Differential cross-section measurements of the production of a top-antitop quark pair in association with a Z boson with the ATLAS detector

Harriet A. J. Watson

Submitted in fulfilment of the requirements of the
Degree of Doctor of Philosophy

School of Physics & Astronomy
College of Science & Engineering
University of Glasgow

April 2024

Abstract

This thesis describes differential cross-section measurements of the production of a top-antitop quark pair in association with a Z-boson ($t\bar{t}Z$) in proton-proton collision data collected by the ATLAS experiment at the Large Hadron Collider (LHC) between 2015 and 2018 with a centre-of-mass-energy of $\sqrt{s} = 13\,\text{TeV}$, corresponding to an integrated luminosity of $140\,\text{fb}^{-1}$. The analysis targets three- and four-lepton final states and aims to measure the differential cross-sections as precisely as possible. A profile likelihood unfolding method is used to extract differential cross-section measurements in a simultaneous fit in multiple orthogonal analysis regions. The differential cross-section measurements are presented as a function of a number of variables which probe the kinematics of the $t\bar{t}Z$ system. Both absolute and normalised differential cross-section measurements are performed at particle- and parton- level and are compared with theoretical predictions. Good agreement is seen between the data and predictions.

Declaration

The research presented in this thesis is the result of my own work within the Experimental Particle Physics Group in the School of Physics & Astronomy at the University of Glasgow and has not been submitted for another qualification at this or any other institution. My research was performed as a member of the ATLAS Collaboration at the LHC, where I benefited from expertise and tools that are the culmination of many years of work by thousands of collaborators. During my research I directly contributed to the collaboration through ATLAS control room shifts. I also served as muon combined performance liaison to the ATLAS Top working group from October 2022 to April 2024.

The contents of Chapters 1 to 5 provide theoretical context, a description of the detector, experimental techniques and analysis tools. As is common for an ATLAS publication, the $t\bar{t}Z$ analysis is a collaborative effort involving around twenty people. I was the lead analyser of the differential cross-section measurements in the tetralepton channel and the combination of the trilepton and tetralepton channels which are described in Chapters 6 to 10. These measurements were published in the Journal of High Energy Physics in July 2023 [1]. The work shown in these chapters are my own except:

- Preparation of simulated event samples and data (Sections 6.1 and 6.2.1).
- Estimation of the non-prompt lepton background (Section 6.2.2).
- Development of neural networks used to define the analysis regions (Sections 6.3.1 and 6.3.2).
- Optimisation of the binning of differential observables (Section 7.2).

In addition, and not discussed in this thesis, I developed a monitoring tool for the muon trigger for my ATLAS author qualification task. This was used to monitor the efficiency of the muon trigger during the transition between Run 2 and Run 3 [2].

Harriet A. J. Watson

Contents

Chapter 1

Introduction

I first visited CERN in 2019 as a bright-eyed and optimistic 21-year-old summer student. My first impression was one that has been reaffirmed in every subsequent visit: CERN is a very cool place to work. It is difficult to think of anywhere else in the world that you can see a truly global effort towards exceptional collaborative science as is achieved there, and on such a large scale. Despite writing this thesis in 2024 as a worn-out almost-Doctor, I hope that some of that enthusiasm remains apparent.

The Large Hadron Collider at CERN was once hailed the world's first "top-quark factory". It has since delivered tens of millions of top-quarks, the heaviest fundamental particle that we know of. The precision of top-quark mass and top-quark pair production cross-section measurements have improved to the point that systematic uncertainties are now dominant. However, there are rare top-quark processes - where additional particles are produced in association with the top-quark pair - that are not well-constrained experimentally. Measuring these processes as precisely as possible provides an excellent probe of the Standard Model of particle physics. My research with the ATLAS experiment has focused on measuring the cross-section of such a rare top-quark process, the production of a top-antitop quark pair in association with a Z-boson ($t\bar{t}Z$).

This thesis presents my own research as well as the background information required to understand it. Firstly, Chapter 2 gives an introduction to the theoretical framework of particle physics, focusing on the properties of top-quarks, cross-section measurements and the production of $t\bar{t}Z$. This is followed by an overview of the ATLAS detector given in Chapter 3. Chapter 4 outlines how we can simulate particle collisions to connect the theory to experiment. Following this, Chapter 5 describes how signals recorded by the ATLAS detector are used to reconstruct and calibrate physics objects. Next, Chapter 6 describes the selection of $t\bar{t}Z$ events that defines the analysis regions. The statistical framework of the analysis, which is the basis of the cross-section fit, is given in Chapter 7, as well as a description of the differential observables. Chapter 8 presents tests of the fitting method for potential bias and Chapter 9 describes the sources of systematic uncertainty that are relevant to the analysis. The measured cross-sections of $t\bar{t}Z$ are presented in Chapter 10 and compared to previous ATLAS measurements. Finally, Chapter 11 gives a summary of the work completed for this thesis, with an outlook towards future measurements.

Chapter 2

Theoretical background

This chapter provides the theoretical context for the research presented in this thesis. This begins with an introduction to the Standard Model of particle physics, focusing on the top-quark and the Z-boson. This is followed by a description of cross-section measurements at colliders and specific features of the production of $t\bar{t}Z$. Finally, some motivation is given for what these measurements can tell us about physics beyond the Standard Model.

2.1 The Standard Model

In particle physics, the Standard Model (SM) is the mathematical framework that describes the fundamental particles in our Universe and their interactions. It is our best description of matter on the smallest possible scale, so far. The fundamental forces included in the SM are the strong nuclear force, the weak nuclear force[1] and the electromagnetic force. The weak and electromagnetic forces are unified above a certain energy scale to form the electroweak (EWK) force. At its heart, the SM is a quantum field theory (QFT), which means that forces are described by fields and particles are quanta of these fields, in a way that is consistent with both quantum mechanics and special relativity. Particles are either mediators of the fundamental forces or matter particles. The SM Lagrangian, $\mathcal{L}_{\text{SM}}$, follows local $SU(3)^C \times SU(2)^L \times U(1)^Y$ gauge symmetry. The underlying Lie algebra of each term dictates the number of mediator

[1] Referred to simply as the strong and weak forces, respectively, from here onward.

particles, or gauge bosons, that exist for the corresponding field. The $SU(3)^C$ term represents the strong force, generating eight spin-1 gauge bosons that conserve colour charge (C) [3]. The $SU(2)^L \times U(1)^Y$ gauge group has four-dimensional Lie algebra, corresponding to the four spin-1 gauge bosons of the unifed EWK force that conserve the weak isospin (L) and hypercharge (Y) [4].

Particles in the SM fall into two categories: spin-$\frac{1}{2}$ fermions, and integer-spin bosons. The fermions - or matter particles - can be further divided into leptons and quarks. Six leptons and six quarks are paired respectively into three generations of increasing mass. Three leptons, the electron, muon and tau, have negative electromagnetic charge (Q) and interact via the electroweak force. For each flavour of lepton there is a corresponding neutrino with neutral electromagnetic charge and very low mass. Quarks possess both electromagnetic charge and colour charge and thus can interact via both the electroweak and strong forces. In order of increasing mass, the six quarks are named: up (u) and down (d) in the first generation, strange (s) and charm (c) in the second generation, and bottom (b) and top (t) in the third generation. For each fermion, there is a corresponding antiparticle with equal mass and flipped quantum numbers. Leptons and quarks interact by exchanging a mediator of the fundamental forces - a boson. The strong and electroweak forces, which have relatively short range, are the most relevant to the small-scale interactions of elementary particles. Currently, there is no self-consistent quantum description of the fourth fundamental force, the gravitational force, and it is not currently included in the SM.[2] Despite having infinite range, the effects of the gravitational force are small enough to be neglected in collider physics experiments. The electromagnetic force also has infinite range, but its field strength is higher than that of gravity. The relative field strengths of the fundamental forces are shown in Table 2.1.

The gluon (g) is the mediator of the strong force and, therefore, possesses colour charge. Quantum chromodynamics (QCD) is the description of the interactions of coloured objects via the strong force [5]. Due to colour charge confinement, free quarks, which are not colour-singlet states, cannot be observed. Instead, quarks form colourless hadrons made up of two or more quarks or antiquarks.

[2] Our best description of gravity is provided by general relativity.

Force	Relative field strength	Range
Strong nuclear	1	10^{-15} m
Weak nuclear	10^{-6}	10^{-18} m
Electromagnetism	$\frac{1}{137}$	∞
Gravitational	$\sim 10^{-40}$	∞

Table 2.1: Range and relative field strength of the fundamental forces.

The photon (γ) is the mediator of the electromagnetic force, and the $W^{\pm}$ and Z^0 bosons are the mediators of the weak force, where superscripts denote the electromagnetic charge.[3] The gluon, photon and Z-boson, being invariant under charge conjugation, are their own antiparticles while the W^+- and W^--bosons are mutual antiparticles. A scalar (spin-0) boson, is required for the process of spontaneous electroweak symmetry breaking (EWSB), giving rise to the Z- and W-boson masses. The Higgs mechanism was proposed by Brout, Englert and Higgs [6, 7] and the Higgs boson was discovered by the ATLAS and CMS experiments in 2012 [8, 9]. The associated Higgs field interacts with fermions via the Yukawa couplings, which are proportional to fermion mass. Table 2.2 shows a summary of the particles and forces that make up the Standard Model.

2.1.1 The top-quark

The top-quark was first predicted in 1973 by Kobayashi and Maskawa [10], as part of a third generation of quarks. It was discovered decades later, in 1995, by the CDF and DØ experiments [11, 12]. The time between prediction and discovery is due to the large mass of the top-quark, or rather, the discrepancy between the top-quark mass and the energies probed by particle experiments before the 1990s. The top-quark is the most massive fundamental particle, with $m_{\mathrm{t}} = (172.52 \pm 0.33)\,\mathrm{GeV}$ [13] and thus a strong coupling to the Higgs boson. At hadron colliders such as the LHC, the top-quark is most often produced as part of a top-antitop quark ($t\bar{t}$) pair via the strong interaction. The production of $t\bar{t}$ is initiated by gluon-gluon fusion around 90% of the time, as shown in Figures 2.1a to 2.1c. The remaining 10% is initiated via quark-antiquark annihilation, as in Figure 2.1d.

[3] Superscript electromagnetic charge notation is neglected when unnecessary.

	Quarks			Leptons	
Generation		Mass	Q	Mass	Q
I	$\begin{pmatrix} u \\ d \end{pmatrix}$	2.16 MeV 4.67 MeV	$+\frac{2}{3}$ $-\frac{1}{3}$	$\begin{pmatrix} e^- \\ \nu_e \end{pmatrix}$	0.511 MeV < 0.8 eV	-1 0
II	$\begin{pmatrix} c \\ s \end{pmatrix}$	1.27 GeV 93 MeV	$+\frac{2}{3}$ $-\frac{1}{3}$	$\begin{pmatrix} \mu^- \\ \nu_\mu \end{pmatrix}$	105.66 MeV < 0.19 MeV	-1 0
III	$\begin{pmatrix} t \\ b \end{pmatrix}$	172.52 GeV 4.18 GeV	$+\frac{2}{3}$ $-\frac{1}{3}$	$\begin{pmatrix} \tau^- \\ \nu_\tau \end{pmatrix}$	1.78 GeV < 18.2 MeV	-1 0

Force	Mediator(s)	Mass [GeV]	Q
Strong	g	0	0
Weak	Z^0, $W^\pm$	91.2, 80.4	0, ± 1
Electromagnetism	γ	0	0
Higgs field	H	125.2	0

Table 2.2: Particles and forces of the Standard Model, where Q is the electromagnetic charge and mass values are given by the Particle Data Group [14], except the mass of the top-quark which is measured in Ref. [13]. and the mass of the Higgs boson, which is measured in Ref. [15].

The high mass of the top-quark dictates some of its other properties: the top-quark lifetime is $\tau_\mathrm{t} \sim 10^{-25}$ s and it decays before it can hadronise [14]. Therefore, the top-quark does not form bound states, unlike the lighter quarks. According to the Cabbibo-Kobayashi-Maskawa (CKM) matrix [10, 16], which parameterises quark flavour-mixing, top-quarks decay to a down-type quark (d, s or b) and a W-boson with a probability of over 97% [14]. The final state particles of $t\bar{t}$ events are determined by the decay mode of the W-bosons, which can be hadronic ($W \to q\bar{q}'$) or leptonic ($W \to \ell\nu_{\ell'}$). Figure 2.2 shows the branching ratios for the decay of the W-boson. Considering only top-quarks decaying to Wb, $t\bar{t}$ events are categorised into channels, each

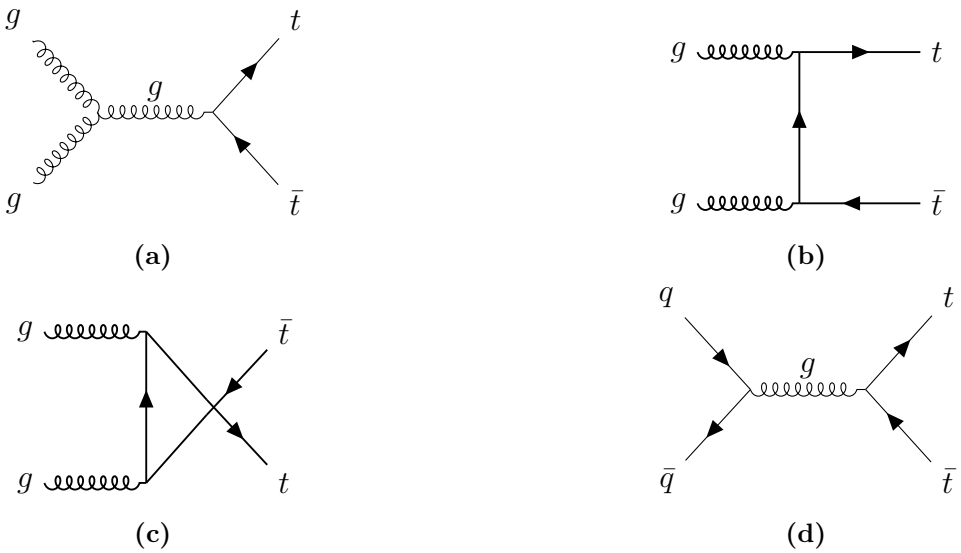

Figure 2.1: Leading-order Feynman diagrams of top-antitop quark pair production from hadron-hadron collisions.

with different final-state particles: all-hadronic (four light-flavour quarks), semi-leptonic (two light-flavour quarks, a charged lepton and a neutrino), or di-leptonic (two charged leptons), each with two b-quarks. Tau leptons are unstable and have a short lifetime ($\sim 10^{-13}$ s), which means that they are difficult to reconstruct in particle detectors. For this reason, decay modes involving tau leptons are not typically used to measure $t\bar{t}$ events. Figure 2.3 shows the approximate branching ratios of the dominant $t\bar{t}$ decay modes.

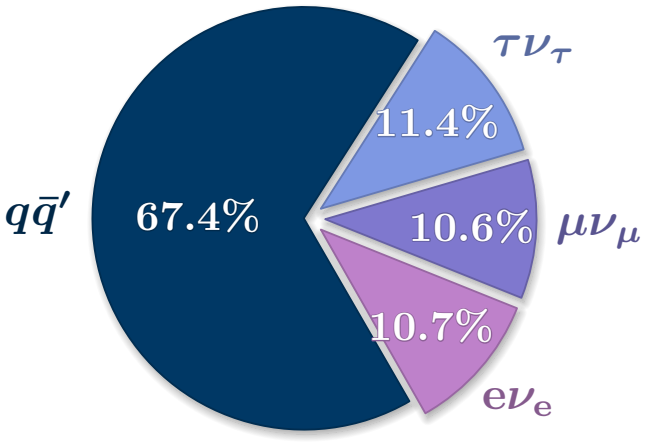

Figure 2.2: Branching ratios for the dominant decay modes of the W^+-boson [14]. W^- decay modes are charge conjugates of the modes shown. The total adds to 100.1% due to rounding.

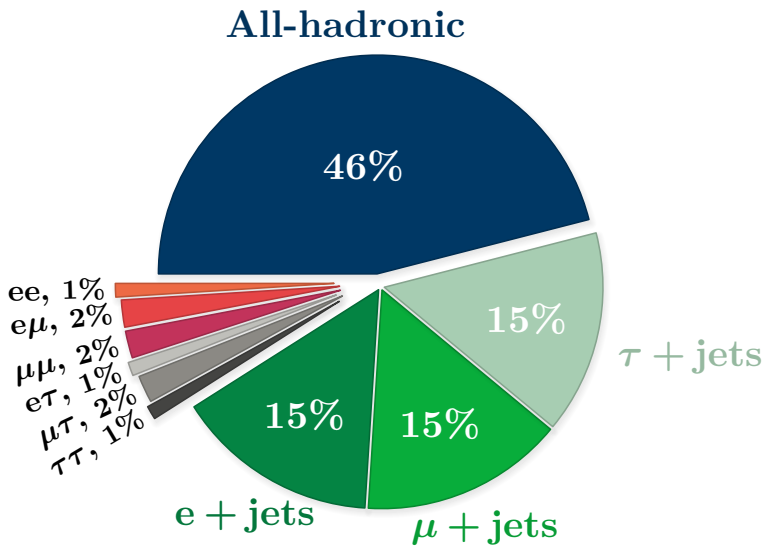

Figure 2.3: Approximate branching ratios for the dominant decay modes of the $t\bar{t}$ system assuming that top-quarks decay like $t \to Wb$ 100% of the time. Bare quarks hadronise and are detected as *jets*: this is discussed further in Chapter 5.

2.1.2 The Z-boson

The Z-boson was discovered by the UA1 and UA2 experiments in 1983 at CERN [17, 18]. With a mass of (91.1876 ± 0.0021) GeV [14], the Z-boson can decay to pairs of opposite-sign-same-flavour (OSSF) charged leptons, a neutrino-antineutrino pair, or a quark-antiquark pair. The branching ratios of the Z-boson decay modes are shown in Figure 2.4.

2.2 Cross-section calculations and $t\bar{t}Z$

Precision measurements of $t\bar{t}$ production in association with other massive particles, such as a Z-boson, are required to complete our understanding of the top-quark. The production of $t\bar{t}Z$ is 1000× rarer than $t\bar{t}$ production and offers a unique window into the top-quark-Z-boson coupling. Currently, the strength of this coupling is not well constrained experimentally, which motivates the aim to precisely measure the $t\bar{t}Z$ production cross-section. This section discusses the theoretical calculation of cross-sections in general and previous measurements of the $t\bar{t}Z$ production cross-section.

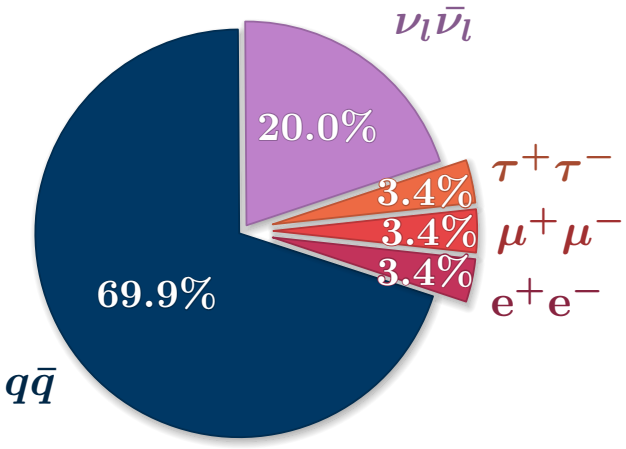

Figure 2.4: Branching ratios of the dominant decay modes of the Z-boson [14]. The total adds to 100.1% due to rounding.

At particle collider experiments, the scattering cross-section, σ, is related to the scattering probability of two colliding particles. The scattering cross-section is proportional to the rate of scattering events:

$$\sigma \propto \frac{\mathrm{d}N}{\mathrm{d}t}, \tag{2.1}$$

where the number of events, N, can be measured experimentally. To calculate cross-sections predicted by theory, we use the fact that the scattering cross-section is proportional to the square of the scattering amplitude. For a given hard scattering process, the amplitude can be calculated according to Feynman rules, summing over all possible Feynman diagrams that have the same initial- and final-state particles. This requires knowledge of the momenta of the initial colliding particles. Protons are not fundamental particles in the SM, instead consisting of three valence quarks (uud), as well as sea (anti)quarks and gluons. In the context of LHC collisions, these are referred to collectively as *partons*. When colliding protons, it is not trivial to know the momentum fraction carried by each of the colliding partons, any of which could initiate a particle process that we want to measure. These must be derived from data, requiring parton distribution functions (PDFs), which describe the probability f_i for a parton of type i to have a Bjorken fraction x of the proton momentum. A problem arises from the fact that there are

strong interactions at two energy scales within the colliding proton: high-energy interactions between partons originating from different colliding protons and low-energy interactions between partons originating from the same proton. At low energies, the strong coupling constant (α_s) is larger than one, and the cross-section calculation can no longer be solved perturbatively. A factorisation energy scale (μ_f) can be defined as the threshold between perturbative and non-perturbative behaviour. Then, a cross-section calculation can be factorised into high-energy and low-energy parts and solved independently. For a process $pp \to X$, the production cross-section can be written as a factorisation of the hard-scatter cross-section and the PDF such that

$$\sigma_{pp\to X} = \sum_{i,j\in g,q,\bar{q}} \int dx_1 dx_2 f_i(x_1, \mu_f^2) f_j(x_2, \mu_f^2) \hat{\sigma}_{ij\to X}, \tag{2.2}$$

where $\hat{\sigma}_{ij\to X}$ is the partonic cross-section. PDFs depend on the factorisation scale according to the DGLAP equations [19, 20, 21] and are fitted to experimental data, with data from multiple experiments contributing to a single PDF set.

In principal, the number of Feynman diagrams that contribute to a particular process is virtually infinite due to additional virtual gluon self-interaction (loops) or low-momentum radiation. Each additional QCD vertex contributes a factor of α_s, which is smaller than one at LHC collision energies. Therefore, higher-order QCD contributions are suppressed. The precision of the theoretical cross-section calculation depends on the order of the summation. The partonic hard-scatter cross-section of a given process can be written as a power series in α_s:

$$\hat{\sigma}_{if} = M_{if}^{(0)} + \alpha_s M_{if}^{(1)} + \alpha_s^2 M_{if}^{(2)} + \dots , \tag{2.3}$$

where the first term is the leading order (LO) contribution to the hard scatter process, the second is the next-to-leading-order (NLO) contribution, and so on. For a cross-section calculation at NLO, the series is truncated after the second term, neglecting additional terms. For calculations at NLO and above, it is necessary to account for ultra-violet (UV) divergences that can arise from QFT integrals when virtual particle loop momenta are large. The calculation must also account for infrared (IR) divergences, that arise from real, low-energy soft and collinear gluon emissions. A renormalisation of the SM Lagrangian is used to prevent UV divergences,

Figure 2.5: Leading-order Feynman diagrams of the production of a top-antitop quark pair in association with a Z-boson via a) gluon-gluon fusion and b) quark-antiquark pair annihilation.

introducing a parameter named the renormalisation scale, μ_r. Leading-order Feynman diagrams of the production of $t\bar{t}Z$ at hadron colliders are shown in Figure 2.5.

The final-state particles of $t\bar{t}Z$ depend on the decay channels of both the $t\bar{t}$ system and the Z-boson. While $t\bar{t}Z$ final states with no leptons have the highest branching ratio, the background is also high which significantly reduces the potential measurement sensitivity. For the research presented in this thesis, we focus on leptonic ($\ell = \mu, e$) final states. The differential cross-section measurements of $t\bar{t}Z$ are performed in the trilepton (3ℓ) and tetralepton (4ℓ) channels, where the Z-boson always decays to two OSSF leptons and the $t\bar{t}$ system decays semi-leptonically or dileptonically. Figure 2.6 shows the approximate branching ratios of $t\bar{t}Z$ final states in terms of the number of leptons.

Figure 2.7 shows a summary of the inclusive cross-section measurements of top-quark processes by the ATLAS experiment compared to theoretical predictions. Several other top-quark processes such as $t\bar{t}H$, tZq and $t\bar{t}W$ have similar multi-lepton final states to $t\bar{t}Z$, as well as small production cross-sections. In order to measure these processes precisely, knowledge of the $t\bar{t}Z$ cross-section from data is required. Currently, the most precise theoretical calculation of the inclusive $t\bar{t}Z$ cross-section at NLO has a precision of 10% [22]. Theoretical predictions of $t\bar{t}Z$ differential cross-sections at NLO plus next-to-next-to-leading-logarithm (NNLL) accuracy, including EWK corrections, are also calculated in Ref. [22] and include those as functions of the rapidity and the transverse momenta of the top-quarks and the Z-boson, and the invariant masses of the $t\bar{t}$ and $t\bar{t}Z$ systems.

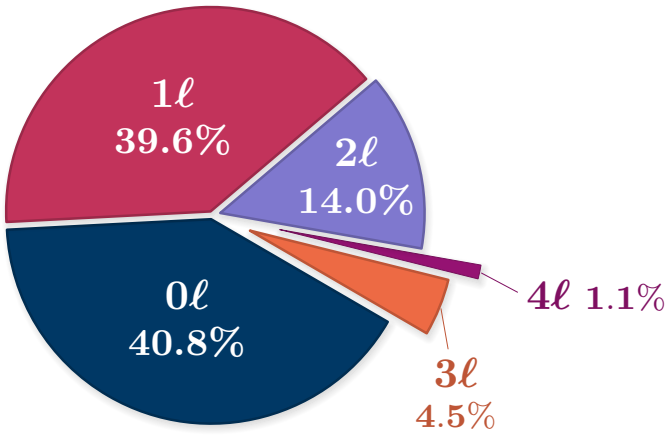

Figure 2.6: Approximate branching ratios of the leptonic ($\ell = e, \mu, \tau$) final states of $t\bar{t}Z$. When excluding final states with τ leptons, the 3ℓ and 4ℓ channels have branching ratios of 1.9% and 0.3% respectively.

Measurements of the $t\bar{t}Z$ production inclusive and differential cross-sections at the LHC have been performed by both the ATLAS and CMS collaborations. The first differential cross-section measurement in $t\bar{t}Z$ production at the LHC was performed by the CMS Collaboration, using its 2016–2017 dataset from $\sqrt{s} = 13\,\text{TeV}$ pp collisions, which corresponds to $77.5\,\text{fb}^{-1}$ [24]. The differential cross-sections were measured as a function of two variables in final states with three or four leptons. In the same analysis, the inclusive $t\bar{t}Z$ cross-section was measured with a precision of 8.2%. The ATLAS Collaboration reported the first measurements of $t\bar{t}Z$ differential cross-sections using its full dataset from Run 2 of the LHC [25]. The inclusive cross-section was extracted in final states with three or four leptons with a precision of 9.5%. The research presented in this thesis reanalyses the ATLAS Run 2 dataset with improved analysis techniques and the aim of increasing the precision of the differential cross-section measurements. Previous results from the ATLAS and CMS collaborations are compatible with the SM predictions [22], and with each other. Figure 2.8 shows measurements of the $t\bar{t}Z$ inclusive cross-section by the ATLAS and CMS collaborations compared to theoretical expected values.

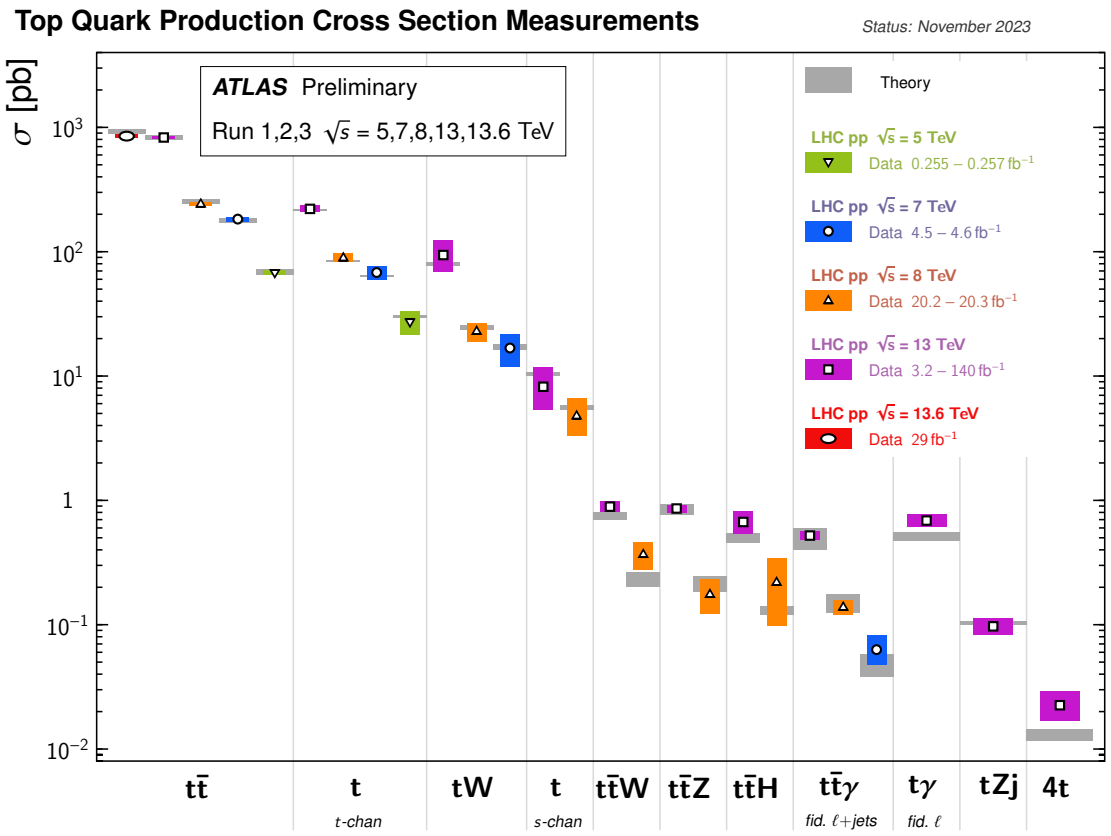

Figure 2.7: Summary of ATLAS top-quark production cross-section measurements, compared to the corresponding theoretical expectations [23]. All theoretical expectations were calculated at NLO or higher.

2.3 Beyond the Standard Model

The SM has been shown to describe observed particle data very well. Despite this, there are many observed phenomena that the SM fails to explain: the matter-antimatter asymmetry of the Universe, neutrino masses and dark matter, to name a few. Since the Higgs boson discovery, the focus of experimental particle physics has been on precision measurements of SM parameters, as well as direct searches for beyond-the-SM (BSM) particles. The search for new physics has so far concluded that unknown processes either occur "hidden" in SM processes, or they occur at higher energy scales via heavy particles. In the case of new physics at some high energy scale, Λ, the Higgs boson effective mass contains corrections from Higgs couplings to massive particles, which are proportional to the Yukawa couplings and the momentum cutoff

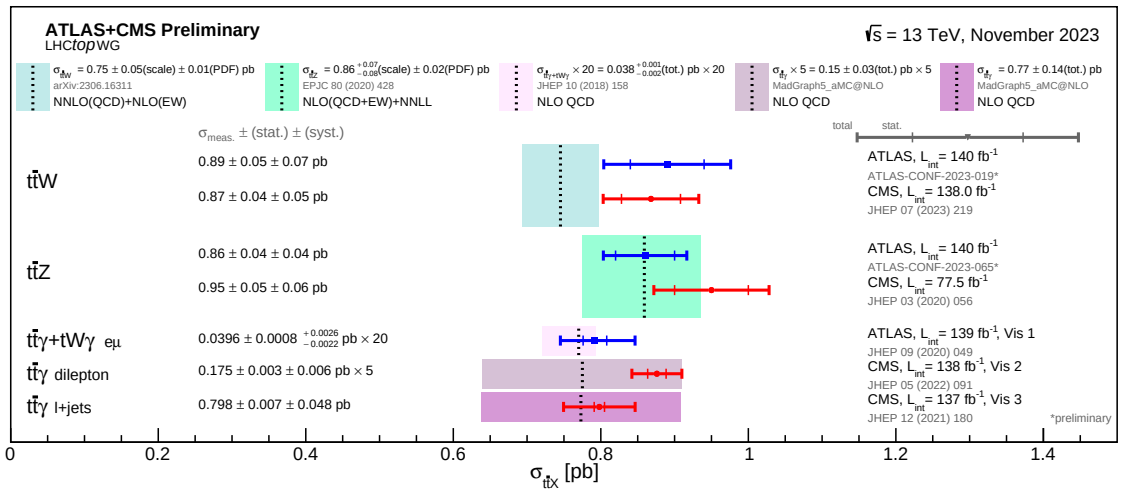

Figure 2.8: Summary of ATLAS and CMS measurements of $t\bar{t}X$ ($X = W$, Z or γ) cross-sections at $\sqrt{s} = 13\,\text{TeV}$ [23]. The $t\bar{t}Z$ measurements are compared to NLO QCD and EWK theoretical calculation complemented with NNLL resummation. The theory bands represent uncertainties due to renormalisation and factorisation scales and PDFs.

on quantum loop corrections. In this case, the relationship between the Higgs mass and the energy scale of new physics is quadratic. The scale of new physics, as motivated by theories for quantum gravity, could be at the Planck scale (10^{19} GeV). However, the Higgs mass is significantly smaller than this, on the EWK scale (10^{2} GeV), posing a question known as the hierarchy problem: why is the Higgs boson so light? Such fine-tuning of a SM parameter indicates that our more generalised understanding is incomplete. As the top-quark Yukawa coupling is very close to one, it has the largest contribution to the Higgs effective mass, making it a compelling avenue of investigation. Studies of the Higgs boson-top-quark coupling could reveal BSM contributions to its amplitude.

It is possible that new physics contributions will occur at energies beyond the TeV scale, making direct detection of new particles inaccessible to current experiments. However, processes that are dominant at a higher energy scale could have indirect effects at current colliders and experiments planned for the near future. These may be measurable as deviations from SM predictions. In $t\bar{t}Z$, this could manifest as an increased cross-section when the top-quarks and Z-boson have high momentum [26]. Therefore, it is interesting to understand the cross-section of $t\bar{t}Z$ with respect to kinematic observables, such as the momentum of the Z-boson, to high precision. Specific BSM theories that could have the same final state as $t\bar{t}Z$ events include

vector-like quarks [27] and little Higgs models [28]. In addition, supersymmetric extensions of the SM could be contribute to $t\bar{t}Z$ final states [29, 30].

Chapter 3

The ATLAS experiment

Particle physics is considered a relatively young field of research, though it has been one of rapid discovery and expansion. Early experiments, such as the cloud chambers that discovered the positron [31], muon [32] and kaon [33], could be performed in the physics department of a university. Modern experiments push the energy and intensity frontiers, requiring dedicated research facilities with high-energy particle accelerators and colliders.

3.1 The Large Hadron Collider

The Large Hadron Collider (LHC) is a circular particle collider located at the Conseil Européen pour la Recherche Nucléaire (CERN) near Geneva, Switzerland. The LHC is the highest-energy particle collider ever built and it has been the centre of significant particle physics results in recent years, most famously for the discovery of the Higgs boson in 2012 [8, 9]. As I write this, the CERN laboratory celebrates its 70^{th} anniversary. Founded in 1954, CERN has produced a series of particle accelerators before the LHC, which first saw collisions in 2009. The LHC was built in the pre-existing tunnel of the Large Electron-Positron collider (LEP) [34], which is 27 km long and around 100 m underground. Before particles reach the LHC, they are accelerated through a network of lower-energy accelerators. The LHC has been operated in three *runs* of collisions, with long shutdowns in between that are used to upgrade parts of the LHC subsystems

and experiments. Accordingly, *pp* collision data has been collected in three batches so far: Run 1 (2009 - 2013), Run 2 (2015 - 2018) and Run 3 (2022 - present). Upgrades have allowed for increased collision energies since the construction of the LHC. The following paragraphs describe the LHC accelerator complex in Run 2, during which the data analysed for this thesis was collected.

In the first step towards high-energy proton beams, hydrogen gas is ionised, producing H^- ions that are accelerated by a linear accelerator LINAC 2.[1] The H^- ions are then stripped of their electrons using an electric field, leaving only protons. Next, the protons are accelerated through the proton synchrotron booster, the proton synchrotron and the super proton synchrotron. The accelerated protons are then injected into the LHC ring at two sites, such that beams circulate in opposite directions, each with an energy of 6.5 TeV. A series of dipole magnets bend the proton beams around the LHC ring. Proton injections are timed to create a bunch structure in the beam, which is maintained by focusing quadrupole magnets. Each bunch consists of around 1.1×10^{11} protons with 25 ns spacing between the bunches [35]. Focusing electromagnets cause the beams to collide at four collision points on the ring. A diagram of the CERN accelerator network can be seen in Figure 3.1.

The LHC ring collision points correspond to the locations of four large experiments: ATLAS, CMS, ALICE and LHCb [37, 38, 39, 40] which are evenly-spaced around the ring. Each of these experiments were designed with specific aims within particle physics research. ATLAS and CMS are general-purpose detectors that aim to test the properties of the SM and search for new physics signals. The LHCb detector is designed to study CP violation and the production and decay of *b*-hadrons. The ALICE detector is a general-purpose heavy-ion collision detector that aims to study the quark-gluon plasma and strongly-interacting matter. The LHC delivers proton or heavy-ion [2] collisions to each of these experiments.

[1] LINAC 2 was replaced by LINAC 4 in 2019.
[2] Pb, Xe and Au

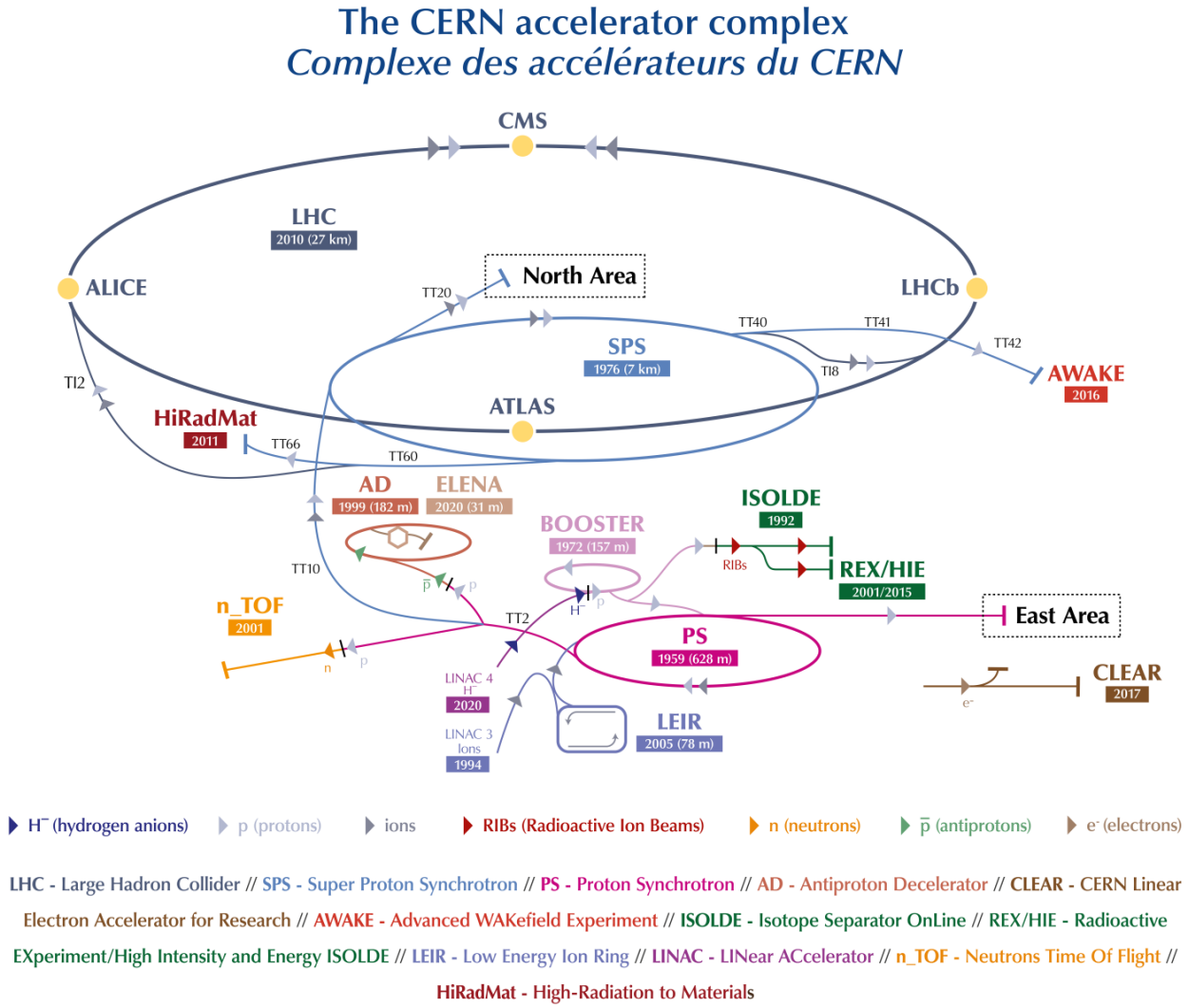

Figure 3.1: Schematic diagram of the CERN accelerator complex [36].

3.2 Collisions and luminosity

Two important parameters for particle colliders such as the LHC are the luminosity of collisions and the centre-of-mass energy of the colliding particle beams. The choice of these parameters is limited by what is technically possible. Naïvely, it is desirable to produce as many collisions as possible, using the highest-possible luminosity and beam energies. However, this is only worth doing if we have the detector technology that is able to record the corresponding rate of collisions to a reasonable precision. Additionally, while a certain luminosity of collisions is

delivered by the LHC, the recorded luminosity of collisions in the ATLAS detector is lower, due to inefficiencies in the detector components. The *instantaneous* luminosity is analogous to the rate of collisions, while the *integrated* luminosity indicates the total size of the collected collision dataset. The latter is typically quoted in inverse femtobarns, fb, where one barn is equal to $10^{-24}\,\mathrm{cm}^2$.

Given the cross-section of a particle interaction ($pp \to X$) at a collider experiment, the number of events for that process, N, can be found using

$$\frac{\mathrm{d}N}{\mathrm{d}t} = \sigma \mathcal{L}_{\mathrm{inst}}, \tag{3.1}$$

where $\mathcal{L}_{\mathrm{inst}}$ is the instantaneous luminosity. For collisions produced by a pair of bunched proton beams with Gaussian profile, this can be written as

$$\mathcal{L}_{\mathrm{inst}} = \frac{N_1 N_2 N_b f}{4\pi\sigma_x\sigma_y}, \tag{3.2}$$

where N_1 and N_2 are the number of protons per bunch in each beam, N_b is the total number of bunches per beam, f is the revolution frequency and σ_x and σ_y are the vertical and horizontal dimensions of the beams [41]. The size of the total dataset of particle collisions is represented by the integration of the instantaneous luminosity over the time period of collisions, giving the integrated luminosity, $\mathcal{L}_{\mathrm{int}}$. The inclusive cross-section, $\sigma_{t\bar{t}Z}$, relates the number of $t\bar{t}Z$ events produced by LHC collisions, $N_{t\bar{t}Z}$, with the integrated luminosity such that

$$N_{t\bar{t}Z} = \mathcal{L}_{\mathrm{int}} \cdot \sigma_{t\bar{t}Z}. \tag{3.3}$$

3.2.1 The Run 2 dataset

The Run 2 dataset refers to data collected at the ATLAS detector from proton-proton collisions provided by the LHC during the 2015 to 2018 period. The data corresponds to an integrated luminosity of $140\,\mathrm{fb}^{-1}$ with a centre-of-mass collision energy of $\sqrt{s} = 13\,\mathrm{TeV}$ [35] and a data-taking efficiency greater than 95% [42].

3.3 The ATLAS detector

Large particle colliders require large detectors; at 44 m long, 25 m in diameter and weighing about the same as the Eiffel Tower (7000 tonnes), A Toroidal LHC Apparatus (ATLAS) is the largest particle detector ever built. The ATLAS detector is a general-purpose detector located at Point 1 on the LHC ring and it consists of a cylindrical barrel, formed of many concentric layers, and two end-caps. Protons collide in the beam pipe at the centre of the ATLAS geometry, which provides almost 4π solid angle coverage around the interaction point (IP). Each layer, or subdetector, of the ATLAS detector is designed to measure the attributes of different types of particle. A system of superconducting magnets is used to aid in charged particle momentum determination. The subdetectors are as follows, starting with the innermost: an inner tracking detector, an electromagnetic calorimeter, a hadronic calorimeter and a muon spectrometer. This section describes the ATLAS detector during Run 2 of the LHC, a schematic of which is shown in Figure 3.2.

3.3.1 Detector geometry

The ATLAS detector geometry follows both a right-handed Cartesian and a cylindrical coordinate system centered at the IP. The anticlockwise beam direction defines the z-axis of the Cartesian coordinate system, with the x-direction defined as pointing from the IP to the centre of the LHC ring and the y-direction defined as pointing directly upwards [37]. The x-y-plane, which is transverse to the beam direction, is used to define quantities such as the transverse momentum, p_T, of physics objects. In cylindrical coordinates, the polar angle, θ, is the angle from the beam axis and the azimuthal angle, ϕ, is the angle from the y-axis around the beam axis. It is useful to define the *rapidity*, y, of a particle as

$$y = \frac{1}{2} \ln \frac{(E + p_z)}{(E - p_z)}, \tag{3.4}$$

where E is the particle energy and p_z is the momentum in the z-direction. If the p_z of a particle is small, the term in the natural logarithm will go to one, and the rapidity will go to zero.

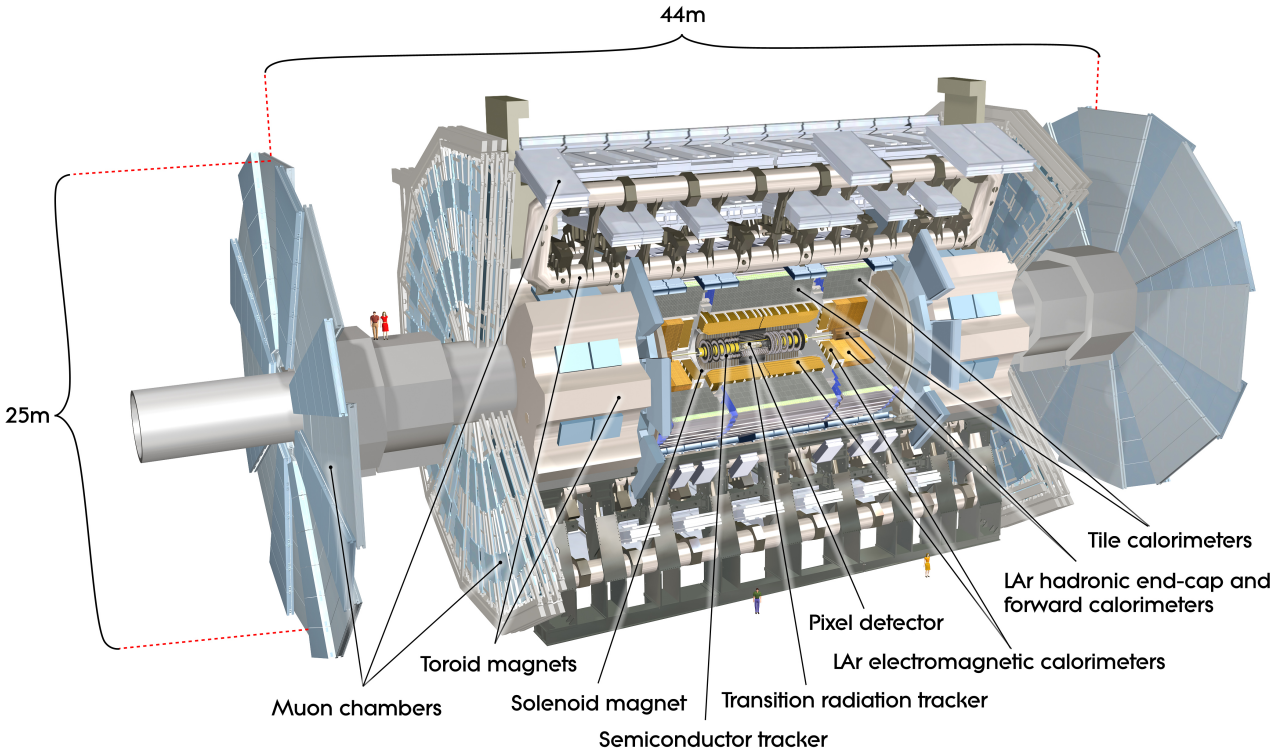

Figure 3.2: Schematic diagram of the ATLAS detector in Run 2 [43].

This corresponds to particles directed perpendicularly to the beam, in the x-y plane. In the opposing limit, where the particle is directed close to the beamline, the rapidity goes to infinity for massless particles. A similar quantity, that is easier to measure for highly energetic particles, is the *pseudorapidity*, η, which is defined as

$$\eta = -\ln \tan \frac{\theta}{2}. \tag{3.5}$$

For massless particles, $\eta = y$. Differences between two rapidities, or pseudorapidities for massless particles, are invariant under Lorentz boosts in the z-direction. Using this, a distance parameter is defined as $\Delta R = \sqrt{(\Delta\eta)^2 + (\Delta\phi)^2}$ and used to describe the relative positions of physics objects, described in Chapter 5, within the detector.

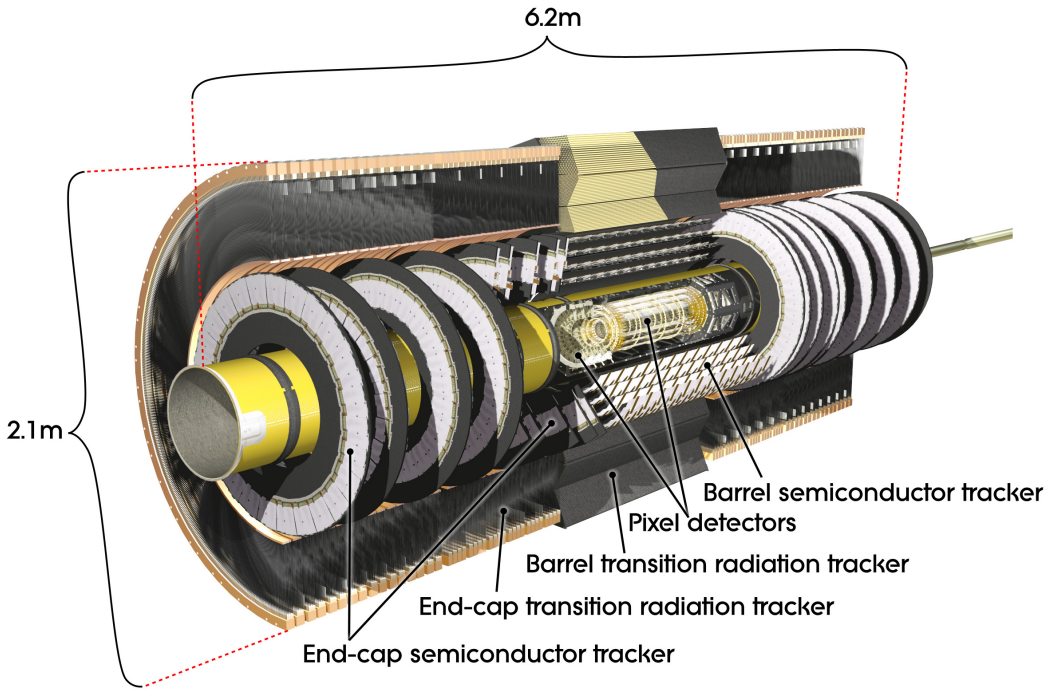

Figure 3.3: Schematic diagram of the inner detector within the central solenoid showing the barrel and end-cap components in Run 2 [47].

3.3.2 Inner detector

The inner detector (ID) [44, 45] is designed to provide precise tracking information for charged particles originating from the IP, while dealing with the high particle density present in LHC collisions. The ID is made up of three layers: the pixel detector, semiconductor tracker (SCT) and the transition radiation tracker (TRT), all within a 2 T central solenoid magnet [46]. The magnetic field enables the identification of the sign of the charge and momentum measurement of charged particles via the curvature of their tracks. Figure 3.3 shows an overview of the ID, excluding the central solenoid and Figure 3.4 shows an expanded view of each layer of the inner detector.

Silicon pixel detector

The pixel detector provides a set of high-granularity, high-precision measurements close to the IP. The insertable B-layer (IBL) is the part of the pixel detector that is closest to the beam

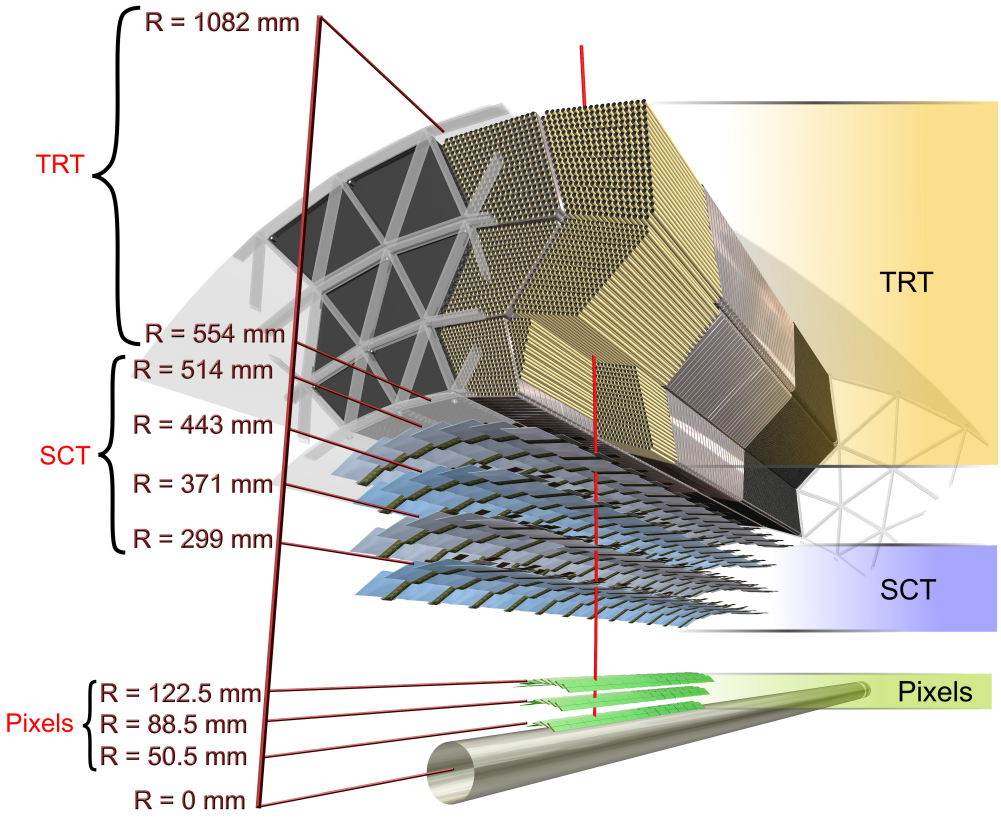

Figure 3.4: Detailed schematic diagram of the different layers of the ATLAS inner detector in Run 2 [48].

pipe and is designed to improve the track reconstruction and identification of b-hadrons [49, 50]. The silicon pixel detector is comprised of silicon substrate connected to electronic readout chips. Charged particles induce excited electron-hole pairs from the doped silicon substrate and resulting free electrons are collected by an anode, causing an electronic signal, or *hit*. The pixel detector has three cylindrical barrel layers and two three-layer disks in the end-caps, covering an acceptance of $|\eta| < 2.5$.

Semiconductor tracker

The SCT encloses the pixel detector and consists of modules of silicon sensors arranged into long strips [51]. Pairs of strip modules are offset by an angle which enables an estimate of the coordinate along the length of the strips to be measured. The detection principle is the same for the silicon strips as in the pixel detector. The strip arrangement allows for easier manufacturing, at the cost of lower granularity, than the pixel detector. There are four layers in the barrel and nine disks in each of the end-caps. The SCT has an acceptance of $|\eta| < 2.5$.

Transition radiation tracker

The TRT is the final and largest part of the ID. The basic detector elements of the TRT are 4 mm polyimide drift tubes, also known as straws [52]. Each straw is filled with a gas mixture and contains an anode wire through its centre. During Run 1, the gas mixture was Xe (70%), CO_2 (27%) and O_2 (3%), but significant leaks occurred that forced a switch to a primarily argon gas mixture in unrepaired regions due to the high cost of xenon. Charged particles ionise the gas, releasing electrons that drift towards the wire, resulting in an electronic signal that is read out from each end of the straw. In the barrel, the straws are aligned with the beam pipe and in each of the end-caps they are arranged perpendicularly to the beam pipe in two disks.

A special feature of the TRT is that the gas mixture absorbs transition radiation from charged particles. This effect is largest for electrons, due to their low mass, which means that the amount of transition radiation (X-rays) observed can be used to differentiate between electron and pion tracks [53]. The TRT provides a large number of hits that contribute significantly to momentum measurements, which compensates for its precision per point, which is lower than that of the silicon detectors.

3.3.3 Calorimeters

The ATLAS calorimeter system [54, 55] is required to measure the energy of charged and neutral particles[3] travelling through the detector. This is achieved using alternating layers of

[3]Except muons and neutrinos, which are expected to travel through without depositing all of their energy.

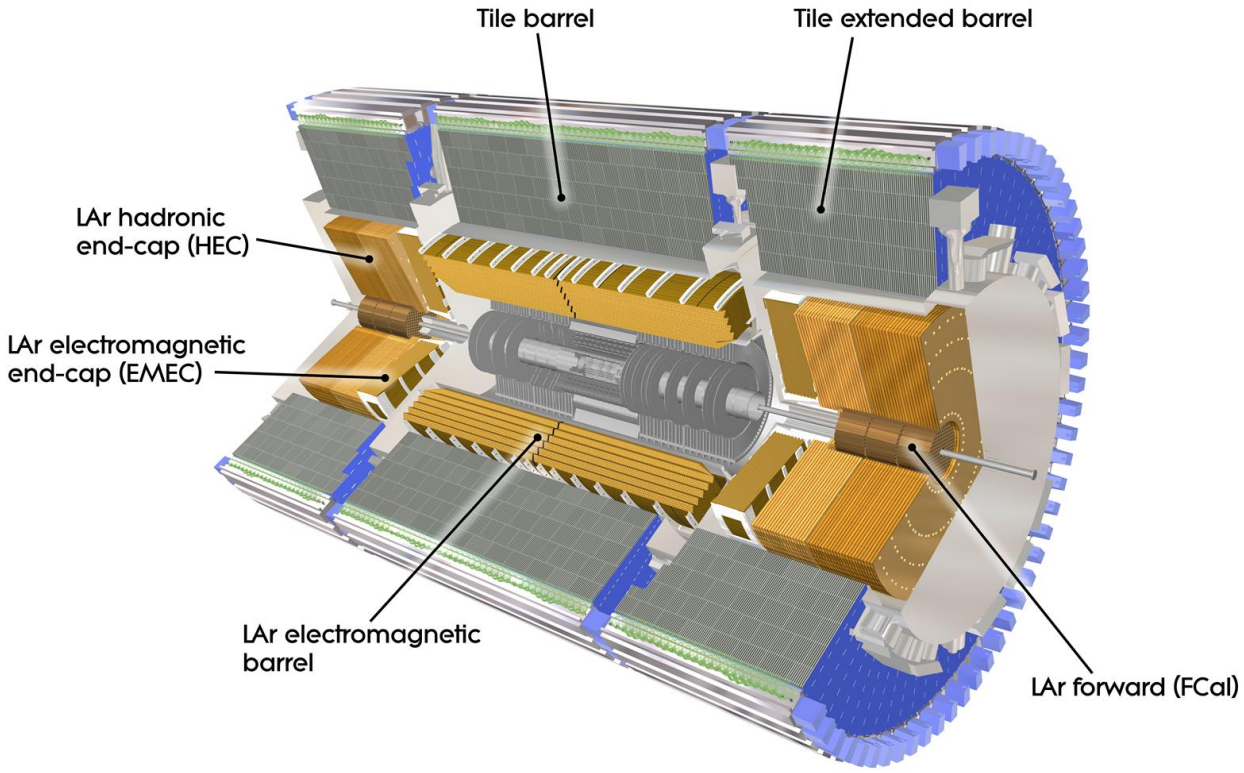

Figure 3.5: Schematic diagram of the ATLAS calorimeter system in Run 2 [56].

high-density material and active layers that measure deposited energy. High-energy particles interact with the high density material, producing cascades of secondary, lower-energy particles, or *showers*. The showering process is different for electromagnetically-interacting particles (e, γ) and hadronic particles (e.g. π, κ, p) that interact largely via the strong force. The radiation length determines the frequency of electromagnetic interactions for a given material. The hadronic equivalent is the nuclear interaction length. Therefore, two distinct calorimeters are used: the electromagnetic calorimeter with fine granularity and the hadronic calorimeter with coarser granularity. The calorimeters are designed to have sufficient depth to capture the full shower of particles produced upon interaction with the calorimeter material. The ATLAS calorimeters are shown in Figure 3.5.

Electromagnetic calorimeter

The electromagnetic calorimeter is a lead and liquid argon (LAr) detector and consists of a barrel section, covering $|\eta| < 1.475$, and two end-cap parts, covering $1.375 < |\eta| < 3.2$, each contained in a cryostat. The electromagnetic end-cap (EMEC) components are two coaxial wheels with the inner wheel covering $2.5 < |\eta| < 3.2$ and the outer wheel covering $1.375 < |\eta| < 2.5$. Incident particles interact with layers of lead material, producing showers of secondary charged particles. The shower particles travel into the LAr layer, ionising LAr atoms and producing an electron current that is read out via electrodes. The electrodes are accordion-shaped in order to achieve full azimuthal coverage [54]. The LAr forward calorimeter (FCal) covers the regions closest to the beam and uses layers of copper and tungsten to measure both electromagnetic and hadronic particle showers. The thickness of the electromagnetic calorimeter is over 22 radiation lengths in the barrel and more than 24 in the end-caps [37].

Hadronic calorimeter

The hadronic calorimeter consists of a tile calorimeter enveloping the electromagnetic barrel calorimeter, the LAr end-cap calorimeter (HEC) and the LAr FCal. The same lead-LAr design as the electromagnetic calorimeter is used for $1.4 < |\eta| < 4.8$ in the hadronic calorimeter [54]. Outside of this volume is the tile calorimeter which is comprised of steel absorbing layers and scintillating tiles [55]. The HEC uses LAr as the active material with copper absorbing layers. The thickness of the hadronic calorimeter is around 10 interaction lengths in both the barrel and the end-caps [37].

3.3.4 Muon spectrometer

The outermost subsystem of the ATLAS detector, the muon spectrometer, contains high-precision tracking chambers within a magnetic field [57]. Muons and neutrinos are the only SM particles expected to travel through the calorimeters without depositing all of their energy. The barrel toroid is used to deflect muon trajectories in the $|\eta| < 1.4$ range while two smaller end-cap toroids bend muon tracks in the $1.6 < |\eta| < 2.7$ range such that the resulting magnetic

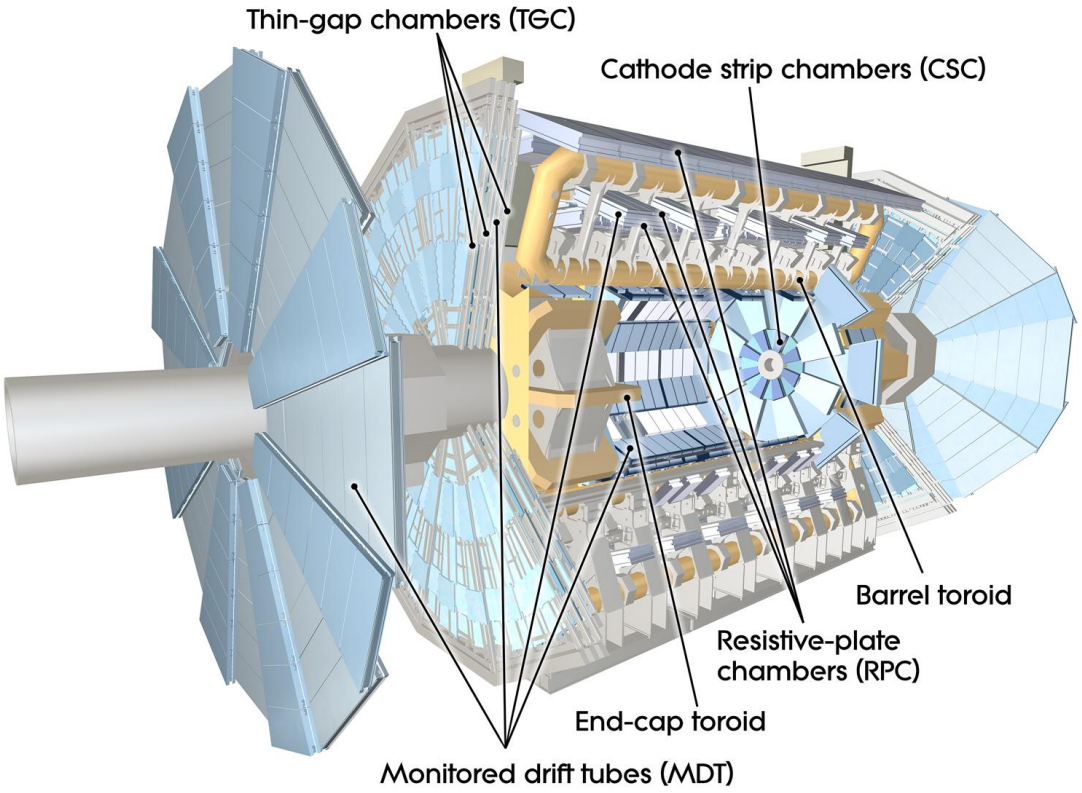

Figure 3.6: Schematic diagram of the ATLAS muon spectrometer in Run 2 [60].

field is mostly orthogonal to muon trajectories [58]. The transition region ($1.4 < |\eta| < 1.6$) is covered by the combination of the barrel and end-cap fields. Each of the toroids are comprised of eight coils and cooled to 4.5 K using liquid helium. Tracks are measured in three layers of chambers: in a cylindrical configuration in the barrel, and in planes perpendicular to the beam in the end-cap and transition region. Precision measurements of track coordinates are provided by monitored drifts tubes (MDTs) over most of the η-range. In the innermost plane ($2 < |\eta| < 2.7$), cathode strip chambers (CSCs) are used, which have higher granularity than the MDT chambers. The muon spectrometer includes a hardware trigger system (see Section 3.4) covering the $|\eta| < 2.4$ range, which is made up of resistive plate chambers (RPCs) in the barrel and thin gap chambers (TGCs) in the end-cap regions. Figure 3.6 shows a schematic of the muon spectrometer system in Run 2. The muon system in Run 3 has been upgraded with two New Small Wheels (NSW) in the high-rapidity region of the detector [59].

Precision tracking chambers

Muon tracking is largely handled by the MDTs [61] which are similar in operation to the TRT section of the ID. MDTs contain a mixture of argon and carbon dioxide gas which is ionised by passing muons, resulting in electronic readout. The maximum drift time is 700 ns and each chamber delivers a resolution of 35 µm. The MDTs are arranged via chambers into three layers that are perpendicular to the beam pipe. The MDTs cover a range of $|\eta| < 2.7$, except in the innermost end-cap layer where CSCs [62] cover the range $2.0 < |\eta| < 2.7$. The CSC has a finer granularity than the MDTs, which is required at the inner end-caps due to high particle density. The CSC operates in a similar way to the MDT, though they are multi-wired, using cathode strips with surrounding anode wires. This feature leads to much shorter drift times for electrons ionised in the gas mixture. Each chamber has a resolution of 40 µm.

Fast trigger chambers

The precision tracking chambers are complemented by a set of fast trigger chambers, consisting of RPCs [63] and TGCs [64]. The fast trigger chambers can deliver tracking information for muons on a timescale of 15 ns to 25 ns, similar to that of the LHC bunch spacing. This fast and coarse tracking information is used in the trigger decision logic described in Section 3.4, including tracking information in the azimuthal plane, which is not recorded by the MDT and CSC. Three layers of RPCs are used in the barrel, covering $|\eta| < 1.05$, and consist of two parallel resistive plates separated by a few millimetres of gas volume (predominantly $C_2H_2F_4$). Each RPC chamber has a resolution of 10 mm. As before, finer granularity is required in the end-caps ($1.05 < |\eta| < 2.$) and this is provided in the muon trigger hardware via three layers of TGCs. The TGCs are multi-wire proportional chambers similar to the CSCs. Each TGC chamber has a resolution of 2 mm to 6 mm and fine granularity to provide a sharp momentum cut-off for triggered muons.

3.4 Trigger and data acquisition

The high rate of LHC collisions, at 40 MHz, presents technical challenges; electronic readout and data storage are the limiting factors when choosing which events to record. The role of the ATLAS trigger and data acquisition (TDAQ) system is to decide which events could contain interesting physics, and to do so at a rate that meets requirements from the maximum detector readout rate, available processing resources and maximum sustainable rate of permanent data storage. The trigger system does this by evaluating detector hits in real-time using pre-determined fast algorithms to record events of interest. A set of trigger algorithms is designed which target events with signals from high-energy physics objects in the final state. A multi-level trigger system is used, comprised of a Level 1 (L1) trigger that reduces the event rate to around 100 kHz, followed by a High-Level trigger (HLT) that further reduces the event rate to around 1 kHz [65].

3.4.1 Level 1 trigger

The L1 trigger, which is hardware-based, uses information from the calorimeters and the RPCs and TGCs in the muon spectrometer to perform a coarse analysis of each event within 2.5 µs. Events involving high-p_T objects are identified through areas of η-ϕ space containing signals in the muon spectrometer and/or the calorimeters. Such areas are called regions of interest (ROI) and these are passed to the HLT for further processing. All detector information is available at HLT and while most HLT algorithms process ROI, some algorithms run on the full event.

3.4.2 High-level trigger

The HLT, which is software-based, uses a chain of slower, but more precise, algorithms to select events of interest for permanent storage. The HLT software is run on server computers. The most CPU-intensive algorithms, which use fine-granularity position data, are called last in the trigger chain so that they are called for the fewest possible events. A *menu* of many trigger chains is used to identify specific physics object(s) such as electrons, muons, photons, jets or

two muons for B-meson candidates. For example, a single muon trigger chain will select events with at least one muon above a predetermined p_T threshold. An event that passes any trigger chain on the menu is stored permanently. To further control the event rate, prescales can be applied that reduce the rate for a particular trigger chain by 1/(prescale value) [66]. In this analysis, events are considered that pass either the single electron or single muon triggers:

- `HLT_e24_lhmedium_L1EM20VH`,
- `HLT_e26_lhtight_nod0_ivarloose`,
- `HLT_e24_lhmedium_L1EM20VH1`,
- `HLT_e26_lhtight_nod0_ivarloose`,
- `HLT_e60_lhmedium_nod0`,
- `HLT_e120_lhloose2`,
- `HLT_e140_lhloose_nod0`,
- `HLT_mu20_iloose_L1MU15`,
- `HLT_mu26_ivarmedium`, or
- `HLT_mu50`.

The chains are named according to their selection requirements: the number after `e` and `mu` refer to the p_T threshold in GeV, and the rest of the chain name refers to likelihood or isolation requirements [67, 68, 69, 70]. The efficiency for the combination of the electron triggers is 75 - 95% [71]. The efficiency of passing either the muon trigger chains is 60 - 70% in the barrel and around 80% in the endcaps [72].

Chapter 4

Event simulation

In order to compare LHC data to theoretical predictions, we require a tool that can turn partonic cross-section calculations into physics objects that we reconstruct using a particle detector, bridging the gap between theory and experiment. Monte Carlo (MC) methods, which involve random sampling, are used by event generators that employ a theoretical framework, such as the SM, to produce particle events in a given kinematic phase space and set of particle collisions. Virtually all ATLAS analyses rely on MC event generators to design analyses, especially when data-driven approaches are not suitable. To fully simulate a pp collision event recorded by the ATLAS detector, the resolution of the detector is taken into account using a detector simulation.

4.1 Event generation

Using PDF sets, which were introduced in Section 2.2, as inputs, the following steps are performed in order to produce simulated particle collider events. Section 4.1.1 describes how matrix element (ME) calculations are performed to determine the four-vectors of final-state partons involved in the hard-scatter event e.g. $pp \to t\bar{t}Z$. Additional emissions from final-state partons are modelled with parton shower (PS) algorithms, described in Section 4.1.2, and the formation of bound states from free quarks (hadronisation), is included using a non-perturbative model described in Section 4.1.3. Beyond the hard scatter, additional interactions and unstable

particles can arise from the remaining valence and sea quarks, described in Section 4.1.4 as the underlying event. Further to this, in each bunch crossing there can be up to 70 interactions [35]. This is known as pileup and is described in Section 4.1.5. Finally, a detector simulation, described in Section 4.1.6 is required to provide the detector response to final-state particles such that the simulated events are then directly comparable to data.

4.1.1 Hard scatter

As discussed in Chapter 2, the hard-scatter process is calculated through its matrix element at a fixed-order of α_s. The factorisation and renormalisation scales, the latter of which is required for calculations beyond LO, used in this calculation are usually chosen as approximately equal, and at an energy around that of the relevant process e.g. the mass of the top-quark. Fixed-order calculations in this analysis are mostly performed to NLO accuracy - a full description of the generated event samples is given in Chapter 6.

4.1.2 Parton shower

Following the fixed-order calculation, additional emissions from ingoing and outgoing partons are simulated. Including the QCD radiation from a large number of partons exactly is theoretically challenging and computationally expensive. Instead, parton shower algorithms are used, which use an approximation based on the fact that radiation from partons is enhanced in the collinear limit and that multiple successive soft and collinear emissions can be factorised in terms of the original partonic emission. MC sampling is used to generate two random numbers that represent the momentum fraction and virtuality[1] of parton cascades. Multiple parton emissions are generated in sequence from the hard scatter energy scale until the cutoff scale is reached at around 1 GeV.

Many MC event generators include a parton shower algorithm, with differences in the ordering of the soft emissions differentiating Pythia [73], Sherpa [74] and Herwig [75]. When combining the matrix element calculation and parton shower, it is important to avoid

[1] Lorentz-invariant quantity related to the squared four-momentum.

double-counting real emissions from each part. Dedicated merging and matching algorithms are used to account for this [76, 77].

4.1.3 Hadronisation

Hadronisation is the process by which bare quarks form colour-singlet states - hadrons. This concerns momentum scales on the order of the confinement scale, where α_s is large, and must be approximated with a non-perturbative method. Two main methods exist that contain parameters that can be tuned with data. The Lund string method [78] is used by PYTHIA while the cluster method [79] is used by HERWIG and SHERPA. In the Lund string model, quarks and antiquarks are connected by a colour string that increases in length and energy as a $q\bar{q}$ pair separate. At some point it is energetically favourable to break the string, forming another $q\bar{q}$ pair. Owing to the asymptotic freedom of QCD, the combined energy of the two resultant hadrons is smaller than the energy of the initial state. The cluster method, in contrast, is based on the concept of preconfinement, which is that after the parton shower, it is possible to form colour-singlet states from partons clustered nearby in phase space due to colour flow. Features common to both methods are:

- hadronisation does not significantly change the direction of partons from the hard-scatter event, and
- the model must choose between the large number of possible colour flows between final state partons.

The decay of b- and c-hadrons are simulated using decay amplitudes, including angular and time-dependent correlations for a decay chain made up of many nodes.

4.1.4 Underlying event

The underlying event usually refers to the low-energy interactions concerning partons not involved in the hard-scatter, parton shower or hadronisation processes. Some effects considered in these first three steps can be intertwined with the underlying event, so this step can take on

different definitions depending on the particular event generation sequence. Dedicated models are tuned to experimental data in order to account for the underlying event in MC simulation. Multiple-parton interactions (MPIs) occur when more than one hard-scatter process occurs between multiple partons. There is no single widely-used method to include MPIs: the simplest models assume that the parton interactions are independent, apart from energy and momentum considerations, while more complex models include potential interaction, such as gluon exchange, between the MPIs.

4.1.5 Pileup

Pileup is the term given to multiple independent pp collisions that may occur within each LHC bunch crossing. Pileup is simulated by overlaying multiple event generation chains, each including the steps listed above. The average number of interactions per bunch crossing, $\langle\mu\rangle$, varies across the LHC Run 2 dataset and generated events are reweighted according to the difference between data and MC.

4.1.6 Detector simulation

In order to fairly compare ATLAS data and simulated events, MC-generated events must be passed through a simulation of the ATLAS detector. At this point in the event simulation chain, there is the necessary kinematic information for all the final-state particles. The ATLAS detector simulation [80] is built with GEANT4 [81, 82] and contains packages that simulate the response of each hardware component. The simulation of the physics interactions of particles within the detector records the particle trajectory and the deposited energy, in steps until the particle has zero energy or has gone out of the detector acceptance. Then, digitisation of the energy deposits into voltage and current signals is required to match the same readout recorded for data. At this stage, the simulation is in the equivalent format to the data and can be processed with reconstruction software to produce the physics objects discussed in Chapter 5.

4.2 Particle- and parton-level

Due to the sequential nature of MC event simulation where information is retained at each step, it is possible to compare theoretical predictions (simulated events) with data at different points in the evolution of a particle collision event. Given that final-state partons are often unstable and decay to other particles, we can define:

- **parton-level**, where there are quarks and gluons in the final state and additional radiation has been corrected for in data. For a $t\bar{t}Z$ event, the parton-level is before the decay of the top-quarks and Z-boson.
- **particle-level**, after the parton shower and hadronisation, where there are hadrons or leptons in the final state and all unstable particles have decayed.
- **detector-level**, where the impact of the detector, such as its limited resolution, is included through a detector simulation.

The definition of the parton-level is useful because state-of-the-art calculations often treat top-quarks as stable particles, and we wish to compare theoretical and experimental results. The particle-level is expected to be the closest to what could be measured with a 'perfect' detector. Measurements at particle- and parton-level can also be compared to the results of other experiments, such as CMS, which is not possible at detector-level. In simulated events, particle- and parton-level are sometimes referred to as the *truth-level*. The research described in this thesis measures the differential cross-sections of $t\bar{t}Z$ at both particle- and parton-level.

Chapter 5

Object reconstruction

The ATLAS detector records energy and position information from particles as they travel through various subdetector layers. Different particles have different responses in the detector. The raw event information must be processed, thereby constructing physics objects, in order to perform physics analyses. For this analysis, the low-level objects that are derived from the energy deposits and spatial hits recorded by the detector are tracks and topological clusters. Reconstruction algorithms are used to build physics objects from these low-level objects. The physics objects that must be reconstructed in the measurement of $t\bar{t}Z$ are leptons, jets of hadronic particles, and missing transverse energy.

5.1 Inner detector tracks and vertices

The trajectories, or tracks, of charged particles, can be constructed from hits in the inner detector. Charged particles travelling through the inner detector layers cause detector hits. Nearby hits are grouped to form three-dimensional *space points*, which is done separately in the pixel layer and in the SCT [83]. The following track candidate search is an iterative process and uses a *track-seed*, formed from three space-points, as its input. Extrapolating the trajectory of the track candidate, a combinatorial Kalman filter [84] is used to include successive hits in the track candidate fit. Multiple track candidates are found from a single

track-seed, with some sharing space-points and making them incompatible. Therefore, an iterative likelihood-based ambiguity-solving algorithm is used to reject some track candidates. The resolved track candidates are then extended to the TRT. The track candidates must satisfy the following criteria:

- $p_T > 400\,\text{MeV}$,
- $|\eta| < 2.5$,
- minimum of 7 pixel and SCT clusters,[1]
- maximum of either one shared pixel cluster or two shared SCT clusters in the same layer,
- $|z_0 \sin\theta| < 3\,\text{mm}$,
- $d_0 < 2\,\text{mm}$,
- fewer than three holes [2] in the combined pixel and SCT subdetectors,
- fewer than two holes in the pixel subdetector,

where the transverse impact parameter, d_0, is calculated with respect to the measured beamline position, z_0 is the longitudinal impact parameter along the beamline between the point where d_0 is measured and the primary vertex, and θ is the polar angle of the track [85].

Tracks in the inner detector are used to find the primary vertex, defined as the intersection of multiple tracks (vertex) with the largest sum of squared transverse momentum, $\sum p_T$, over all associated tracks. The primary vertex is attributed to the point of hard scatter in the pp collisions. Other vertices are classed as secondary vertices and are attributed to the decay of long-lived particles, such as b-hadrons, or pileup background.

[1] Clusters are groups of pixels and strips with a common edge that are used to construct space-points.
[2] Holes are defined as areas where a reconstructed track trajectory intersects with a sensitive detector element but does not have a matching cluster.

5.2 Leptons

Leptons, unless stated otherwise, will refer to electrons and muons. Tau leptons are not used explicitly in the measurement of $t\bar{t}Z$, though electron and muon candidates that may have originated from tau lepton decay are not excluded.

5.2.1 Electrons

Electron candidates are reconstructed by matching tracks in the inner detector to energy deposits in the LAr calorimeter. The signals in individual calorimeter cells are sequentially grouped to form clusters. The topological cluster (*topo-cluster*) approach forms dynamic and variable-size clusters [86, 87]. This approach includes bremsstrahlung radiation, the emission of a low-energy photon ($\sim 100\,\text{MeV}$) upon an electron interacting with detector material, in the clustering algorithm. The basis of the topo-cluster algorithm is the cell significance, $\zeta_{\text{cell}}^{\text{EM}}$, which is computed as

$$\zeta_{\text{cell}}^{\text{EM}} = \left| \frac{E_{\text{cell}}^{\text{EM}}}{\sigma_{\text{cell,noise}}^{\text{EM}}} \right|, \tag{5.1}$$

where $E_{\text{cell}}^{\text{EM}}$ is the absolute cell energy at the electromagnetic scale, which is the baseline calorimeter scale that correctly measures energy depositions from electromagnetic showers and $\sigma_{\text{cell,noise}}^{\text{EM}}$ is average cell noise in simulated events. *Protoclusters* are formed using a set of noise thresholds in the so-called "4-2-0" approach and combined into topo-clusters as described in Ref. [86]. Then, the *supercluster* algorithm is used to connect topo-clusters with low-energy Bremsstrahlung photons. The highest-p_T topo-clusters can be used as a seed in the supercluster algorithm if they have an energy of over 1 GeV and a corresponding track with at least four hits in the inner detector. A multivariate calibration of the cluster energy based on simulated $Z \to e^+e^-$ events is applied [88, 89]. Electron candidates are defined as superclusters with an associated track, which is matched to the cluster using variables that are related to the distance between the track and cluster [86].

In order suppress charge-misidentified electrons and non-prompt leptons,[3] the electron candidate track must have $|\Delta z_0 \sin\theta| < 0.5\,\text{mm}$ and $|d_0|/\sigma_{d_0} < 5$ where σ_{d_0} is the uncertainty associated with d_0. Calibrated electrons must satisfy isolation and identification requirements. A likelihood-based algorithm is used to identify prompt leptons and reject non-prompt background, defining `VeryLoose`, `Loose`, `MediumAndBLayer`, `Medium` and `Tight` selections. Electrons are required to satisfy the `Medium` likelihood requirement which has an average efficiency of around 80% [89]. They are also required to have $p_T > 7\,\text{GeV}$ and $|\eta| < 2.47$. In order to identify prompt leptons, a set of isolation criteria are defined via a multivariate algorithm. The prompt lepton veto (PLV) is a boosted decision tree (BDT) that uses isolation and lifetime variables to separate $t\bar{t}$ events from background processes [90]. A set of isolation working points is defined from the BDT discriminant and the `PLVLoose` working point is required for electrons.

Differences in efficiency between data and simulated events are corrected with scale factors that take into account the electron identification, isolation and reconstruction efficiencies [91, 92]. The electron energy scale is corrected in data using a large sample of $Z \to e^+e^-$ events and the difference between the energy resolution in simulation and data is corrected for in simulation [93].

5.2.2 Muons

The inner detector, muon spectrometer and calorimeter subdetectors can all be used to reconstruct muons. For muons used in the measurements described in this thesis, tracks are reconstructed in the inner detector and muon spectrometer independently before a global refit is performed using hits from both subdetectors. Muon candidate tracks in the muon spectrometer are constructed by firstly forming segments, tracks in a single layer of the muon spectrometer, from hits in each muon chamber. In the MDT chambers, a Hough transform [94] is used to find hits on a trajectory in the bending plane of the detector before segments are formed via a straight-line fit. The RPC or TGC hits are used to measure the coordinate that is orthogonal to the bending plane. In the CSC, segments are found via a combinatorial search in the η and ϕ planes using a loose requirement on the compatibility between the track and luminous region [95]. Once hits in segments are found, these are used in a combinatorial segment-seeded search

[3] Non-prompt leptons are physics objects that are misreconstucted as leptons.

algorithm to build muon track candidates. There must be two matching segments in order to construct a muon track candidate, apart from the barrel-endcap transition region where one high-quality segment and ϕ and η information is sufficient. The resulting reconstructed muons in the muon spectrometer are then extrapolated inward and matched to a track in the inner detector. A combined track fit is performed on the matched inner detector and muon spectrometer hits, allowing for the muon spectrometer hits associated with the combined track to be updated if it improves the fit [96].

Similarly to electrons, calibrated muon candidates must satisfy isolation and identification criteria. Muon candidates must have $p_T > 7\,\text{GeV}$, $|z_0 \sin\theta| < 0.5\,\text{mm}$, $|d_0|/\sigma_{d_0} < 3$, $|\eta| < 2.5$ and satisfy `Medium` identification quality requirements and `PLVLoose` isolation requirements [90, 95]. The reconstruction and identification efficiency of the `Medium` working point has an efficiency of over 90% for muons with p_T greater than 5 GeV [95]. Corrections to the muon momentum scale and resolution are applied to address differences between simulated $Z \to \mu^+\mu^-$ and $J\backslash\Psi \to \mu^+\mu^-$ and observed data [97, 95]. The *tag-and-probe* method is used to derive efficiency scale factors for the isolation, identification and track-to-vertex reconstruction as described in Ref. [96].

5.3 Jets

Due to colour confinement in QCD, quarks and gluons, which possess colour charge, must form colour-neutral hadronic bound states. Unlike leptons, quarks and gluons from pp collisions, are not detected as isolated particles, but rather a collimated shower of particles called jets. Jets are reconstructed from the combination of tracks in the inner detector and topo-clusters in the calorimeters via the particle flow (`PFlow`) algorithm and *particle-flow objects* [98]. Topo-clusters from the hadronic calorimeter are formed following the same procedure as topo-clusters in the electromagnetic calorimeter, as described in Section 5.2.1. The use of tracking information in the `PFlow` algorithm exploits the superior momentum resolution for low p_T objects provided by the tracking detector and increases robustness against pileup background. Any tracks that are used in both electron and jet reconstruction are dealt with via an *overlap removal* procedure that removes particles based on shared tracks and ΔR proximity to other particles.

The anti-k_T algorithm [99] is then used to reconstruct jets via sequential recombination based on a distance parameter, d_{ij}, between two objects i and j such that

$$d_{ij} = \min(k_{t,i}^{2p}, k_{t,j}^{2p}) \frac{\Delta R_{i,j}^2}{R^2}, \tag{5.2}$$

where $\Delta R_{i,j}^2 = (y_i - y_j)^2 + (\phi_i - \phi_j)^2$ and $k_{t,i}$ is the transverse momentum, y_i the rapidity and ϕ_i the azimuthal angle of object i, R is a variable radius parameter and p is a parameter of the algorithm set, for the anti-k_T case, to be equal to minus one. A further distance parameter, d_{iB}, is defined as

$$d_{iB} = k_{t,i}^{2p}, \tag{5.3}$$

or the distance between the beamline and object i. For each set of objects i and j, both d_{ij} and d_{iB} are calculated. If d_{iB} is the smaller of the two, then i is considered a jet candidate. Otherwise, clusters i and j are merged to create a pseudo-jet. This process continues iteratively with the remaining topo-clusters and pseudo-jets until all input particle-flow objects are clustered into jets. For this analysis, and for most ATLAS analyses, $R = 0.4$. The anti-k_T algorithm is infrared and collinear safe, meaning that the reconstruction is invariant under additional soft radiation and also under the additional emission of radiation that is collinear to the jet [100].

Jets are calibrated to account for differences in the calorimeter response between simulated events and data. The jet response in the calorimeters is always less than perfect - some energy is not recorded. This gives rise to an energy offset in reconstructed jets that is corrected for in simulated events [101]. To account for this, precisely-measured processes are used as references in three distinct areas of phase space in order to calibrate the p_T response of each jet. The jet energy resolution is measured in data and simulation, then additional smearing is applied to simulation such that the resolution agrees with data measurements [102].

Jet candidates are required to have $p_T > 25\,\text{GeV}$ and $|\eta| < 2.5$. In order to reject jets originating from pileup background, a multivariate jet vertex tagger (JVT) [103, 104] is used. Jet candidates with $p_T < 60\,\text{GeV}$, $|\eta| < 2.4$ and JVT discriminant < 0.5 are rejected in order to reduce low-p_T pileup background.

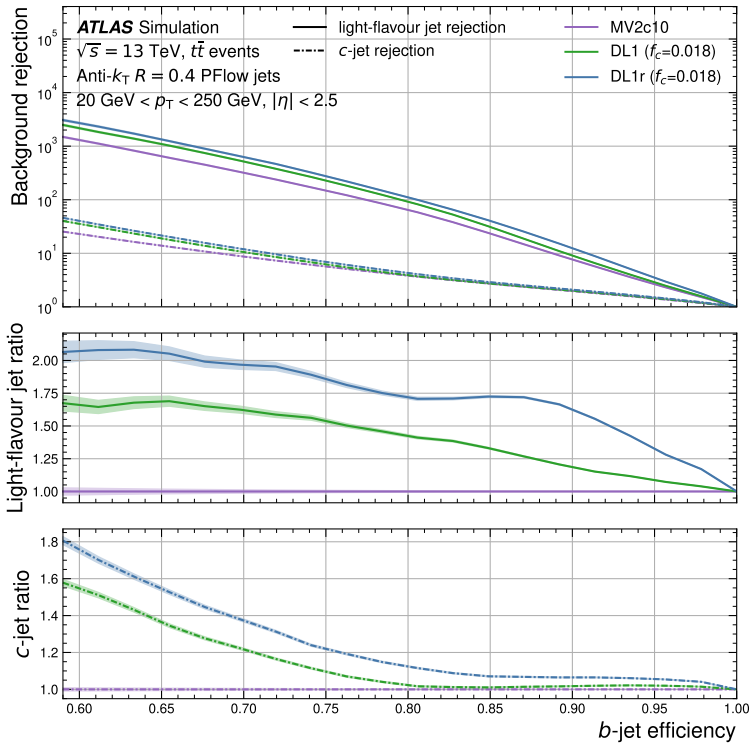

Figure 5.1: Light- and c-jet rejection factors as a function of b-jet tagging efficiency for the high-level b-taggers used by ATLAS. The lower two panels show the light- and c-jet rejection relative to that of `MV2c10` [105].

5.3.1 *b*-tagging

As well as light-flavour jets, jets from b-hadron decay are also present in the ATLAS detector. Given that top quarks virtually always decay to b-quarks, it is important to be able to identify b-jets over those originating from light-flavour (u, d, s) and c-quarks; this is called *b-tagging*. Flavour-tagging algorithms used in ATLAS typically have two levels. Firstly, low-level algorithms are used to analyse properties of tracks and vertices [105]. Then, the outputs of low-level algorithms can be used along with kinematic information as inputs to high-level multivariate algorithms. For this analysis, we use the high-level algorithm `DL1r`, which employs a recurrent neural network to discriminate between b- and c- or light-flavour jets [106]. The most important variables are the presence of secondary vertices and the correlation between the impact parameters of tracks. As well as correctly identifying b-jets, it is important that the algorithm simultaneously rejects light- and c-jets. Figure 5.1 shows the light- and c-jet rejection

as a function of the b-tagging efficiency for the DL1r flavour-tagging algorithm relative to an older high-level algorithm, MV2c10. The DL1r discriminant is used to provide a set of thresholds that tag b-jets with corresponding efficiencies of 60%, 70%, 77% and 85%. The background rejection is equal to 1/(light- or c-jet efficiency). As an example, the 77% working point has a light-jet rejection of up to 270 and a c-jet rejection of up to 7 (p_T dependent), corresponding to efficiencies of 0.4% and 14% respectively. The efficiency of the DL1r algorithm is calibrated to account for the differences in data and simulation for $t\bar{t}$ and Z+jets events. This can be done for each working point separately (fixed-order) or as a function of the four working points (pseudo-continuous). Fixed-order b-tagging means that only a single working point can be used to select objects in an event for analysis, whereas pseudo-continuous b-tagging allows for the use of more than one working point. The analysis presented in this thesis makes use of the latter strategy.

5.4 Missing transverse energy

The partons associated with protons colliding at the LHC each carry an unknown momentum fraction, so it is not possible to know the total expected momentum of a given collision. However, momentum conservation dictates that, assuming the colliding partons are perfectly aligned along the beamline, the transverse momenta of all objects in the event will sum to zero. Particles such as neutrinos do not interact with the detector, due to their neutral charge and low mass, though their presence can be inferred via missing transverse momentum. Searching for top-quark decays in leptonic final states means that we expect some missing transverse momentum from a neutrino. The missing transverse energy, $E_{\mathrm{T}}^{\mathrm{miss}}$, associated with a given event is defined as the absolute value of the negative vectorial sum of the transverse (x-y plane) momenta of all identified and calibrated physics objects. The first term of the E_T^{miss} is from the hard-scatter event, consisting of reconstructed and calibrated jets, electrons, photons, tau leptons and muons. The second term is from the soft-event: reconstructed charged-particle tracks associated with the hard-scatter vertex, but not with the physics objects listed in the first term [107]. Tables 5.1 and 5.2 summarise the object selection for leptons and jets, respectively.

Table 5.1: Summary of the electron and muon object definitions. Electrons in the transition region between the EMEC and HEC of the LAr calorimeter are rejected in order to reduce non-prompt electrons.

	Pre-selected Electron	**Pre-selected Muon**
Acceptance	$p_T > 7\,\text{GeV}$, $\lvert\eta\rvert < 2.47$ except $1.37 < \lvert\eta\rvert < 1.52$	$p_T > 7\,\text{GeV}$, $\lvert\eta\rvert < 2.5$
Quality	`LooseAndBLayerLH`	`Medium`
Impact parameter	$\lvert d_0\rvert/\sigma_{d_0} < 5$ $\lvert z_0 \sin\theta\rvert < 0.5$ mm	$\lvert d_0\rvert/\sigma_{d_0} < 3$ $\lvert z_0 \sin\theta\rvert < 0.5$ mm
	Signal Electron	**Signal Muon**
Quality	`MediumLH`	`Medium`
Isolation	`PLVLoose`	`PLVLoose`

Table 5.2: Summary of the jet selection criteria and b-tagging.

Jet	
Collection	`AntiKt4EMPFlow`
Acceptance	$p_T > 25\,\text{GeV}$, $\lvert\eta\rvert < 2.5$
Jet Vertex Tagger	reject jets with $p_T < 25\,\text{GeV}$, $\lvert\eta\rvert < 2.4$ and JVT < 0.5
***b*-tagged jet**	
Acceptance	$p_T > 25\,\text{GeV}$, $\lvert\eta\rvert < 2.5$
b-tagging	85% efficiency, `DL1r`

5.5 $t\bar{t}$ reconstruction

Top quarks, and the $t\bar{t}$ system, must be reconstructed from its decay products. In the trilepton channel, the $t\bar{t}$ system decays in the single-lepton mode where one W-boson decays leptonically and the other hadronically. The leptonic and hadronic 'sides' are reconstructed separately, with the leptonic W-boson reconstruction taking precedence. The lepton not associated with the Z-boson and the $E_{\text{T}}^{\text{miss}}$ associated with the event is used to find the neutrino four-vector such that the $\ell\nu$ invariant mass is equal to the W-boson mass. The b-jet with the smallest ΔR separation from the $\ell\nu$ system is then combined with the W-boson to reconstruct the top-quark.

For the hadronic side, the invariant mass of pairs of light jets is calculated and the pair that best matches the W-boson mass is chosen to reconstruct the W-boson. The reconstructed W-boson is combined with the b-jet not used in the leptonic-side reconstruction.

In the tetralepton channel, the $t\bar{t}$ system decays in the dileptonic mode, making $t\bar{t}$ reconstruction challenging due to the presence of two neutrinos in the final state. Both neutrinos contribute to missing transverse momentum and the four-momentum vectors of the neutrinos have many possible solutions. The two-neutrino scanning method (2νSM) is used to find the mostly likely solution [1]. Kinematic information of the two leptons not associated with the Z-boson and of the two b-jets are used as input. Firstly, values of the neutrino η and ϕ are found by systematically scanning over possible values and retaining those that are consistent with the η of the combined $bb\ell\ell$ system. Possible kinematic solutions are reduced further by applying constraints on the $\Delta R(\ell, \nu)$ based on the sum of the transverse momentum of both charged leptons. The neutrino transverse momenta are then calculated for the remaining solutions. Top-quark candidates are constructed from all possible combinations of the b-jets, charged leptons and neutrinos. A weight is assigned to each top-quark candidate based on i) the probability of obtaining the reconstructed top-quark mass from a reference top-quark mass distribution built from parton-level objects and ii) the differences between measured x and y components of the $E_{\mathrm{T}}^{\mathrm{miss}}$ and the corresponding parton-level neutrino p_T components. The combination of reconstructed objects and neutrinos with the highest weight over both top-quark candidates is chosen as the reconstructed $t\bar{t}$ system.

Chapter 6

Signal and background

In order to precisely measure the $t\bar{t}Z$ differential cross-sections, events are selected from the full Run 2 dataset that contain physics objects expected in $t\bar{t}Z$ trilepton and tetralepton final states. These final states are referred to as the *signal* process. There are multiple SM processes that can have the same reconstructed final-state objects as $t\bar{t}Z$ events and these are referred to collectively as *background* processes. Simulated events are used to define regions of phase space that are $t\bar{t}Z$-enriched and to estimate the contribution of background processes. This chapter describes the simulated event samples for the $t\bar{t}Z$ signal (Section 6.1) and for each important background process (Section 6.2). Multivariate techniques are used to separate $t\bar{t}Z$ signal from background in each channel, defining measurement signal regions (Section 6.3).

MC event samples, generated using the steps described in Chapter 4, are used to model the signal and background processes. Some settings in the simulated samples are common across the signal and background: the value of the top-quark mass, the effect of multiple interactions and pileup, and the use of either the full or fast detector simulation. The top-quark mass is set to 172.5 GeV in all MC samples. The effect of multiple interactions in the same and neighbouring bunch crossings is modelled by overlaying each simulated hard-scattering event with inelastic pp events generated with Pythia 8.186 [108] using the NNPDF2.3lo set of parton distribution functions [109] and the `A3` set of tuned parameters [110]. Separate MC production campaigns are used to model the different pileup distributions observed in data during 2015/16, 2017 and 2018. The simulated event samples are reweighted to reproduce the observed distribution of

the average number of collisions per bunch crossing in each data-taking period. The simulation of the ATLAS detector is performed with either a full detector simulation [111] based on the GEANT4 [81] framework or a fast simulation (ATLFAST II) using a parameterisation of the performance of the electromagnetic and hadronic calorimeters [112] and GEANT4 for the other detector components [81].

6.1 Signal

The production of a $t\bar{t}$ pair in association with a leptonically-decaying Z-boson is modelled using the MADGRAPH5_aMC@NLO 2.8.1 generator [113], which produced matrix elements at NLO with the NNPDF3.0NLO PDF set [109]. The interference between $\gamma^* \to \ell^+\ell^-$ and Z/γ^* is included down to 5 GeV in dilepton invariant mass. The functional form of the renormalisation and factorisation scales (μ_R and μ_F) is set to $0.5 \times \sum_i \sqrt{m_i^2 + p_{\mathrm{T},i}^2}$, where the sum index, i, runs over all the particles generated from the matrix element calculation. The events are interfaced with PYTHIA 8.244 [73] for the simulation of the parton shower, hadronisation, and underlying event, using the `A14` set of tuned parameters and the NNPDF2.3LO PDF set. The decays of b- and c-hadrons are simulated using the EVTGEN 1.7.0 program [114].

It is possible that the choice of nominal MC event generator can bias the differential cross-section measurements. To estimate theoretical modelling uncertainties in the signal prediction, several alternative $t\bar{t}Z$ MC samples are considered. These include a sample generated with the same MADGRAPH5_aMC@NLO version as the nominal sample, but interfaced to HERWIG 7.2.1 [75] for the simulation of the parton shower. Two additional samples with the same settings as the nominal $t\bar{t}Z$ sample, except for upward and downward variations of the `Var3c` variation of the `A14` tune, are used to evaluate uncertainties associated with the modelling of initial-state radiation. The `Var3c` variation corresponds to a variation of α_s for initial-state radiation in the `A14` tune. Alternative samples generated with SHERPA are used for comparisons with the measured differential cross-section distributions. A $t\bar{t}Z$ sample is produced with the SHERPA 2.2.1 generator [74] at NLO accuracy. Another sample is produced with a newer version of the same generator, SHERPA 2.2.11, together with the MEPS@NLO matching algorithm [115, 116, 117], which performed the multi-leg merging of up to three additional

partons with the parton shower at LO, with a merging scale of 30 GeV. These samples also include off-shell effects down to 5 GeV in the invariant mass of the lepton pair. The SHERPA parton shower is used along with the NNPDF3.0NNLO PDF set. The fast detector simulation is used for the alternative $t\bar{t}Z$ samples.

6.2 Backgrounds

Background processes can be split into two categories: those with prompt or non-prompt leptons, where the term 'prompt' refers to leptons which are directly produced by the hard-scatter process or by the decays of heavy resonances such as Z, W or Higgs bosons. Non-prompt lepton sources include leptons that come from b-jets and jets that are misreconstructed as leptons. To estimate background processes in data, control regions (CRs) are defined that are enriched in important backgrounds. The shape of the background distribution is found using simulated events. The control regions are included in the fit when extracting the differential cross-section, in order to measure background normalisation factors simultaneously with the cross-section.

6.2.1 Prompt lepton background

In both of the trilepton and tetralepton channels, there are three main types of background: diboson processes (WZ+jets, ZZ+jets), single top-quark and vector boson processes (tZq, tWZ) and top-quark pair and W/Higgs boson production (ttW, ttH). The diboson backgrounds in both channels can be further categorised by the flavour of the associated jets (b/c/light). Other smaller backgrounds in the signal regions are grouped together in a separate category.

The tetralepton channel has small expected contributions from SM background processes. In particular, tetralepton events which have a different-flavour non-Z lepton pair suffer little background. For tetralepton events with a same-flavour non-Z lepton pair, the ZZ+jets process (with $ZZ \to \ell^{\pm}\ell^{\mp}\ell^{\pm}\ell^{\mp}$) is the largest expected background. In the trilepton channel, the dominant expected background processes are WZ+jets (with $WZ \to \ell\ell\ell\nu$) and tZq production.

The single largest background is WZ plus at least one b-jet ($WZ + b$). The following sections describe the MC event samples used to predict the prompt lepton backgrounds in both channels.

Diboson

Diboson processes producing either three charged leptons and one neutrino or four charged leptons (WZ+jets or ZZ+jets, respectively) are simulated using the Sherpa 2.2.2 generator with the NNPDF3.0nnlo PDF set. Multiple matrix elements are matched and merged with the Sherpa parton shower based on the Catani–Seymour dipole factorisation scheme [118] using the MEPS@NLO prescription [119]. Virtual QCD corrections for NLO matrix elements are provided by the OpenLoops library [120]. The WZ/ZZ+jets events with less than two additional partons are simulated at NLO, whereas events with two or three additional partons are simulated at LO precision.

Top-quark with vector bosons

In the tetralepton channel, the second-largest background is the production of single top quarks in association with a W-boson and Z-boson (tWZ). This process is modelled with MadGraph5_aMC@NLO 2.2.2 at NLO with the NNPDF3.0nlo PDF set. The nominal tWZ sample follows the "diagram removal 1" (DR1) scheme described in Ref. [121]. Diagram removal accounts for the overlap of $t\bar{t}Z$ and tWZ at NLO. An alternative sample is generated within the DR2 scheme, which also considers the interference terms between single- and double-resonant $t\bar{t}$ production, as described in Ref. [121]. The alternative sample is used to evaluate uncertainty from the modelling of the tWZ process, as described in Chapter 9.

In the trilepton channel, one of the largest backgrounds is the production of single top quarks in association with a Z-boson (tZq). This process is modelled with the MadGraph5_aMC@NLO 2.9.5 generator at NLO with the NNPDF3.0nlo PDF set. The tZq events are interfaced with Pythia 8.245, and the tWZ events with Pythia 8.212, using the `A14` tune and the NNPDF2.3lo PDF set. The tZq sample includes off-shell effects down to 5 GeV in dilepton invariant mass.

Top-quark pair with a W or Higgs boson

In both the trilepton and tetralepton channels, the production of a $t\bar{t}$ pair in association with a Higgs boson ($t\bar{t}H$) is a minor background. This event sample is generated using NLO matrix elements in MadGraph5_aMC@NLO 2.6.0 with the NNPDF3.0nlo PDF set interfaced with Pythia 8.230 for the parton shower, using the `A14` tune. The fast detector simulation is used for the nominal prediction of the $t\bar{t}H$ process.

The production of a $t\bar{t}$ pair in association with a W-boson ($t\bar{t}W$) is a minor background in the trilepton channel. This process is generated with Sherpa 2.2.10 and the NNPDF3.0nnlo PDF set. MEPS@NLO performs multi-leg merging of up to one additional parton at NLO and up to two additional partons at LO, with a merging scale of 30 GeV.

Other

Several other background processes with very small contributions to the trilepton and tetralepton prompt background are grouped together. Event samples featuring the production of a Higgs boson in association with a W- or Z-boson are generated at LO with Pythia 8.186 using the `A14` tune and the NNPDF2.3lo PDF set. Three top-quark production ($tt\bar{t}$) and the production of a $t\bar{t}$ pair with two W-bosons ($t\bar{t}WW$) are simulated at LO using MadGraph 2.2.2 interfaced to Pythia 8.186 with the `A14` tune and the NNPDF2.3lo PDF set. Four top-quark production ($t\bar{t}t\bar{t}$) is simulated at NLO using MadGraph5_aMC@NLO 2.3.3 interfaced to Pythia 8.230 with the `A14` tune and the NNPDF3.1nlo PDF set; an alternative sample uses the Herwig 7.04 parton shower instead. Processes with three heavy gauge bosons (WWW, WWZ, WZZ and ZZZ) yielding up to six final-state leptons are simulated with Sherpa 2.2.2 and the NNPDF3.0nlo PDF set. Final states with no additional partons are calculated at NLO, whereas final states with one, two or three additional partons are calculated at LO.

Table 6.1 summarises the MC generators used to produce the nominal signal and background samples used in the $t\bar{t}Z$ differential cross-section measurements.

Table 6.1: Versions of the generator, parton shower and PDF set used for the nominal MC samples used in the analysis.

Process	Generator	Parton shower	PDF
$t\bar{t}Z$	MadGraph5_aMC@NLO 2.8.1	Pythia 8.244	NNPDF3.0nlo
WZ/ZZ	Sherpa 2.2.2	Sherpa 2.2.2	NNPDF3.0nnlo
tZq	MadGraph5_aMC@NLO 2.9.5	Pythia 8.245	NNPDF3.0nlo
tWZ	MadGraph5_aMC@NLO 2.2.2	Pythia 8.212	NNPDF2.3lo
$t\bar{t}H$	MadGraph5_aMC@NLO 2.6.0	Pythia 8.230	NNPDF3.0nlo
$t\bar{t}W$	Sherpa 2.2.10	Sherpa 2.2.10	NNPDF3.0nnlo
$t\bar{t}t\bar{t}$	MadGraph5_aMC@NLO 2.3.3	Pythia 8.230	NNPDF3.1nlo
$tt\bar{t}$	MadGraph 2.2.2	Pythia 8.186	NNPDF2.3lo
VH	Pythia 8.186	Pythia 8.186	NNPDF2.3lo
VVV	Sherpa 2.2.2	Sherpa 2.2.2	NNPDF3.0nlo

6.2.2 Non-prompt lepton background

In order to estimate the contribution to background events from non-prompt - or "fake" - leptons,[1] a semi-data-driven background fit is performed in dedicated control regions. As mentioned at the beginning of this chapter, fake leptons are objects unintentionally misidentified as leptons in the $t\bar{t}Z$ final state. They can originate from various sources including meson decays, photon conversions or light jets, creating lepton-like detector signatures. For $t\bar{t}Z$ events, the fake lepton background is largest in the trilepton channel, where $t\bar{t}$ and a W- or Z-boson with heavy-flavour hadrons, $t\bar{t}$, Z+jets and W+jets backgrounds with fake leptons can mimic a $t\bar{t}Z$ final state.

A *template fit* method is used to normalise fake leptons from different sources to data. This method relies on MC templates, one for each source of fake leptons, created using MC truth information containing the origin and type of the fake leptons. Four distinct MC templates are defined based on the major source of fakes for this analysis: electrons from heavy-flavour sources ("F-e-HF"), muons from heavy-flavour sources ("F-μ-HF"), electrons from other sources ("F-e-Other"), and any other events containing a fake lepton and not belonging to the other categories or events containing multiple fake leptons ("F-Other"). In order to get the best

[1] Also referred to as "fakes".

estimate of the fake lepton background, it is important to define fake lepton control regions that are kinematically similar to the measurement signal regions (SRs), described in Section 6.3, while remaining orthogonal. A set of trilepton control regions (CRs) are designed that require exactly three leptons with $p_T > 27,\ 20,\ 15\,\text{GeV}$, at least one b-jet tagged with 85% efficiency and at least three jets. In contrast to the signal region selection, there must be exactly one lepton that fails the identification and isolation requirements applied to signal leptons. This lepton is referred to as the "loose" lepton. Two control regions that are dominated by $t\bar{t}$ are selected to enrich the contribution from fake leptons from heavy-flavour decays. Events with an OSSF lepton pair are removed and the flavour of the loose lepton (e/μ) is then used to categorise events into two regions: CR-$t\bar{t}$-e and CR-$t\bar{t}$-μ. A third control region that is dominated by $Z \to \ell\ell$ is defined to estimate the contribution from fake electrons from other sources, CR-Z-e. Events in this control region have exactly three electrons, two of which form an OSSF pair, and $E_{\text{T}}^{\text{miss}}$ less than 80 GeV. This region targets events with a Z-boson plus a fake electron in order to estimate the F-e-Other background. The fake lepton control region selection criteria are summarised in Table 6.2.

Table 6.2: Definition of the trilepton fake lepton control regions.

Variable	**Preselection**		
N_ℓ $(\ell = e, \mu)$	$= 3$, of which one is loose		
p_T (ℓ_1, ℓ_2, ℓ_3)	$> 27,\ 20,\ 15$ GeV		
Sum of lepton charges	± 1		
N_{jets} $(p_T > 25$ GeV)	≥ 3		
$N_{b-\text{jets}}$	≥ 1@85%		
	CR-$t\bar{t}$-e	**CR-$t\bar{t}$-μ**	**CR-Z-e**
Lepton flavour	no OSSF pair (loose e)	no OSSF pair (loose μ)	OSSF pair (exactly 3 e)
$E_{\text{T}}^{\text{miss}}$	—	—	< 80 GeV

The F-e-HF, F-e-Other and F-μ-HF templates are normalised in data simultaneously with the differential cross-section measurement. In the CR-$t\bar{t}$-e and CR-$t\bar{t}$-μ regions, the total event yields are used in the fit. In the CR-Z-e region, the sum of the transverse momentum of the trailing lepton and the missing transverse energy is fitted in six bins as this distribution has

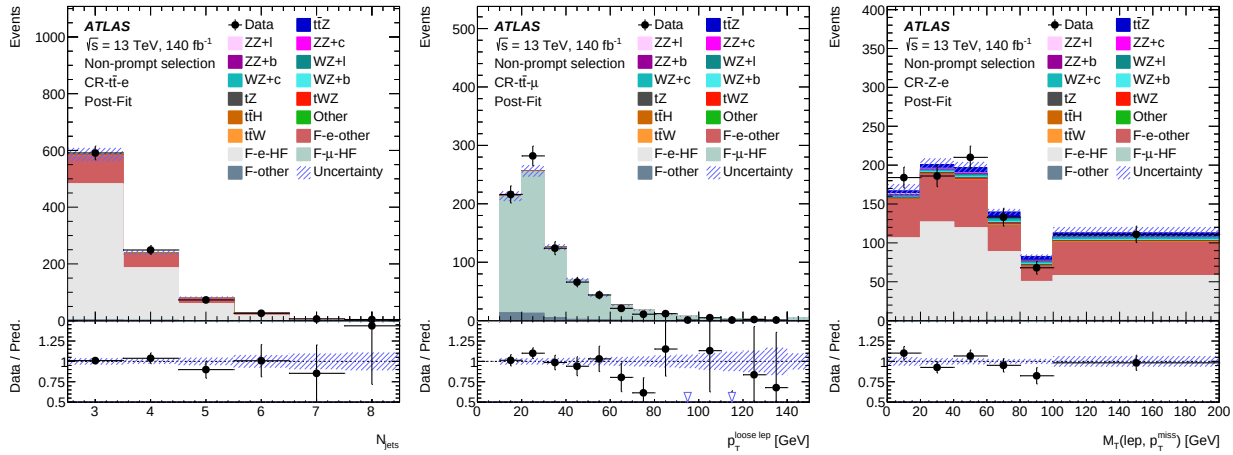

(a) CR-$t\bar{t}$-e **(b)** CR-$t\bar{t}$-μ **(c)** CR-Z-e

Figure 6.1: Post-fit distributions of the (a) number of jets in CR-$t\bar{t}$-e, (b) transverse momentum of the loose lepton in CR-$t\bar{t}$-μ and of (c) the transverse mass of the trailing lepton and the missing transverse momentum in CR-Z-e when fitted independently from the differential cross-section measurements. The last bins include overflow events. The distributions (a) and (b) are not used in the fit, instead an overall event yield in each of these regions is fitted.

some mild separation power between the F-e-Other and F-e-HF backgrounds, the latter of which is already well-estimated in the CR-$t\bar{t}$-e region. Events in the F-Other category, which are not normalised in data, are assigned a conservative 50% normalisation uncertainty. The extraction of three fake normalisation factors $\mathcal{N}_{e,\mathrm{HF}}$, $\mathcal{N}_{\mu,\mathrm{HF}}$ and $\mathcal{N}_{e,\mathrm{other}}$ is initially performed in the fake lepton control regions independently of the cross-section measurement. Detector-level kinematic distributions showed a small (less than 20%) non-closure between data and prediction in some bins when the fit was performed in the fake lepton control regions only. An additional uncertainty is applied to the fake templates in the signal regions to cover the non-closure: 20% on fake electrons and 10% on fake muons. Figure 6.1 shows the post-fit distributions in the fake lepton control regions. The corresponding event yields are shown in Table 6.3.

The values of the fake lepton normalisation factors fitted independently from the differential cross-section measurements can be seen in Table 6.4. The $\mathcal{N}_{\mu,\mathrm{HF}}$ and $\mathcal{N}_{e,\mathrm{other}}$ normalisation factors are consistent with the SM prediction and the $\mathcal{N}_{e,\mathrm{HF}}$ normalisation factor fits slightly lower than the SM prediction. The F-μ-HF and F-e-HF backgrounds have comparable normalisation uncertainty at just under 10% while the uncertainty on the F-e-Other background is closer to

Table 6.3: Observed and expected event yields in the fake lepton control regions after the combined fit to data, where the dash indicates a yield smaller than 0.1. The indicated errors include MC statistical uncertainty and systematic uncertainties discussed in Chapter 9.

	CR-$t\bar{t}$-e	CR-$t\bar{t}$-μ	CR-Z-e
$t\bar{t}Z$	2.53 ± 0.21	0.71 ± 0.12	33.5 ± 1.4
$ZZ + l$	–	–	3.8 ± 1.1
$ZZ + c$	–	–	2.99 ± 0.95
$ZZ + b$	–	–	3.5 ± 1.8
$WZ + l$	0.29 ± 0.13	–	7.8 ± 3.1
$WZ + c$	0.36 ± 0.13	–	11.2 ± 4.3
$WZ + b$	0.16 ± 0.10	–	5.8 ± 3.3
tZq	0.21 ± 0.05	–	6.55 ± 0.99
tWZ	0.26 ± 0.04	–	3.81 ± 0.41
$t\bar{t}H$	4.46 ± 0.38	2.31 ± 0.20	3.20 ± 0.29
$t\bar{t}W$	2.9 ± 1.5	1.50 ± 0.75	1.41 ± 0.71
Other	1.2 ± 0.54	0.72 ± 0.32	0.52 ± 0.23
F-e-HF	749 ± 70	–	548 ± 56
F-μ-HF	0.25 ± 0.02	744 ± 31	–
F-e-Other	177 ± 50	–	267 ± 72
F-Other	3.0 ± 1.4	36 ± 16	1.03 ± 0.52
Total	943 ± 30	786 ± 28	901 ± 28
Data	949	786	892

Table 6.4: Values of fake lepton normalisation factors fitted independently from the differential cross-section measurements.

Norm. factor	Value
$\mathcal{N}_{e,\mathrm{HF}}$	$0.87^{+0.1}_{-0.09}$
$\mathcal{N}_{\mu,\mathrm{HF}}$	$1.00^{+0.09}_{-0.08}$
$\mathcal{N}_{e,\mathrm{other}}$	$1.17^{+0.41}_{-0.36}$

40%. This reflects the fact that there is significantly more F-μ-HF and F-e-HF events across the fake lepton control regions, reducing the statistical uncertainty.

6.3 Signal regions

The signal region selection must strike a balance between selecting sufficient signal events such that the statistical uncertainty of the differential cross-section measurements is minimised, while removing enough background such that the signal regions are of acceptable purity. In both the trilepton and tetralepton channels, a loose preselection is applied before multivariate techniques are used to further separate $t\bar{t}Z$ signal from background processes.

The preselection requires three or four tight leptons, one with $p_T > 27\,\text{GeV}$, in the tetralepton and trilepton regions respectively. Events are required to have at least one OSSF lepton pair with a mass within 10 GeV of the Z-boson mass. In both channels, all possible OSSF pairs are required to have a mass $> 10\,\text{GeV}$ in order to remove low-mass dilepton resonances. At least two or three jets are required in the tetralepton and trilepton regions respectively. At least one jet must pass the 85% efficiency working point of the b-tagging algorithm described in Section 5.3.1. In the tetralepton region, the sum of the lepton charge must be equal to zero. After the preselection, deep neural networks (DNNs) are trained in each region to further separate signal and background.

6.3.1 Tetralepton channel

In the tetralepton channel, events are split into those with a same-flavour (SF) and different-flavour (DF) non-Z lepton pair. The largest background in the tetralepton channel, ZZ+jets, is concentrated in the same-flavour selection, where there are two Z-bosons that each decay to OSSF lepton pairs. The different-flavour events have very high purity after preselection, so further selection did not offer an improvement without reducing the signal acceptance. A binary DNN classification model [122], built using Keras [123], is used to separate $t\bar{t}Z$-4ℓ-SF events from ZZ+jets background. Using truth information from simulated events, the DNN learns the characteristics of $t\bar{t}Z$ and ZZ+jets events. The input variables are the $E_{\text{T}}^{\text{miss}}$, invariant mass of the non-Z leptons, p_T of the reconstructed top-quarks, Z-boson and leptons, the leading and subleading b-tag working point of the jets associated with each event and the 2νSM weight. The output of the DNN is a discriminator that classifies events based on the probability that

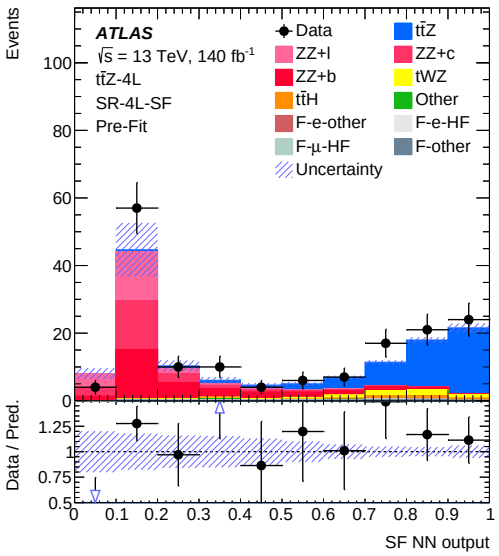

Figure 6.2: Distribution of the classifier output for the same-flavour binary classifier in the tetralepton channel. The coloured histogram shows the SM predictions for the $t\bar{t}Z$ signal and background processes. The black markers show the observed data.

they are a $t\bar{t}Z$ event. Figure 6.2 shows the SF DNN output distribution. The most important discriminating input variables for the DNN are the $E_{\mathrm{T}}^{\mathrm{miss}}$, non-$Z$ dilepton mass and the 2νSM weight.

The DNN-4ℓ-SF performs well, with good separation between $t\bar{t}Z$ and the ZZ+jets background. A SR-4ℓ-SF signal region is defined by requiring DNN-4ℓ-SF output of 0.4 or higher. The DNN output distribution is almost uniform between 0.3 and 0.6, with the large majority of the ZZ+jets background has a DNN output between 0 and 0.5. A control region (CR-4ℓ-ZZ) is defined by requiring DNN-4ℓ-SF output smaller than 0.4 in order to normalise the $ZZ + b$ background to data with a normalisation factor, $\mathcal{N}_{ZZ+b}$, which is fitted simultaneously with the $t\bar{t}Z$ differential cross-sections. The value of 0.4 was chosen as it gave the best precision on the inclusive cross-section. The tetralepton signal region selection is summarised in Table 6.5. The expected and observed event yields in the tetralepton regions are summarised in Table 6.6. The SR-4ℓ-SF region has an expected purity of 69%, with the largest backgrounds being $ZZ + b$ (10%) and tWZ (9%). The SR-4ℓ-DF region has a 77% expected signal purity, with a 10% tWZ contribution and $ZZ + b$ background on the percent-level. The CR-4ℓ-ZZ region is expected to consist of 94% ZZ+jets background, with 33% being $ZZ + b$, and an expected signal purity

Table 6.5: Definition of the tetralepton signal regions.

Variable	**Preselection**		
N_ℓ $(\ell = e, \mu)$	$= 4$		
	≥ 1 OSSF lepton pair with $\mid m_{\ell\ell}^Z - m_Z \mid < 20\,\text{GeV}$		
	for all OSSF combinations: $m_{\text{OSSF}} > 10\,\text{GeV}$		
p_T $(\ell_1, \ell_2, \ell_3, \ell_4)$	$> 27,\ 7,\ 7,\ 7\,\text{GeV}$		
Sum of lepton charge	$= 0$		
N_{jets} $(p_T > 25\,\text{GeV})$	≥ 2		
$N_{b-\text{jets}}$	≥ 1@85%		
	SR-4ℓ-SF	**SR-4ℓ-DF**	**CR-4ℓ-ZZ**
$\ell\ell^{\text{non-Z}}$	e^+e^- or $\mu^+\mu^-$	$e^\pm\mu^\mp$	e^+e^- or $\mu^+\mu^-$
DNN output	≥ 0.4	—	< 0.4

Table 6.6: Observed and expected event yields in the tetralepton signal regions. The indicated errors include MC statistical uncertainty and systematic uncertainties discussed in Chapter 9.

	SR-4ℓ-SF	SR-4ℓ-DF	CR-4ℓ-ZZ
$t\bar{t}Z$	49.4 ± 3.0	51.1 ± 2.9	2.36 ± 0.23
$ZZ + b$	7.5 ± 2.0	0.46 ± 0.12	26.7 ± 6.9
$ZZ + c$	2.13 ± 0.66	0.30 ± 0.09	24.6 ± 7.1
$ZZ + l$	0.83 ± 0.24	0.34 ± 0.09	22.6 ± 5.2
tWZ	6.60 ± 0.82	7.3 ± 1.2	0.69 ± 0.10
$t\bar{t}H$	2.79 ± 0.24	2.82 ± 0.24	0.32 ± 0.04
Other	0.55 ± 0.25	1.12 ± 0.52	0.55 ± 0.25
F-e-HF	0.28 ± 0.07	0.45 ± 0.10	0.11 ± 0.03
F-e-other	0.39 ± 0.14	0.50 ± 0.18	0.10 ± 0.04
F-μ-HF	0.58 ± 0.07	0.62 ± 0.08	0.16 ± 0.02
F-other	0.90 ± 0.40	1.66 ± 0.74	0.33 ± 0.15
Total	72.0 ± 3.4	66.7 ± 3.0	78.5 ± 8.0
Data	79	74	81

of 3%. Data in the SR-4ℓ-SF, SR-4ℓ-DF and CR-4ℓ-ZZ regions are consistent with the expected event yields. Studies performed on the inclusion of the CR-4ℓ-ZZ in the 4ℓ measurements showed that it improved the precision by $\sim 8\%$ in each bin and provided better constraining power of the $ZZ + b$ background.

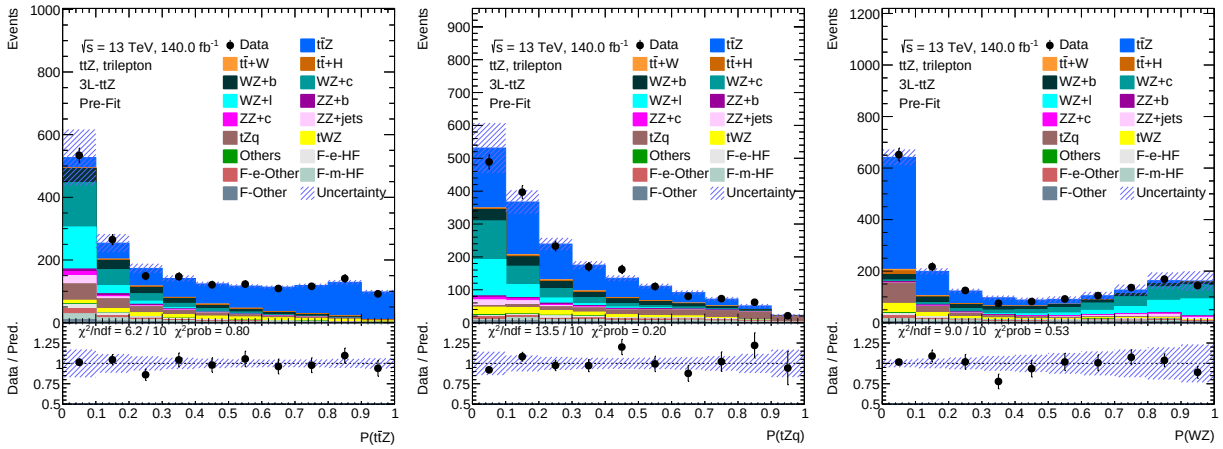

(a) DNN-$t\bar{t}Z$ **(b)** DNN-tZq **(c)** DNN-WZ

Figure 6.3: Distribution of the classifier outputs for the three classification nodes of the multi-class classifier DNN in the trilepton channel. The coloured histogram shows the SM predictions of the $t\bar{t}Z$ signal and background processes. The black markers show the observed data.

6.3.2 Trilepton channel

In the trilepton channel, a multiclass DNN was used to separate the two main background processes in the trilepton channel from $t\bar{t}Z$ signal. This method is similar to the DNN used in the tetralepton channel, but utilises three classification nodes: one for each of the $t\bar{t}Z$, tZq and WZ categories. The input variables include the kinematic information such as jet and lepton p_T, $E_{\mathrm{T}}^{\mathrm{miss}}$, jet multiplicity ($N_{\mathrm{jets}}$), the sum of the transverse momenta of the leptons, reconstructed masses of the top-quarks and the leading and subleading b-tagging working point of the jets associated with each event. The trilepton DNN produces an output for each classifier node, which are shown in Figure 6.3. The most important discriminating input variables were jet p_T for the $t\bar{t}Z$ classifier, the leading jet b-tagging working point for the WZ classifier, and the mass of the hadronically-reconstructed top-quark for the tZq classifier.

The data are seen to be in good agreement with the predicted DNN output distributions. The higher the value of the classifier output, the more events are $t\bar{t}Z$, tZq or WZ-like for each classification node. From Figure 6.3, we can see that the tZq process (shown in brown) cannot be completely separated from $t\bar{t}Z$ (shown in blue). Therefore, it is difficult to normalise this process in data and instead the tZq background is kept fixed to the SM prediction and

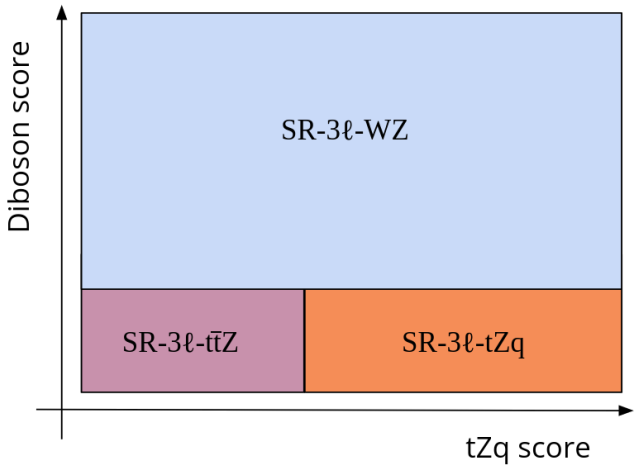

Figure 6.4: Visual representation of the trilepton signal regions defined by the selection on the DNN WZ (diboson) and tZq classifier outputs.

assigned a normalisation uncertainty. On the other hand, Figure 6.3c shows that the WZ+jets background (shown in shades of turquoise) can be separated from signal using the DNN-WZ output.

Selection requirements on the DNN-WZ and DNN-tZq are used to define three orthogonal trilepton signal regions: the SR-3ℓ-$t\bar{t}Z$ region requires DNN-tZq output of less than 0.4 and a DNN-WZ output of less than 0.22. A SR-3ℓ-tZq region is defined that requires DNN-tZq output of 0.4 or higher and DNN-WZ output of less than 0.22. A third region, SR-3ℓ-WZ, requires a DNN-WZ output of 0.22 or higher and a b-tagged jet at the 60% working point to enrich the $WZ + b$ component. Then, the $WZ + b$ background can be normalised to data in the SR-3ℓ-WZ region using a normalisation factor, $\mathcal{N}_{WZ+b}$, in the differential cross-section fit. The trilepton signal region selection is summarised in Table 6.7 and visualised in Figure 6.4. The previous ATLAS measurement used a single $t\bar{t}Z$-enriched signal region in the trilepton channel. By including regions that are enriched in the tZq and WZ+jets backgrounds but also contain $t\bar{t}Z$ events, we can select more signal events and increase the precision of the differential cross-section measurements. The expected and observed event yields in the trilepton regions are summarised in Table 6.8. The SR-3ℓ-$t\bar{t}Z$ has an expected purity of 76%, with the largest backgrounds being tWZ (7%), $WZ + b$ (4%) and tZq (4%). The SR-3ℓ-WZ regions has 27% expected signal purity and a 30% expected contribution from the $WZ + b$ background.

Table 6.7: Definition of the trilepton signal regions.

Variable	**Preselection**		
N_ℓ $(\ell = e, \mu)$	$= 3$		
	≥ 1 OSSF lepton pair with $\mid m_{\ell\ell}^Z - m_Z \mid < 10$ GeV		
	for all OSSF combinations: $m_{\text{OSSF}} > 10$ GeV		
$p_T\,(\ell_1, \ell_2, \ell_3)$	$> 27,\ 20,\ 15$ GeV		
$N_{\text{jets}}\,(p_T > 25$ GeV)	≥ 3		
$N_{b-\text{jets}}$	≥ 1@85%		
	SR-3ℓ-ttZ	**SR-3ℓ-tZq**	**SR-3ℓ-WZ**
DNN-tZq output	< 0.40	≥ 0.40	—
DNN-WZ output	< 0.22	< 0.22	≥ 0.22
$N_{b-\text{jets}}$	—	—	≥ 1@60%

The SR-3ℓ-tZq region has an expected signal purity of 38% and a 25% contribution from tZq background. In each of the trilepton signal regions, the data are in good agreement with the expected event yields.

6.3.3 Particle- and parton-level definitions

The particle- and parton-level selections for the tetralepton and trilepton channels used for the differential cross-section measurements are summarised in Table 6.9. The particle-level fiducial volumes are constructed to closely follow the detector-level regions, with at least one OSSF lepton pair within 10 GeV of the mass of the Z-boson. Particle-level jets are reconstructed in the same way as detector-level jets, with the anti-k_t algorithm and $\Delta R = 0.4$. Particle-level jets are considered b-jets if they are ghost-matched to a b-hadron [124]. The parton-level fiducial volumes are defined by the top-quark decays; semi-leptonic (e or μ + jets only) in the trilepton channel, and dileptonic ($e^+e^-, e^\pm\mu^\mp, \mu^+\mu^-$ only) in the tetralepton channel. The Z-boson is required to decay to two charged leptons ($Z \to e^+e^-, \mu^+\mu^-$). Events featuring tau leptons which originate directly from either the Z- or W-bosons from the $t\bar{t}$ system are removed from the parton-level fiducial volume and are not considered in the cross-section measurement, regardless of their subsequent decay. The differential observables, described in Section 7.2, are

Table 6.8: Observed and expected event yields in the trilepton signal regions. The indicated errors include MC statistical uncertainty and systematic uncertainties discussed in Chapter 9.

	SR-3ℓ-$t\bar{t}Z$	SR-3ℓ-WZ	SR-3ℓ-tZq
$t\bar{t}Z$	441 ± 21	49.0 ± 3.7	151 ± 11
$WZ + b$	21.1 ± 7.4	47 ± 16	27.1 ± 9.5
$WZ + c$	8.9 ± 3.6	12.2 ± 5.0	11.1 ± 4.6
$WZ + l$	1.19 ± 0.52	1.70 ± 0.76	1.81 ± 0.80
$ZZ + b$	4.3 ± 2.5	6.9 ± 4.0	7.3 ± 4.2
$ZZ + c$	1.23 ± 0.42	1.22 ± 0.43	1.61 ± 0.53
$ZZ + l$	0.42 ± 0.13	0.26 ± 0.09	0.53 ± 0.15
tZq	20.8 ± 4.0	13.2 ± 2.3	99 ± 16
tWZ	40.0 ± 7.6	18.0 ± 4.2	24.2 ± 3.0
$t\bar{t}W$	4.3 ± 2.2	2.2 ± 1.1	5.3 ± 2.6
$t\bar{t}H$	11.9 ± 1.1	1.43 ± 0.13	6.70 ± 0.57
$t\bar{t}t\bar{t}$	1.56 ± 0.78	0.13 ± 0.07	0.27 ± 0.14
Other	1.33 ± 0.61	1.40 ± 0.63	0.39 ± 0.19
F-e-HF	4.6 ± 1.0	3.90 ± 0.87	12.0 ± 2.6
F-e-Other	7.8 ± 2.7	7.3 ± 2.6	15.2 ± 5.4
F-μ-HF	6.98 ± 0.86	5.27 ± 0.66	18.2 ± 2.2
F-Other	2.8 ± 1.2	2.7 ± 1.2	4.4 ± 2.0
Total	580 ± 19	174 ± 13	386 ± 15
Data	569	175	388

reconstructed from the top-quarks after final-state radiation and immediately prior to their decay. The invariant mass of the two leptons from the Z-boson decay is required to be within 15 GeV of the mass of the Z-boson.

Table 6.9: Definition of the fiducial volumes for the trilepton and tetralepton channels at particle- and parton-level.

	Variable	3ℓ	4ℓ
Particle-level	N_ℓ $(\ell = e, \mu)$	$=3$	$=4$
	p_T (ℓ)	$> 27, 20, 15\,\text{GeV}$	$> 27, 7, 7, 7\,\text{GeV}$
	Sum of lepton charge	± 1	$= 0$
	N_{jets} $(p_T > 25\,\text{GeV})$	≥ 3	≥ 2
	$N_{b-\text{jets}}$	≥ 1	
	Non-Z leptons	OSSF with $\lvert m_{\ell\ell} - m_Z \rvert < 10\,\text{GeV}$	
Parton-level	$t\bar{t} \rightarrow$	$e^\pm/\mu^\pm$ + jets	$e^\pm\mu^\mp/e^\pm e^\mp/\mu^\pm\mu^\mp$
	$Z \rightarrow$	$e^\pm e^\mp/\mu^\pm\mu^\mp$	
		$\lvert m_{\ell\ell} - m_Z \rvert < 15\,\text{GeV}$	

Chapter 7

Unfolding and differential observables

The aim of this research is to measure the differential cross-sections of $t\bar{t}Z$ with respect to a set of kinematic variables. In an ideal world, we would be able to perfectly measure the value of these observables for every $t\bar{t}Z$ event that is produced from LHC pp collisions, obtaining the true distribution of the observable. In reality, we have detectors such as ATLAS that have both finite resolution, which can change the shape of the measured observable distribution, and limited acceptance, meaning the detector is likely to miss some events. The true observable distribution, where we measure the differential cross-section, can be obtained with a method called *unfolding*, which aims to correct for these detector effects.

New theoretical models may only be directly compared to ATLAS data if they include the effect of the detector, which involves passing the calculations through the CPU-expensive detector simulation that is used in the last step of event simulation. This considerably slows down the comparison of theory and experimental measurements. In order to avoid this, we can use unfolding to produce cross-section measurements at particle- or parton-level and then compare to theory predictions. Unfolding also makes results from similar experiments, such as ATLAS and CMS, directly comparable. Lastly, producing unfolded differential cross-section results allows for their reinterpretation in the future. There are many approaches to unfolding; in this analysis we use profile likelihood unfolding (PLU) which employs the profile likelihood ratio

test statistic [125]. The following sections describe the statistical framework of the unfolding method, the fit parameters and the choice of the differential observables and their binning.

7.1 Profile likelihood unfolding

Likelihood functions can be used to fit a cross-section from data. The likelihood, L, gives the probability of observed data, n, for given values of expected model parameters, x, like $L = p(n|x)$. By maximising the likelihood, model parameters, such as a cross-section parameter, are extracted that best describe the data. For a cross-section measurement, a key model parameter is the expected number of events. Assuming two types of events, signal and background, the expected number of events, v, is equal to

$$v = \mu s + b, \tag{7.1}$$

where s is the number of predicted signal events, b is the number of predicted background events and μ is the signal strength in observed data. Here, the signal strength is the total observed number of signal events divided by the total number of signal events predicted by the SM, such that $\sigma_{\text{measured}} = \mu\sigma_{\text{SM}}$. A signal strength value of $\mu = 0$ is equivalent to the background-only hypothesis and $\mu = 1$ indicates that the data is in perfect agreement with the SM. In this case, the signal strength is essentially the result of an inclusive cross-section measurement.

The likelihood is a function of *parameters of interest* (POIs), which here refer to the signal strength μ, and nuisance parameters (NPs), $\vec{\theta}$ [125]. NPs correspond to the systematic uncertainties associated with the model parameters: they account for uncertainty arising from experimental procedures, theoretical calculations and the effect of limited MC statistics. They can be constrained directly in the likelihood via multiplicative Gaussian terms. The number of expected signal and background events depend on the NPs. In a simple inclusive cross-section measurement observing n events, the likelihood can be defined as

$$L\left(n|\nu\right) = L\left(n|\mu,\vec{\theta}\right) = \text{Pois}\left(n|\nu(\mu,\vec{\theta})\right) \times \prod_{j}^{\text{NPs}} \text{Gaus}\left(\theta_j\right). \tag{7.2}$$

Background normalisation factors are a type of NP used to estimate the $ZZ + b$, $WZ + b$ and fake lepton background processes described in Chapter 6.2. This requires additional degrees of freedom in the fit, introduced by using multiple orthogonal regions, including control regions that are enriched in the backgrounds we wish to constrain. The background normalisation factors, $\vec{k}$, are included in the likelihood function, fitting to data to avoid relying on the absolute prediction from simulated events. These are essentially nuisance parameters with no prior constraints. The likelihood function for a single POI fitted in multiple orthogonal analysis regions may be written as the product of Poisson probabilities over regions, R:

$$L\left(\vec{n}|\mu,\vec{\theta},\vec{k}\right) = \prod_{r}^{R} \text{Pois}\left(n_r|\nu_r(\mu,\vec{\theta},\vec{k})\right) \times \prod_{j}^{\text{NPs}} \text{Gaus}\left(\theta_j\right). \tag{7.3}$$

Where an inclusive cross-section measurement has one signal strength parameter, a differential cross-section is the measurement of a set of signal strengths, $\vec{\mu}$, one for each bin i of the differential observable. For a binned distribution, the likelihood function also includes the product of Poisson probabilities over all bins, N, of a distribution:

$$L\left(\vec{n}|\vec{\mu},\vec{\theta},\vec{k}\right) = \prod_{r}^{R}\prod_{i}^{N} \text{Pois}\left(n_{i,r}|\nu_{i,r}(\vec{\mu},\vec{\theta},\vec{k})\right) \times \prod_{j}^{\text{NPs}} \text{Gaus}\left(\theta_j\right). \tag{7.4}$$

Then, the expected number of events in bin i is

$$\nu_i = s_i(\vec{\mu},\vec{\theta}) + b_i(\vec{\theta},\vec{k}), \tag{7.5}$$

where the expected number of signal events now depends on the signal strength parameters in every other bin. In this case, the calculation of the expected signal events requires some careful consideration. Due to finite detector resolution, an event contributing to cross-section in bin i could actually be reconstructed in bin $i+1$. Due to detector inefficiencies, the expected number of signal events recorded by the detector is smaller than those produced from collisions. These effects are accounted for with a migration matrix and efficiency and acceptance corrections, collectively referred to as *unfolding corrections*. The expected signal events in bin i are inferred

from the unfolding corrections such that

$$s_i = \sum_j \frac{1}{\alpha_i} M_{ij} \epsilon_j \mu_j \tau_j \tag{7.6}$$

where τ_j is the number of signal events in the truth distribution in bin j, M_{ij} is the migration matrix and α_i and ϵ_j are the acceptance and efficiency histograms, respectively. The acceptance histogram adjusts the observable distribution at particle-level for events that pass detector-level requirements, but do not pass fiducial requirements:

$$\alpha_i = \frac{n_i^{\text{reco}} \cap n_i^{\text{truth}}}{n_i^{\text{reco}}}, \tag{7.7}$$

i.e. events that are incorrectly accepted at detector-level due to finite detector resolution. The efficiency histogram corrects for events which passed particle-level selection but not detector-level selection:

$$\epsilon_j = \frac{n_j^{\text{reco}} \cap n_j^{\text{truth}}}{n_j^{\text{truth}}}, \tag{7.8}$$

i.e. events that are missed at detector-level due to reconstruction software and hardware inefficiencies. The migration matrix contains the probability that an event reconstructed in bin j will migrate to truth-level bin i due to finite detector resolution. In the case that there are strong correlations between bins of a distribution, leading to a non-diagonal migration matrix, unfolding can amplify statistical fluctuations. In order to "smooth" the unfolded distribution, an additional term can be used in the likelihood that introduces a penalty for large fluctuations between bins; this is called *regularisation*.

Rather than explicitly maximising the likelihood function, it is convenient to instead minimise the negative log-likelihood numerically. The fit is implemented using the `TRExFitter` framework [126] which employs `Minuit` numerical minimisation algorithms [127]. The uncertainty associated with a fitted POI is found as the difference between the POI central value and the POI value when the difference in the corresponding negative log-likelihoods is equal to one. Then, the statistical uncertainty corresponds to the uncertainty of the fitted POI when no nuisance parameters are included. This framework can easily perform fits in an identical setup for the

normalised differential cross-section. The normalised cross-section can be calculated using a POI for the total cross-section. This requires the removal of one degree of freedom, usually the signal strength parameter in the last bin of the distribution, in order to fulfil the criterion $\int \frac{d\sigma}{dx} = \sigma$. The remaining signal strength parameters are redefined in terms of the total signal strength.

Profile likelihood unfolding is chosen over another popular unfolding method, iterative Bayesian unfolding [128], for a number of reasons. The formalism of the likelihood allows for the trivial inclusion of a number of different analysis regions, which, along with the free-floating background normalisation factors, can be used to fit backgrounds simultaneously with the signal. This also makes it straightforward to fit two analysis channels, such as the trilepton and tetralepton, simultaneously. The inclusion of nuisance parameters in the likelihood allows for the potential exploitation of their correlations. From a technical point of view, the same statistical framework can be applied neatly to a set of multiple observables, without the need to optimise a number of iterations for each observable. Lastly, it is convenient to use the same likelihood approach as the corresponding inclusive cross-section measurement which was published in the same paper [1].

Pruning nuisance parameters

A large number of nuisance parameters can lead to the problem of dimensionality, where the unfolding fit can be slow or struggle to converge. This can be especially true for nuisance parameters with a low impact on the fit which can lead to flat areas in parameter space. Therefore, it is useful to *prune* low-impact nuisance parameters from the fit. For a given sample and region, the impact of the nuisance parameter is removed if the impact on the normalisation from a particular nuisance parameter is less than 0.01%.

Goodness-of-fit

A *goodness-of-fit* test is used to quantify how well a fit model describes observed data. For the maximum-likelihood fits described in this chapter, it is appropriate to construct a goodness-of-fit test that compares the likelihood values of two models. Here, we compare the nominal fit

likelihood value to the *saturated model* [129]. The saturated model is that which has one free parameter for each bin in each region of the data, such that it describes the data perfectly. The saturated model does not depend on the original model parameters. According to Wilks theorem, the ratio of two likelihoods follow the χ^2 distribution asymptotically. By calculating the difference between the minimised negative log-likelihoods of the saturated model and the original model, a goodness-of-fit value is produced that can be interpreted like a χ^2 test via its p-value. The p-value is the probability of getting a χ^2 value that is equal-to or larger-than that of a given model, obtained by integrating the corresponding range of the χ^2 distribution.

Ranking nuisance parameters

It is useful to know how nuisance parameters affect the differential cross-section measurements, and especially so to find the nuisance parameters with the largest impact. The impact is evaluated as the difference in the value of the POI between the nominal fit and a second fit where the value of the nuisance parameter is fixed ($\Delta\mu$). For a nuisance parameter θ, the fixed value, $\hat{\theta}$, is equal to the post-fit (maximum-likelihood) value. The impact can be evaluated before and after the fit such that we define the

- *pre-fit impact*: where θ is set to $\hat{\theta} \pm \Delta\theta$, which describes the uncertainty of θ with a prior unit Gaussian constraint.
- *post-fit impact*: where θ is set to $\hat{\theta} \pm \Delta\hat{\theta}$ and $\Delta\hat{\theta}$ is the uncertainty associated with $\hat{\theta}$ in the nominal fit.

The same procedure can be applied to the normalisation factors $\vec{k}$ for the post-fit impact only. The larger the impact of a particular nuisance parameter, the larger the contribution to the total uncertainty of the measured POI. If the pre-fit impact is different to the post-fit impact, this implies that the fit is able to constrain the nuisance parameter. A ranking of the impact of the nuisance parameters is performed for each POI in the fit.

Table 7.1: Summary of the observables used to measure the $t\bar{t}Z$ differential cross-sections in the tetralepton channel and the combination of the trilepton and tetralepton channels.

	Observable	Definition
4ℓ	N_{jets}	Number of selected jets with $p_T > 25\,\text{GeV}$ and $\lvert\eta\rvert < 2.5$
	H_{T}^{ℓ}	Sum of the transverse momenta of all the signal leptons
	$\lvert\Delta\phi(\ell,\ell)\rvert$	Absolute azimuthal separation between the two leptons from the $t\bar{t}$ system
$3\ell+4\ell$	p_{T}^{Z}	Transverse momentum of the Z-boson
	$\lvert y^{Z}\rvert$	Absolute rapidity of the Z-boson
	$\cos(\theta_{Z}^{\star})$	Angle between the direction of the Z-boson in the detector reference frame and the direction of the negatively charged lepton in the rest frame of the Z-boson

7.2 Differential observables

The goal of this analysis is to measure the differential cross-section of $t\bar{t}Z$ with respect to a set of kinematic observables. The choice of observables is motivated by potential sensitivity to new physics and fundamental properties of the $t\bar{t}Z$ final state. The measurements are made in the tetralepton channel, as well as with combination of the trilepton and tetralepton channels. The chosen differential observables are kinematic and angular properties of the top-quarks, Z-boson and the $t\bar{t}Z$ system. The observables that can be reconstructed in both channels are unfolded in the combination of the trilepton and tetralepton regions. All of the observables are unfolded to both particle- and parton-level, except for the N_{jets} observable, which is unfolded only to particle-level as jets are undefined at parton-level. The list of the observables used to measure the $t\bar{t}Z$ differential cross-sections reported in this analysis is shown in Table 7.1. Additional observables, that rely on the hadronic reconstruction of the top-quark, are found to have somewhat non-diagonal migration matrices: 40% to 70% on diagonal, compared to purely leptonic observables with more than 90% on the diagonal. These observables, in the combination of the trilepton and tetralepton channels, are unfolded using regularised unfolding and the results are reported in Ref. [1], alongside observables unfolded in the trilepton channel only.

7.2.1 Binning optimisation

In differential cross-section measurements, the binning of the differential observables can have a large impact on the measurement precision, requiring a level of optimisation. Ideally, narrow binning would be used in order to maximise sensitivity to the distribution shape and potential new physics effects. However, $t\bar{t}Z$ is a low-statistics process and narrow binning risks leaving some bins without sufficient MC statistics to estimate the expected signal and background or the effects of systematic uncertainties. Binnings that are too narrow also lead to highly-correlated bins and an unstable fit. We aim for a balance between fit sensitivity and stability. For each observable, a number of different distribution binnings are tested. The optimal binning for each observable was chosen according to a set of predetermined criteria. Since profile likelihood unfolding is CPU-intensive, it is not feasible to optimise the binning using this unfolding method. As a quicker alternative, iterative Bayesian unfolding [128] is used. The binning is optimised according to two requirements. Firstly, the statistical uncertainty in all unfolded bins must be lower than 35% for variables unfolded in the tetralepton channel only and 25% for the combination of the trilepton and tetralepton channels. Secondly, the diagonal elements of the migration matrix must be higher than a chosen threshold. The high edge of the first bin of the distribution is chosen at the lowest possible value where these two requirements are satisfied. The range of each bin is found sequentially. The threshold on the minimal value of migration matrix diagonal elements is gradually decreased to obtain binning for a higher number of bins. The binning is optimised for a number of bins ranging from 2 to 10. The binning with the highest number of bins resulting in uncertainties below the chosen threshold and passing all the validation tests, discussed in Section 8, when unfolded with the profile likelihood method, is then chosen as the optimal binning for each observable. The same binning is used for both particle- and parton-level. The binning of each of the differential observables is shown in Table 7.2.

7.2.2 Detector-level distributions and unfolding corrections

The N_{jets}, $|\Delta\phi(\ell,\ell)|$ and H_{T}^{ℓ} observable distributions at detector-level are shown in Figures 7.1 to 7.3 for the tetralepton signal and control regions. The coloured histograms show the

Table 7.2: Bin ranges for the differential observables defined in Table 7.1. The bin ranges are identical for particle- and parton-level measurements.

Observable	Channels	Bins	Bin ranges
N_{jets}	4ℓ	3	[1.5,2.5,3.5,8.5]
$\lvert\Delta\phi(\ell,\ell)\rvert$	4ℓ	7	[0, 0.2, 0.37, 0.53, 0.67, 0.79, 0.89, 1]
H_{T}^{ℓ} [GeV]	4ℓ	5	[50, 195, 250, 315, 400, 800]
p_{T}^{Z} [GeV]	$3\ell + 4\ell$	8	[0, 60, 100, 140, 180, 230, 280, 350, 1000]
$\lvert y^{Z}\rvert$	$3\ell + 4\ell$	9	[0, 0.125, 0.275, 0.425, 0.6, 0.775, 0.95, 1.175, 1.45, 2.5]
$\cos\theta_{Z}^{*}$	$3\ell + 4\ell$	8	[-1, -0.75, -0.5, -0.25, 0, 0.25, 0.5, 0.75, 1]

expected number of $t\bar{t}Z$ signal events in blue, as well as the expected background events. The observed data are shown as black markers in each bin. Across all of the tetralepton observable distributions, there is a high signal purity in the SR-4ℓ-SF and SR-4ℓ-DF regions, which reflects the event yields shown in Table 6.6. There are more ZZ+jets background events, shown in shades of red, in the SR-4ℓ-SF region than the SR-4ℓ-DF region, as expected. In the SR-4ℓ-SF and SR-4ℓ-DF regions there is a fairly uniform tWZ background, showing that it is difficult to distinguish from $t\bar{t}Z$ signal. Comparing the CR-4ℓ-ZZ and SR-4ℓ-SF regions for each of the observables, the shape of the $ZZ + b$ background is consistent in both regions. This is important because the normalisation of this background is fitted to data, but the shape relies on the MC predictions. Generally, there is good agreement between the data and expected events. The largest discrepancy is seen in the third bin of the H_{T}^{ℓ} distribution (Figure 7.3) in the SR-4ℓ-DF and SR-4ℓ-SF regions, where the data are significantly higher than the expected events. As this is not seen in the CR-4ℓ-ZZ region, this could be a statistical fluctuation in the data or signal mis-modelling. This distribution is used to validate that the unfolding method is robust against data-MC differences (Section 8.3.2), and it is not thought to have a large impact on the differential cross-section measurements. The p_{T}^{Z}, $\lvert y^{Z}\rvert$ and $\cos(\theta_{Z}^{\star})$ observable distributions at detector-level are shown in Figures 7.4 to 7.6 in the trilepton and tetralepton signal and control regions. Across all of the observable distributions, the shape of both the $WZ + b$ and tZq backgrounds looks consistent between the SR-3ℓ-WZ and SR-3ℓ-tZq regions and the SR-3ℓ-$t\bar{t}Z$ region. In the trilepton regions, the tZq and tWZ backgrounds prove difficult to separate from $t\bar{t}Z$ for these observables.

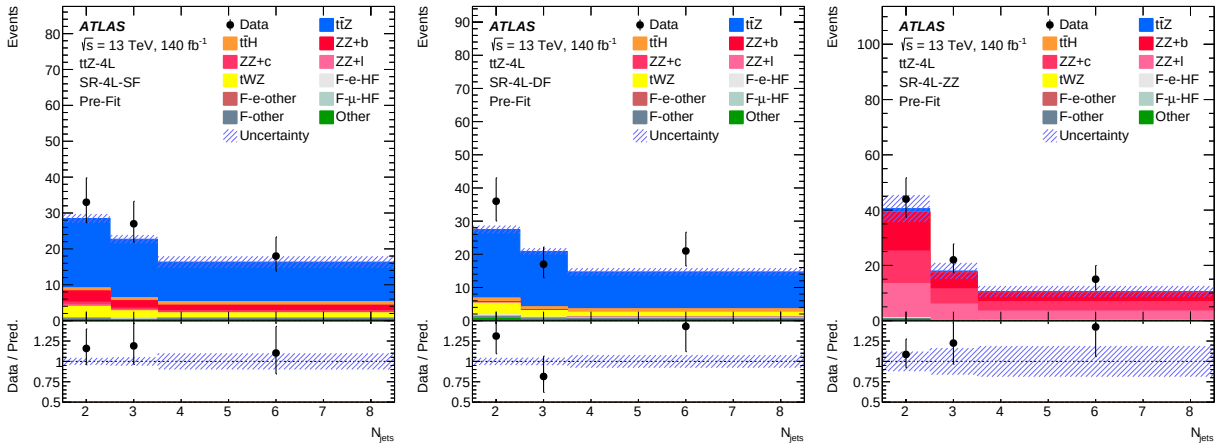

(a) SR-4ℓ-SF **(b)** SR-4ℓ-DF **(c)** CR-4ℓ-ZZ

Figure 7.1: Detector-level distributions of N_{jets} in the tetralepton regions.

The unfolding corrections for the differential observables used to measure the cross-section in the tetralepton channel are shown in Figures 7.7 to 7.16. The unfolding corrections for the differential observables used to measure the cross-section in the combination of the trilepton and tetralepton channels are shown in Figures 7.17 to 7.27. The efficiency values are generally low across all regions due to reconstruction inefficiencies such as the b-tagging and lepton reconstruction. The highest efficiency is seen in the SR-3ℓ-$t\bar{t}Z$, which is expected as this region contains the most $t\bar{t}Z$ events. In all plots, the uncertainty is largest for the CR-4ℓ-ZZ region, which has the lowest signal statistics. The acceptance values are generally high due to the similar

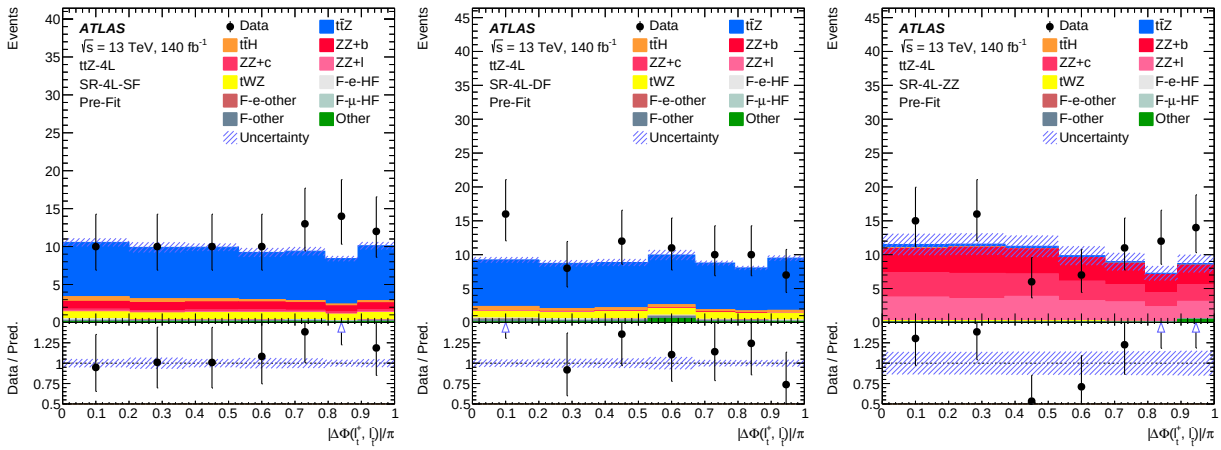

(a) SR-4ℓ-SF **(b)** SR-4ℓ-DF **(c)** CR-4ℓ-ZZ

Figure 7.2: Detector-level distributions of $|\Delta\phi(\ell,\ell)|$ in the tetralepton regions.

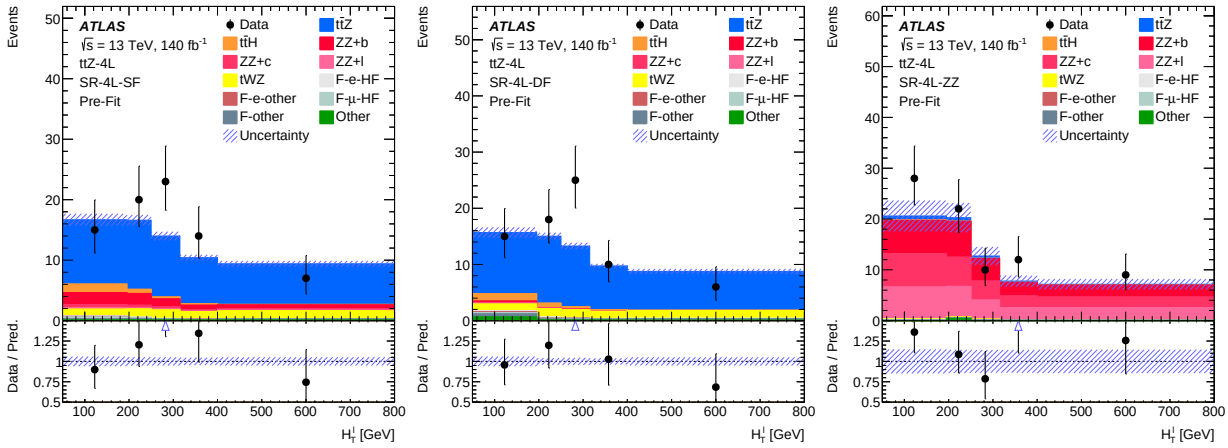

(a) SR-4ℓ-SF **(b)** SR-4ℓ-DF **(c)** CR-4ℓ-ZZ

Figure 7.3: Detector-level distributions of H_{T}^{ℓ} in the tetralepton regions.

selection used for truth- and detector-level. There are some interesting shape effects in the trilepton region efficiency where the multiclass DNN is used to define the regions. Figures 7.17a and 7.19a show that the efficiency of the SR-3ℓ-$t\bar{t}Z$ region selection increases with p_{T}^{Z}, the efficiency of the SR-3ℓ-tZq region selection decreases. We can interpret this as the DNN outputs having sensitivity to this observable, with events that have low p_{T}^{Z} more likely to be classified as 'tZq-like'. Importantly, signal events in the SR-3ℓ-tZq region are included in the cross-section measurements, which wouldn't be the case in a cut-based analysis such as the previous ATLAS measurements [25]. Generally, the migration matrices are highly diagonal, as required by the binning optimisation process. The least diagonal matrices are in the regions where there are fewest signal events, such as CR-4ℓ-ZZ. This region also has significantly lower acceptance than other regions because there are very few signal events contained in the region.

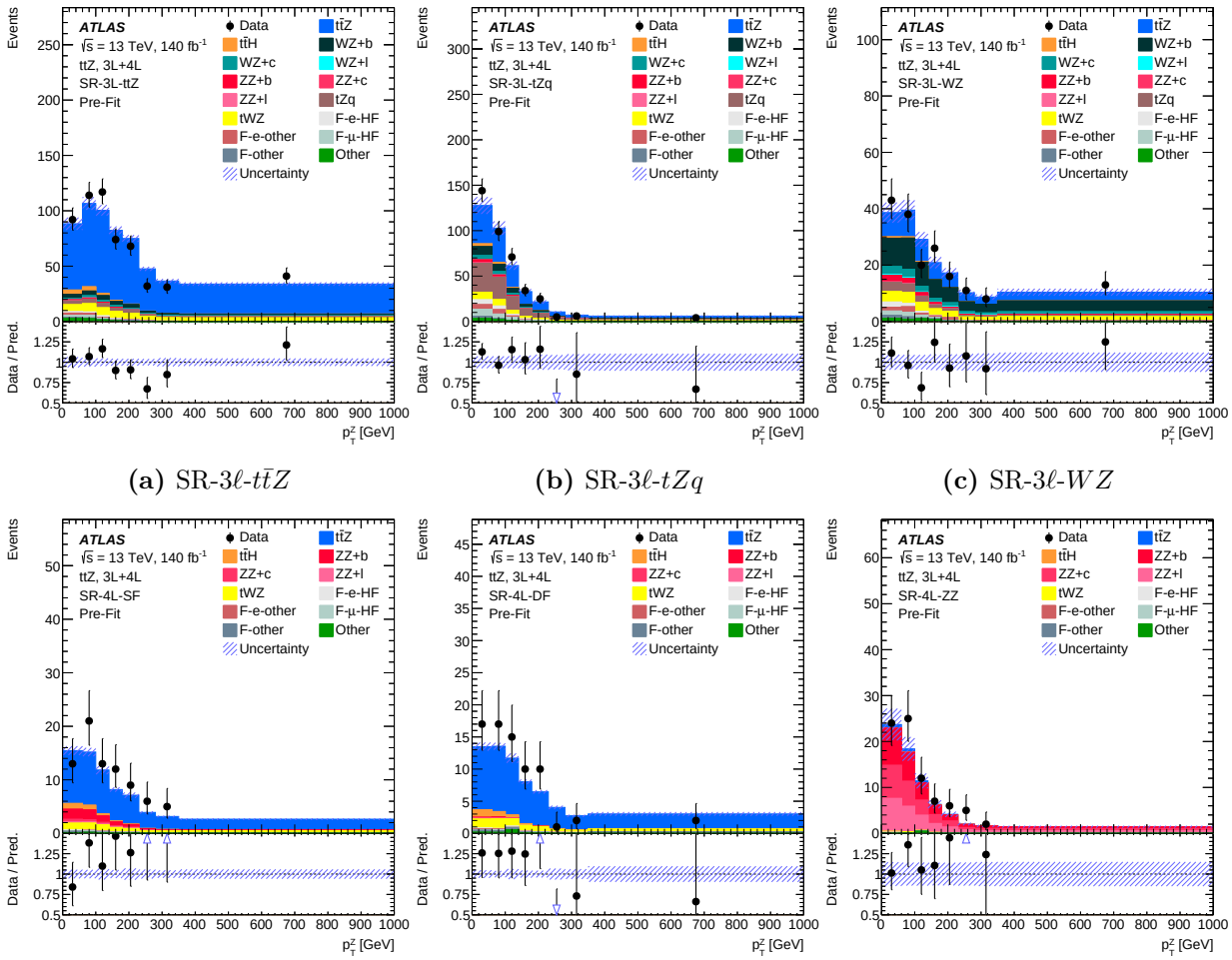

(a) SR-3ℓ-$t\bar{t}Z$ (b) SR-3ℓ-tZq (c) SR-3ℓ-WZ

(d) SR-4ℓ-SF (e) SR-4ℓ-DF (f) CR-4ℓ-ZZ

Figure 7.4: Detector-level distributions of p_{T}^{Z} in the trilepton and tetralepton regions.

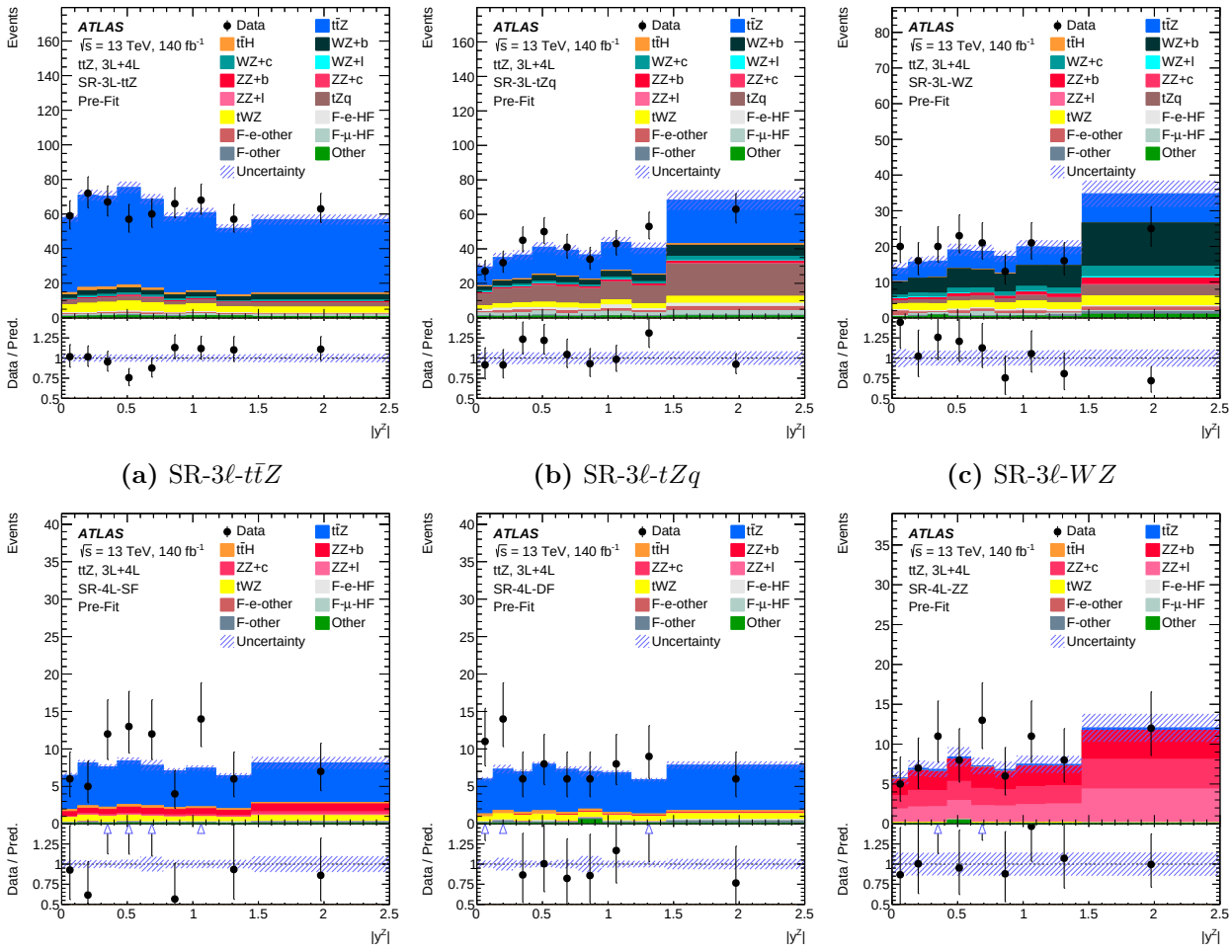

(a) SR-3ℓ-$t\bar{t}Z$ **(b)** SR-3ℓ-tZq **(c)** SR-3ℓ-WZ

(d) SR-4ℓ-SF **(e)** SR-4ℓ-DF **(f)** CR-4ℓ-ZZ

Figure 7.5: Detector-level distributions of $|y^Z|$ in the trilepton and tetralepton regions.

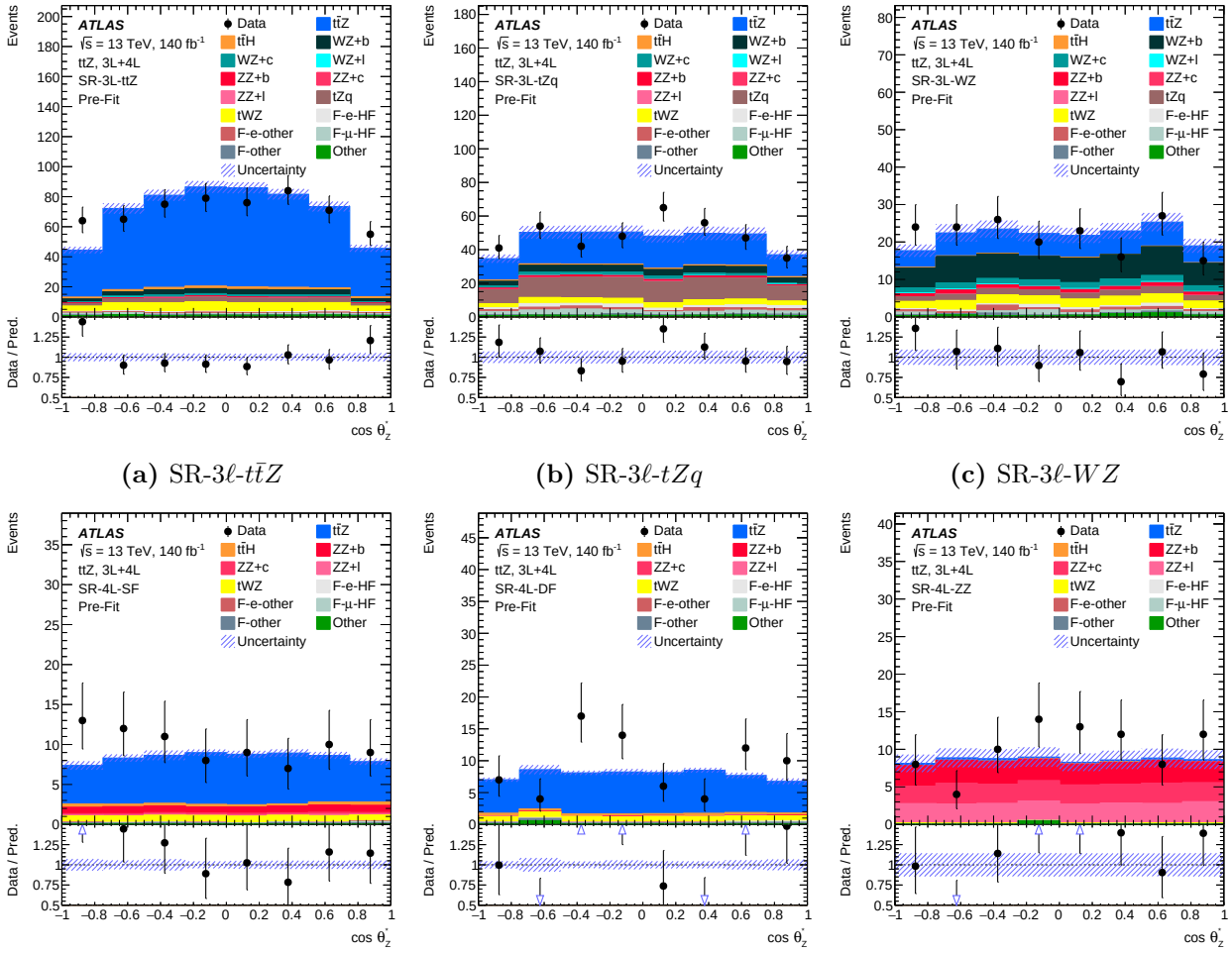

(a) SR-3ℓ-$t\bar{t}Z$ **(b)** SR-3ℓ-tZq **(c)** SR-3ℓ-WZ

(d) SR-4ℓ-SF **(e)** SR-4ℓ-DF **(f)** CR-4ℓ-ZZ

Figure 7.6: Detector-level distributions of $\cos(\theta^{\star}_{Z})$ in the trilepton and tetralepton regions.

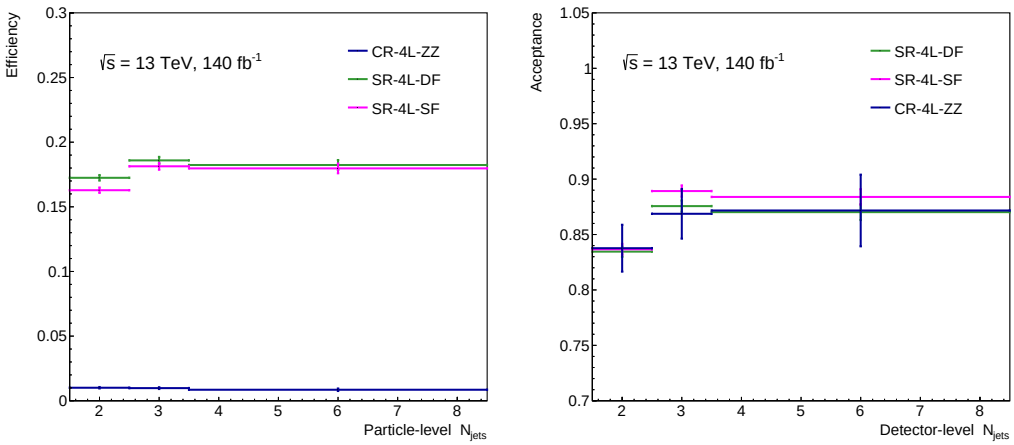

Figure 7.7: Efficiency (left) and acceptance (right) corrections to particle-level for N_{jets} in the tetralepton regions.

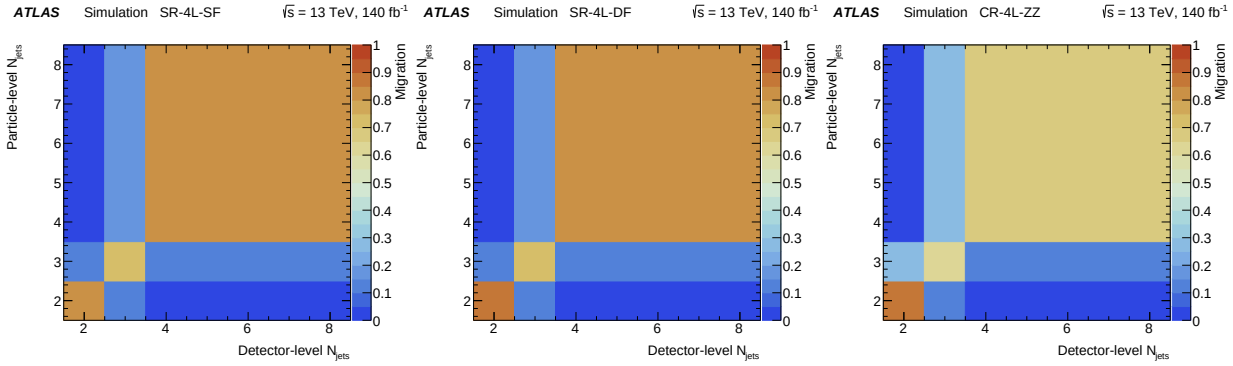

(a) SR-4ℓ-SF **(b)** SR-4ℓ-DF **(c)** CR-4ℓ-ZZ

Figure 7.8: Migration matrices with respect to particle-level N_{jets} in the tetralepton regions.

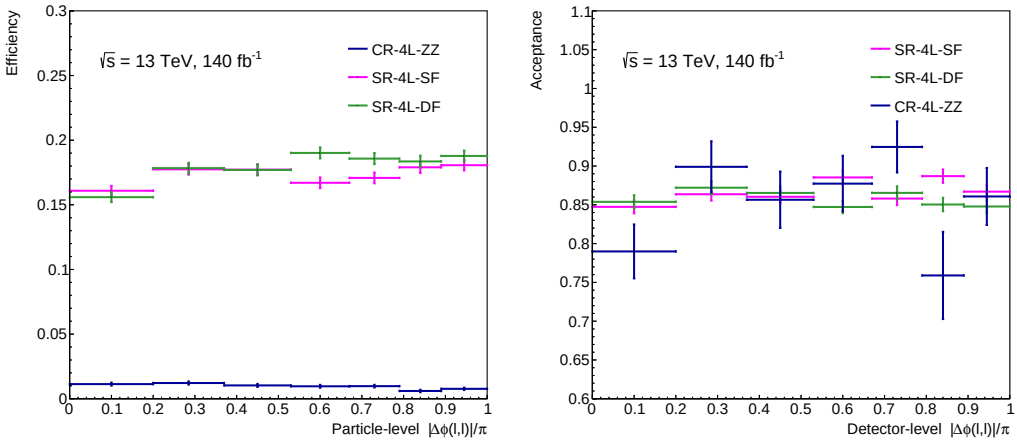

Figure 7.9: Efficiency (left) and acceptance (right) corrections to particle-level $|\Delta\phi(\ell,\ell)|$ for the tetralepton regions.

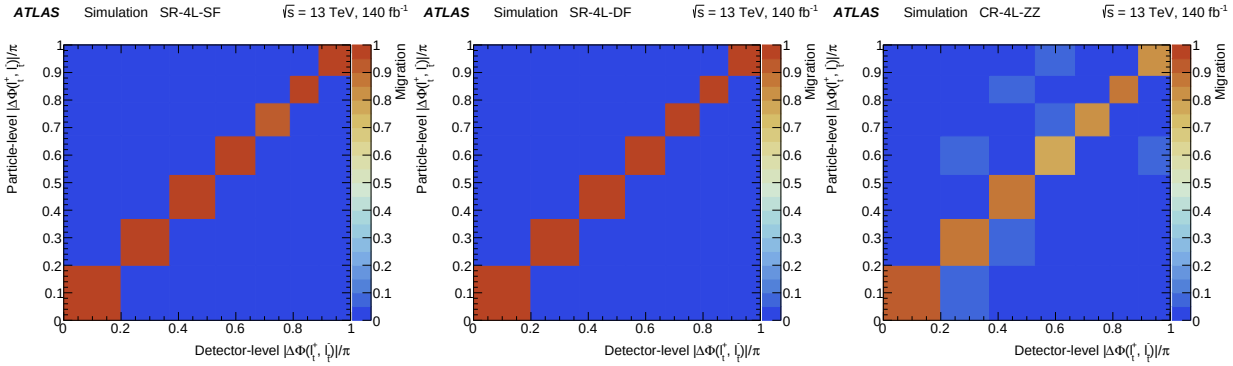

(a) SR-4ℓ-SF **(b)** SR-4ℓ-DF **(c)** CR-4ℓ-ZZ

Figure 7.10: Migration matrices with respect to particle-level $|\Delta\phi(\ell,\ell)|$ in the tetralepton regions.

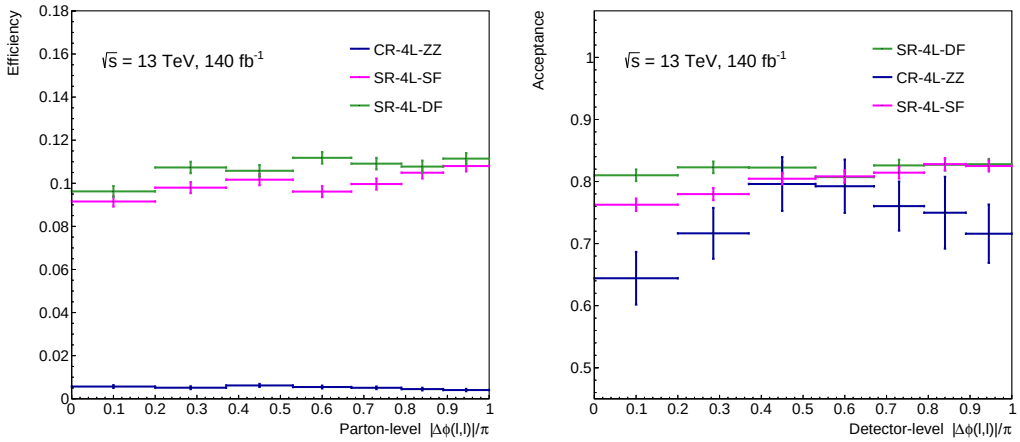

Figure 7.11: Efficiency (left) and acceptance (right) corrections to parton-level for $|\Delta\phi(\ell,\ell)|$ in the tetralepton regions.

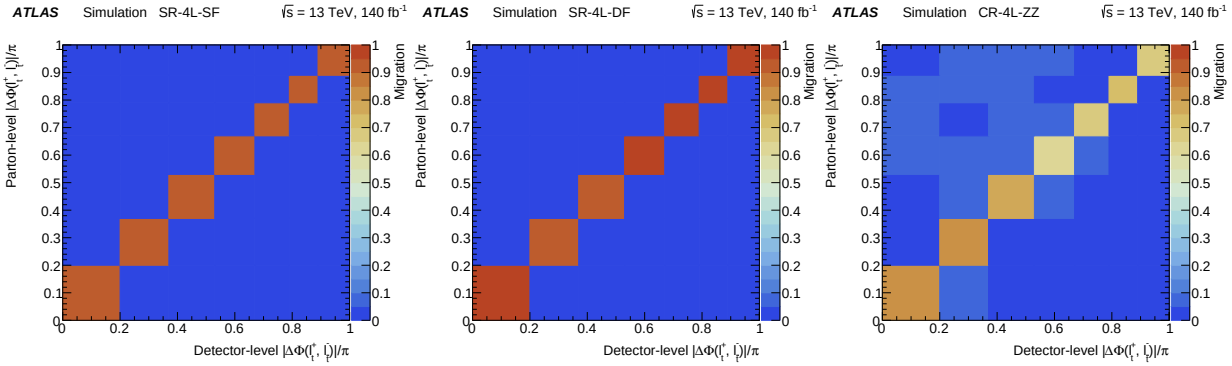

(a) SR-4ℓ-SF **(b)** SR-4ℓ-DF **(c)** CR-4ℓ-ZZ

Figure 7.12: Migration matrices with respect to parton-level $|\Delta\phi(\ell,\ell)|$ in the tetralepton regions.

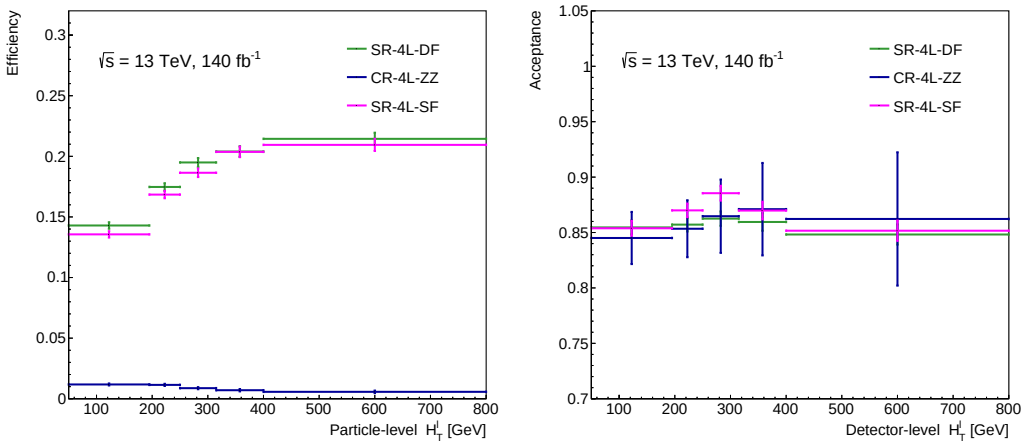

Figure 7.13: Efficiency (left) and acceptance (right) corrections to particle-level for H_{T}^{ℓ} in the tetralepton regions.

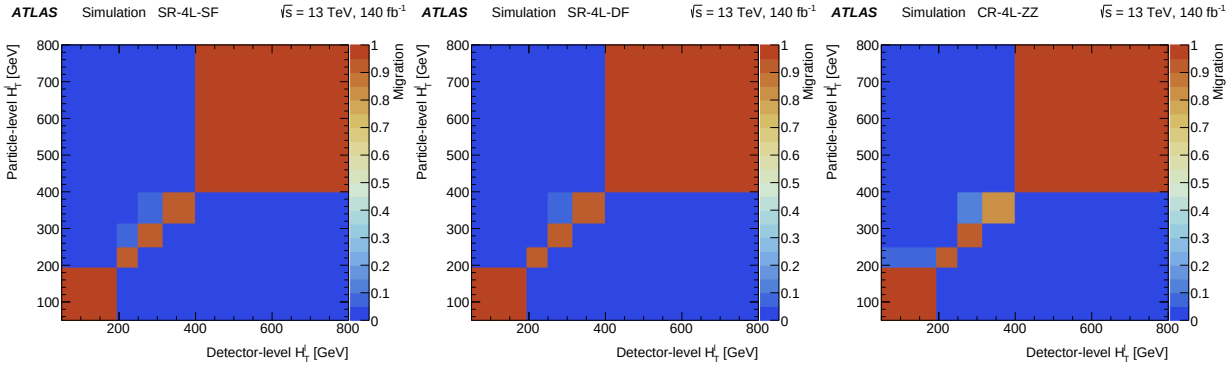

(a) SR-4ℓ-SF **(b)** SR-4ℓ-DF **(c)** CR-4ℓ-ZZ

Figure 7.14: Migration matrices with respect to particle-level H_{T}^{ℓ} in the tetralepton regions.

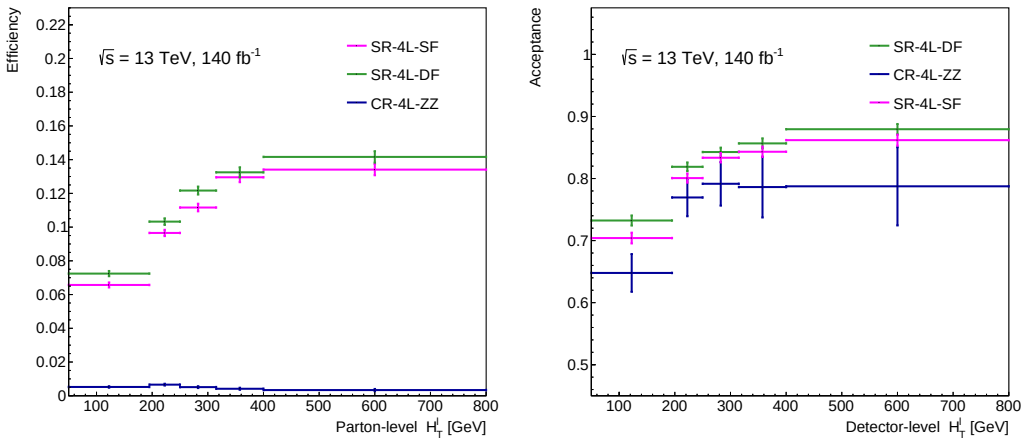

Figure 7.15: Efficiency (left) and acceptance (right) corrections to parton-level for H_{T}^{ℓ} in the tetralepton regions.

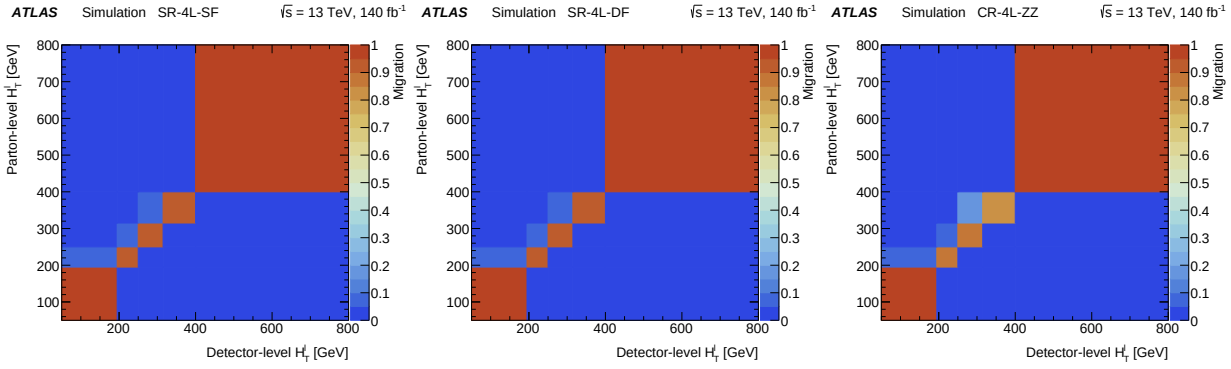

(a) SR-4ℓ-SF **(b)** SR-4ℓ-DF **(c)** CR-4ℓ-ZZ

Figure 7.16: Migration matrices with respect to parton-level H_{T}^{ℓ} in the tetralepton regions.

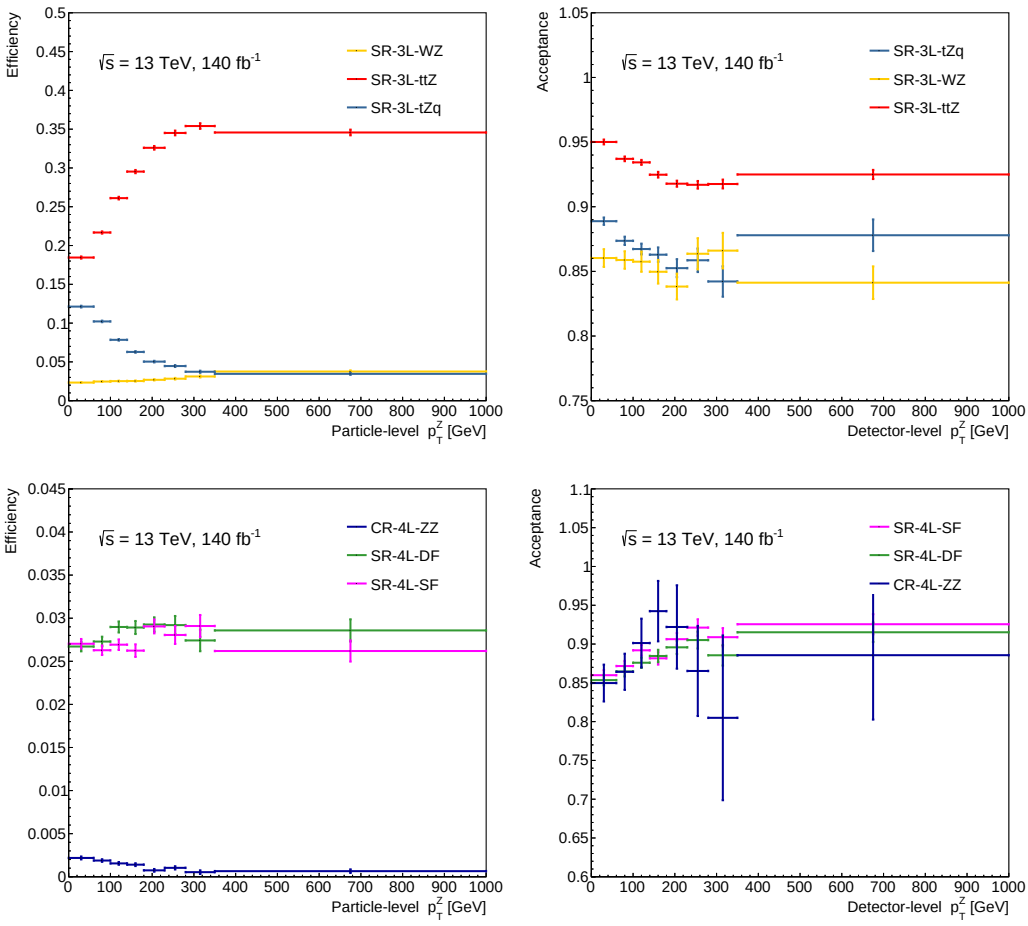

Figure 7.17: Efficiency (left) and acceptance (right) corrections to particle-level for p_{T}^{Z} in the trilepton (top) and tetralepton (bottom) regions.

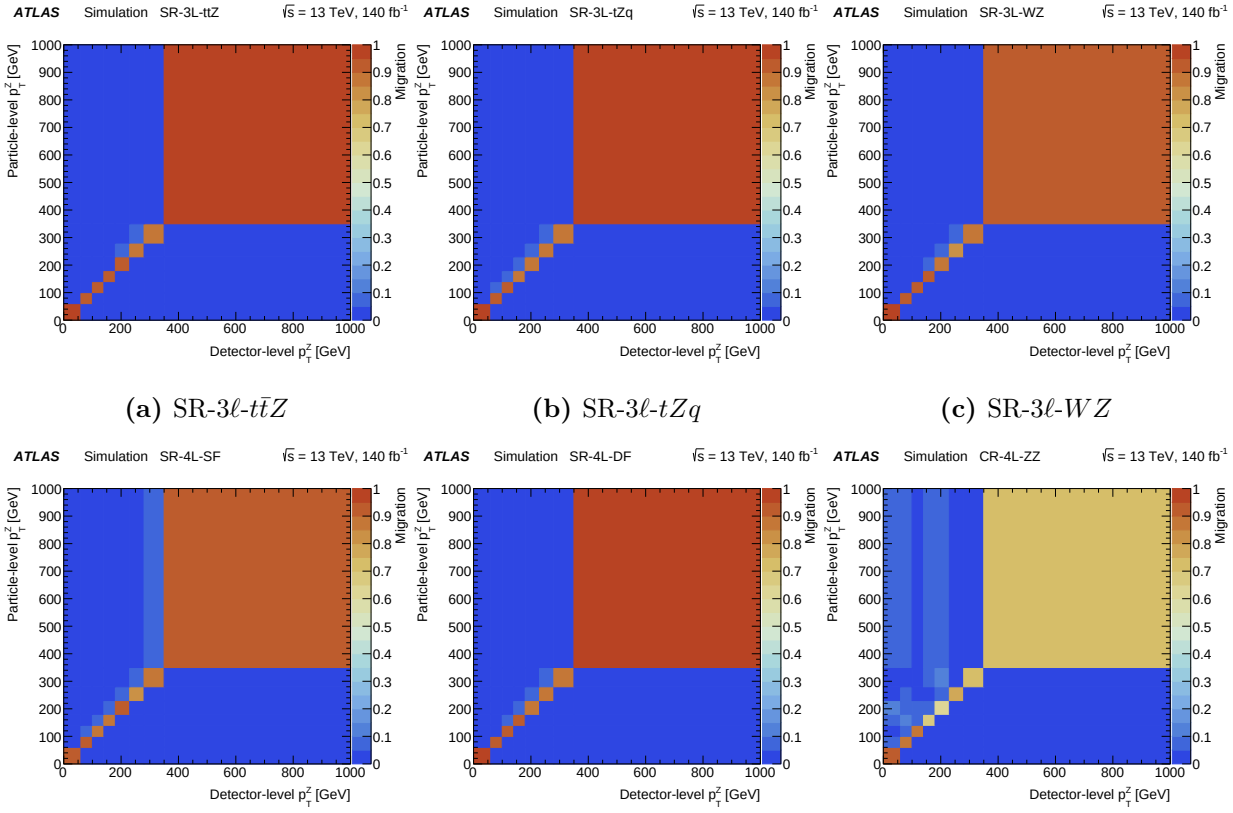

(a) SR-3ℓ-$t\bar{t}Z$ **(b)** SR-3ℓ-tZq **(c)** SR-3ℓ-WZ

(d) SR-4ℓ-SF **(e)** SR-4ℓ-DF **(f)** CR-4ℓ-ZZ

Figure 7.18: Migration matrices with respect to particle-level p_{T}^{Z} in the trilepton and tetralepton regions.

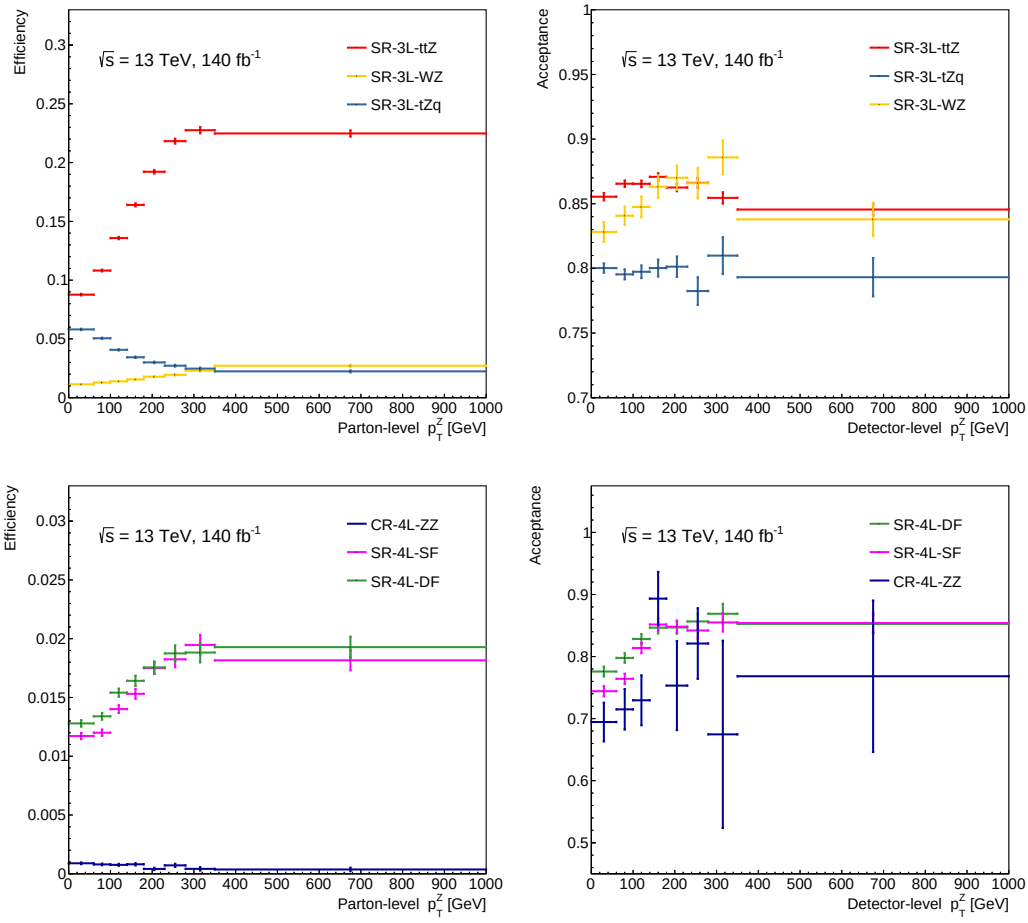

Figure 7.19: Efficiency (left) and acceptance (right) corrections to parton-level for p_{T}^{Z} in the trilepton (top) and tetralepton (bottom) regions.

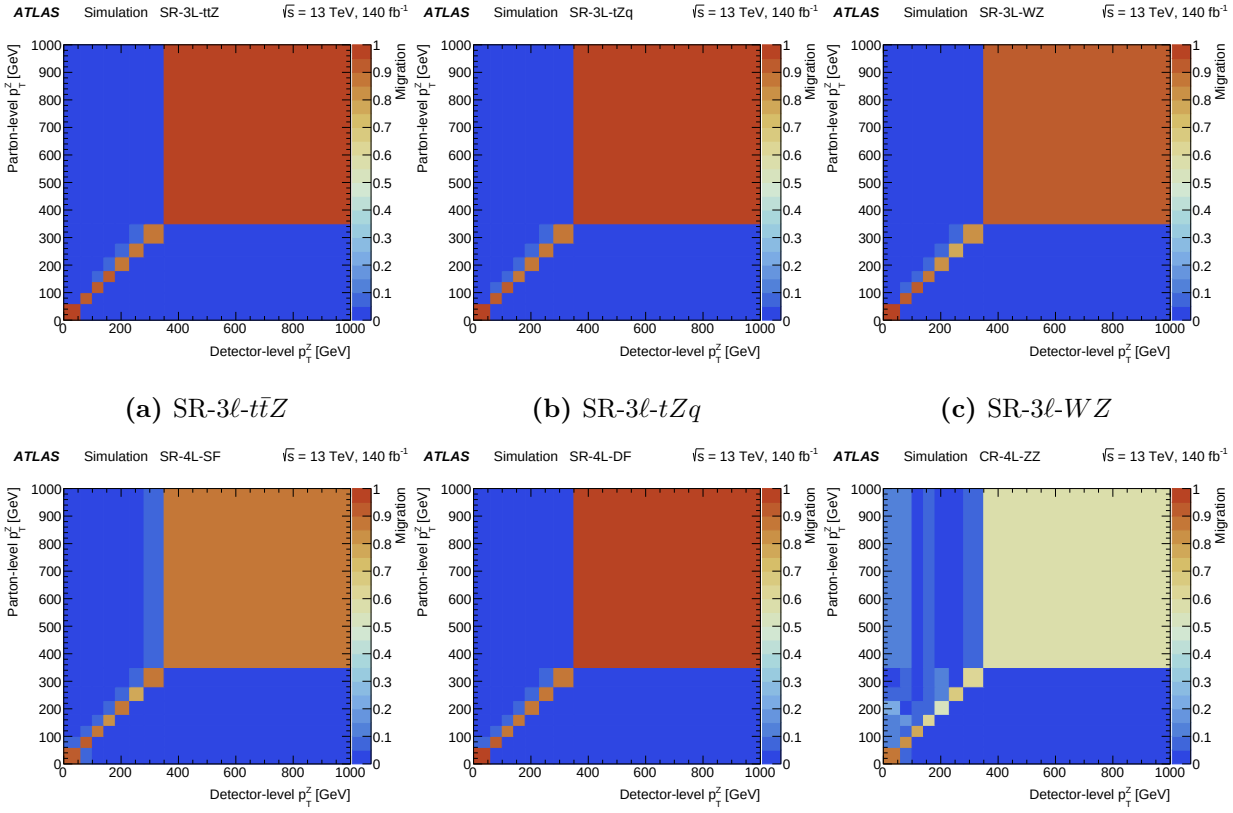

(a) SR-3ℓ-$t\bar{t}Z$ **(b)** SR-3ℓ-tZq **(c)** SR-3ℓ-WZ

(d) SR-4ℓ-SF **(e)** SR-4ℓ-DF **(f)** CR-4ℓ-ZZ

Figure 7.20: Migration matrices with respect to parton-level p_{T}^{Z} in the trilepton and tetralepton regions.

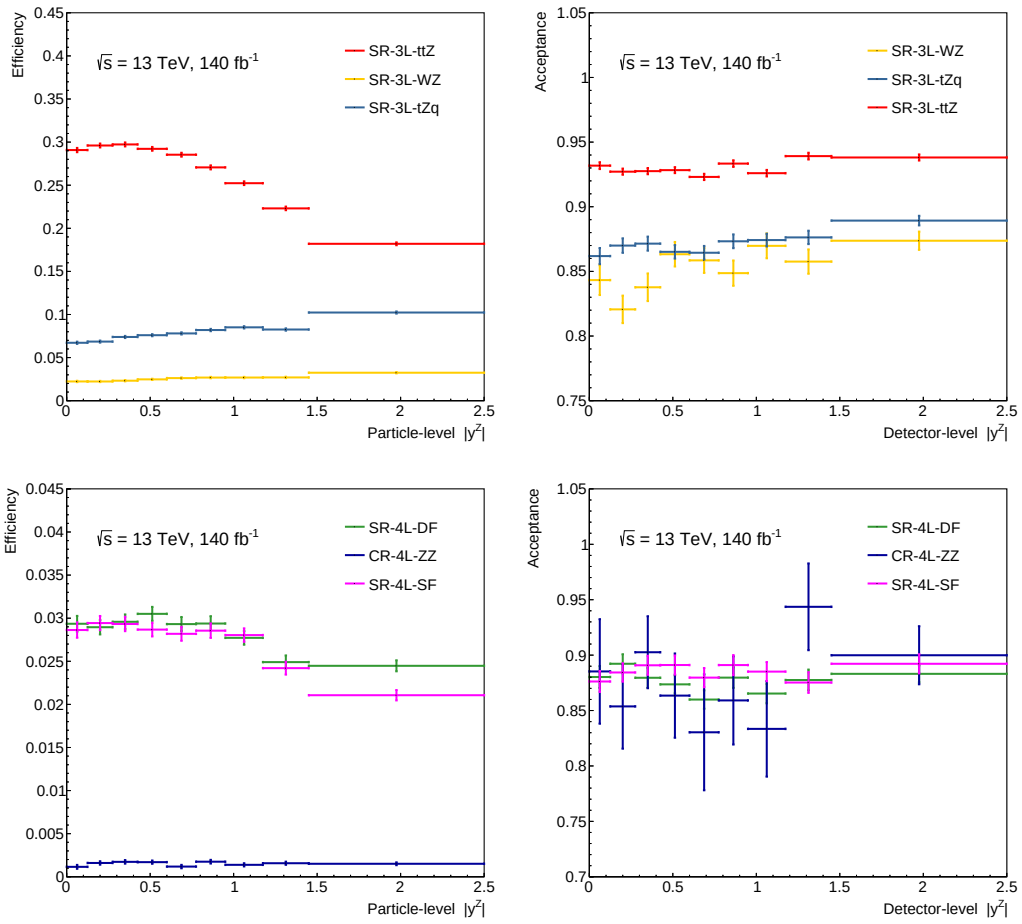

Figure 7.21: Efficiency (left) and acceptance (right) corrections to particle-level for $|y^Z|$ in the trilepton (top) and tetralepton (bottom) regions.

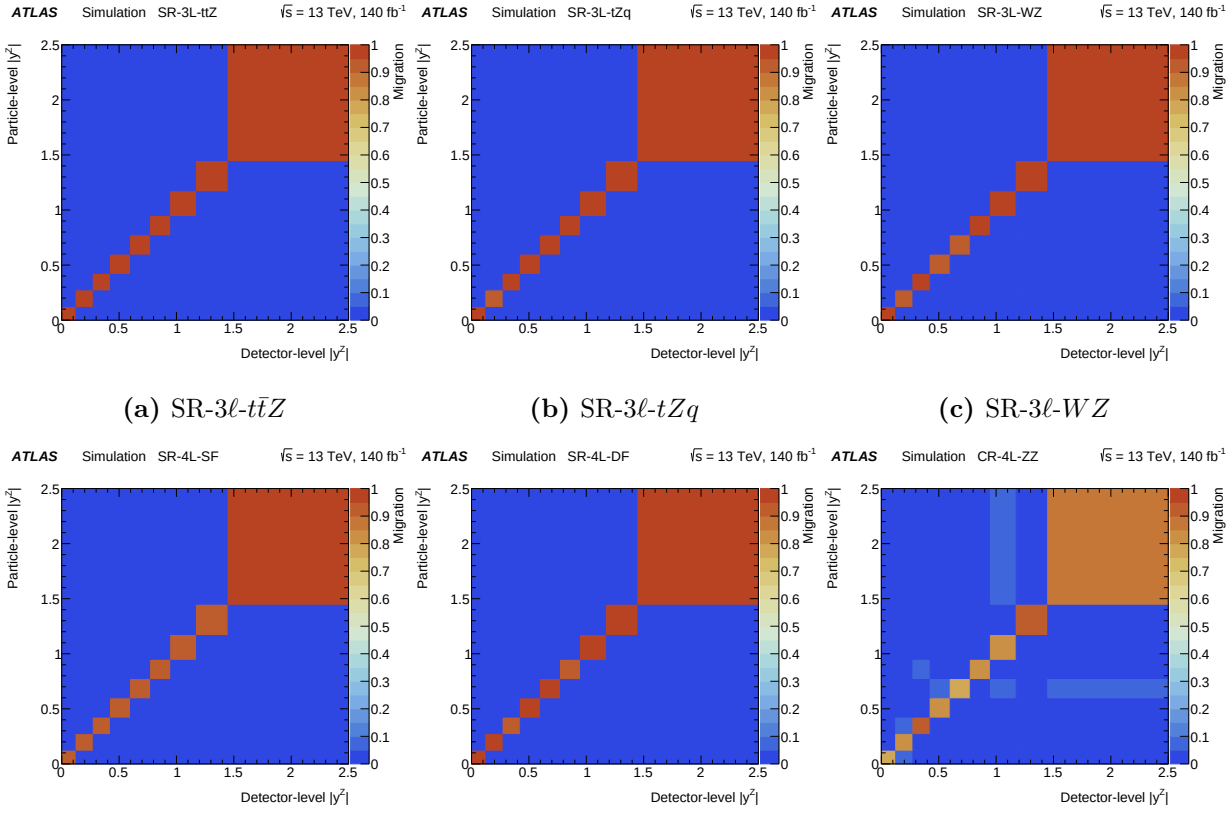

(a) SR-3ℓ-$t\bar{t}Z$ **(b)** SR-3ℓ-tZq **(c)** SR-3ℓ-WZ

(d) SR-4ℓ-SF **(e)** SR-4ℓ-DF **(f)** CR-4ℓ-ZZ

Figure 7.22: Migration matrices with respect to particle-level $|y^Z|$ in the trilepton and tetralepton regions.

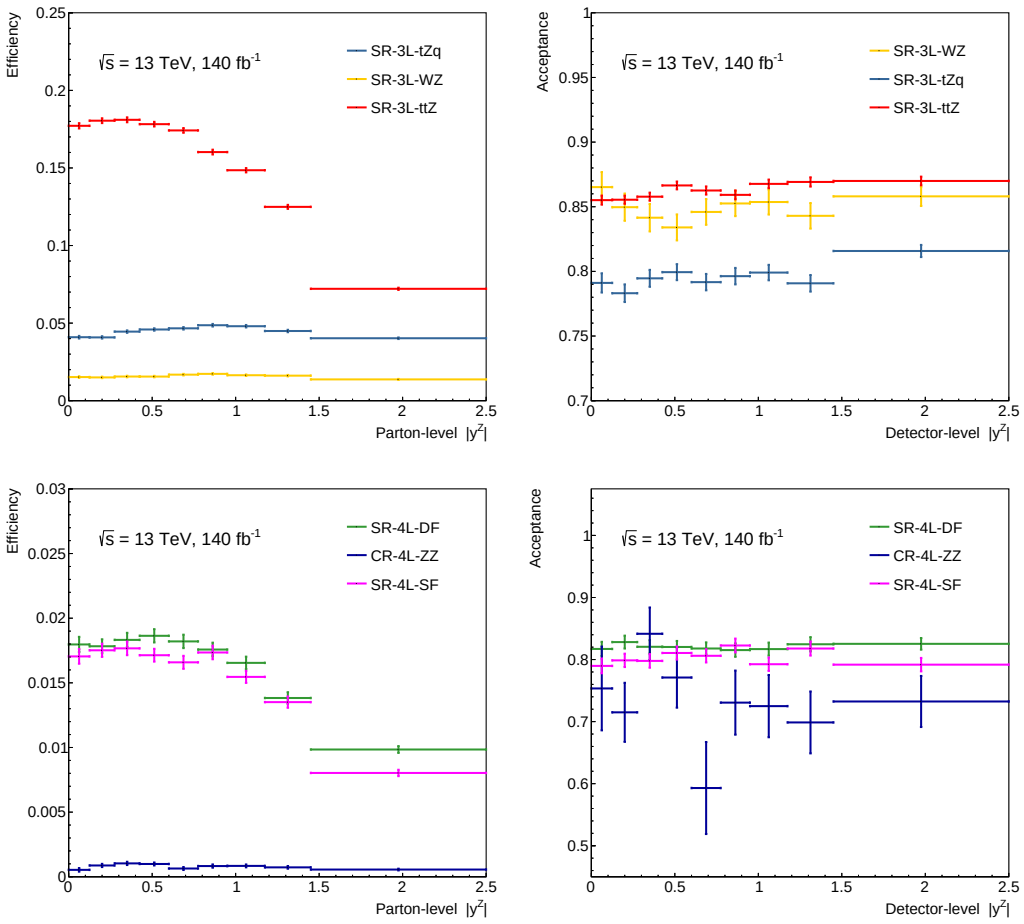

Figure 7.23: Efficiency (left) and acceptance (right) corrections to parton-level for $|y^Z|$ in the trilepton (top) and tetralepton (bottom) regions.

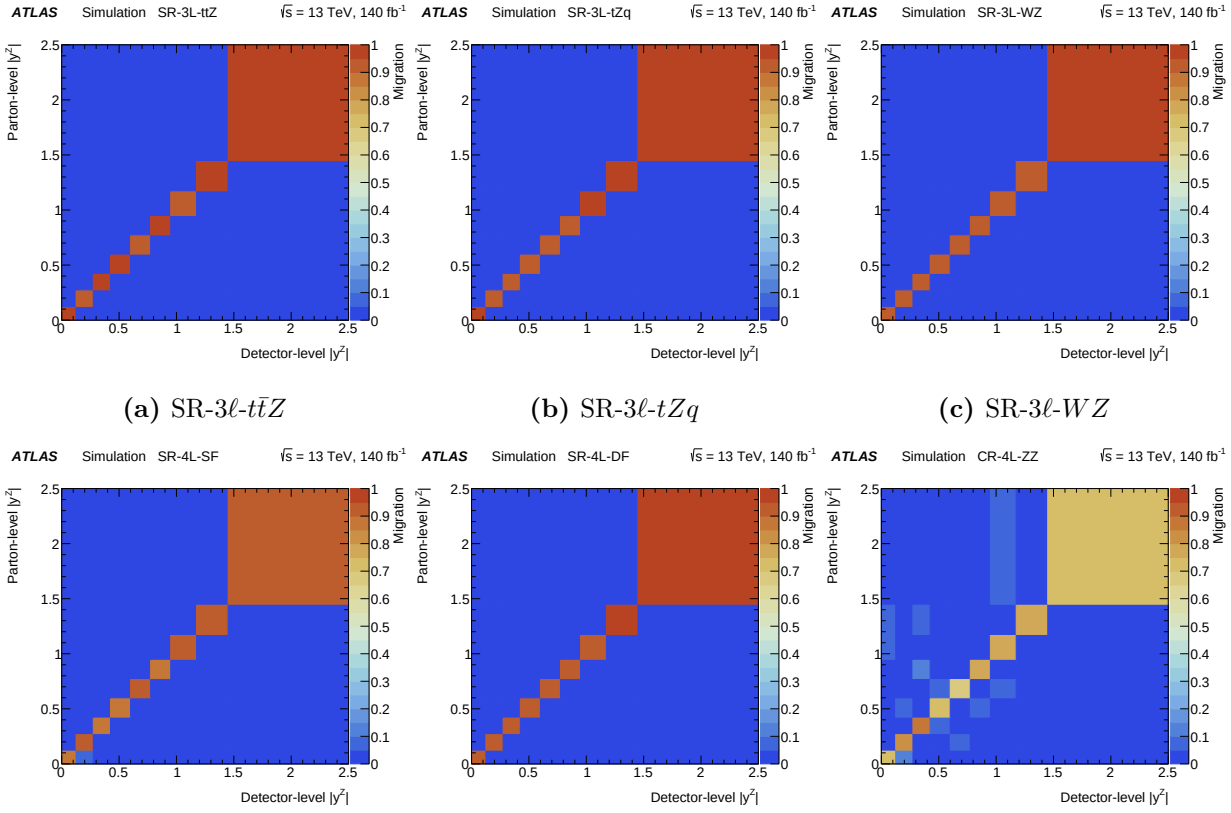

(a) SR-3ℓ-$t\bar{t}Z$ **(b)** SR-3ℓ-tZq **(c)** SR-3ℓ-WZ

(d) SR-4ℓ-SF **(e)** SR-4ℓ-DF **(f)** CR-4ℓ-ZZ

Figure 7.24: Migration matrices with respect to parton-level $|y^Z|$ in the trilepton and tetralepton regions.

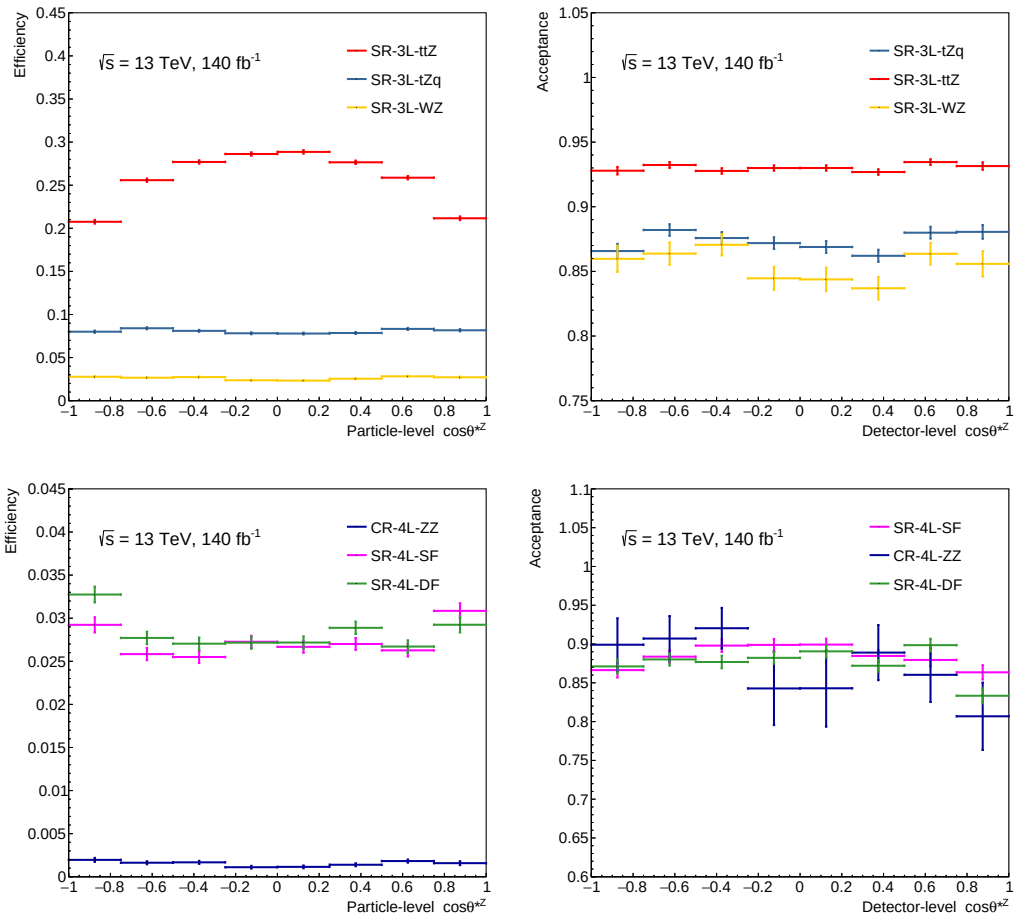

Figure 7.25: Efficiency (left) and acceptance (right) corrections to particle-level for $\cos(\theta_Z^\star)$ in the trilepton (top) and tetralepton (bottom) regions.

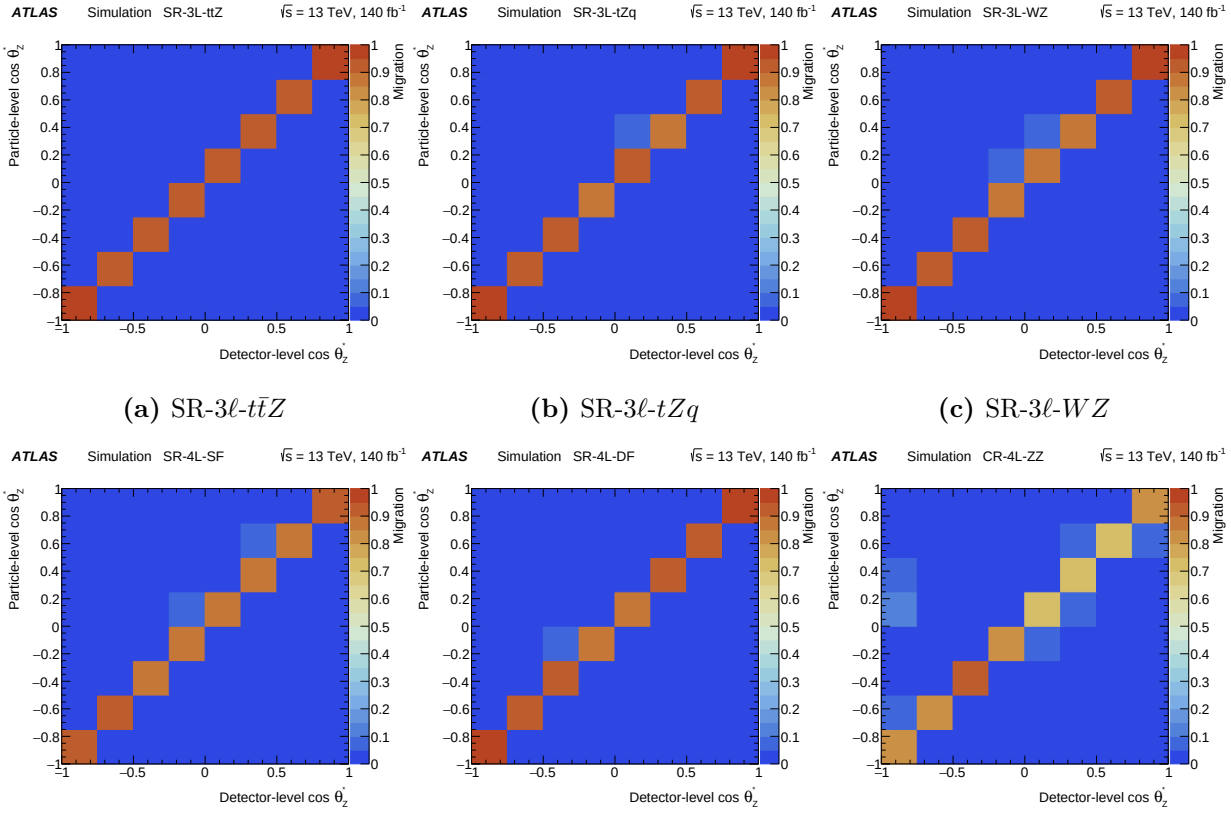

(a) SR-3ℓ-$t\bar{t}Z$ **(b)** SR-3ℓ-tZq **(c)** SR-3ℓ-WZ

(d) SR-4ℓ-SF **(e)** SR-4ℓ-DF **(f)** CR-4ℓ-ZZ

Figure 7.26: Migration matrices with respect to particle-level $\cos(\theta^{\star}_{Z})$ in the trilepton and tetralepton regions.

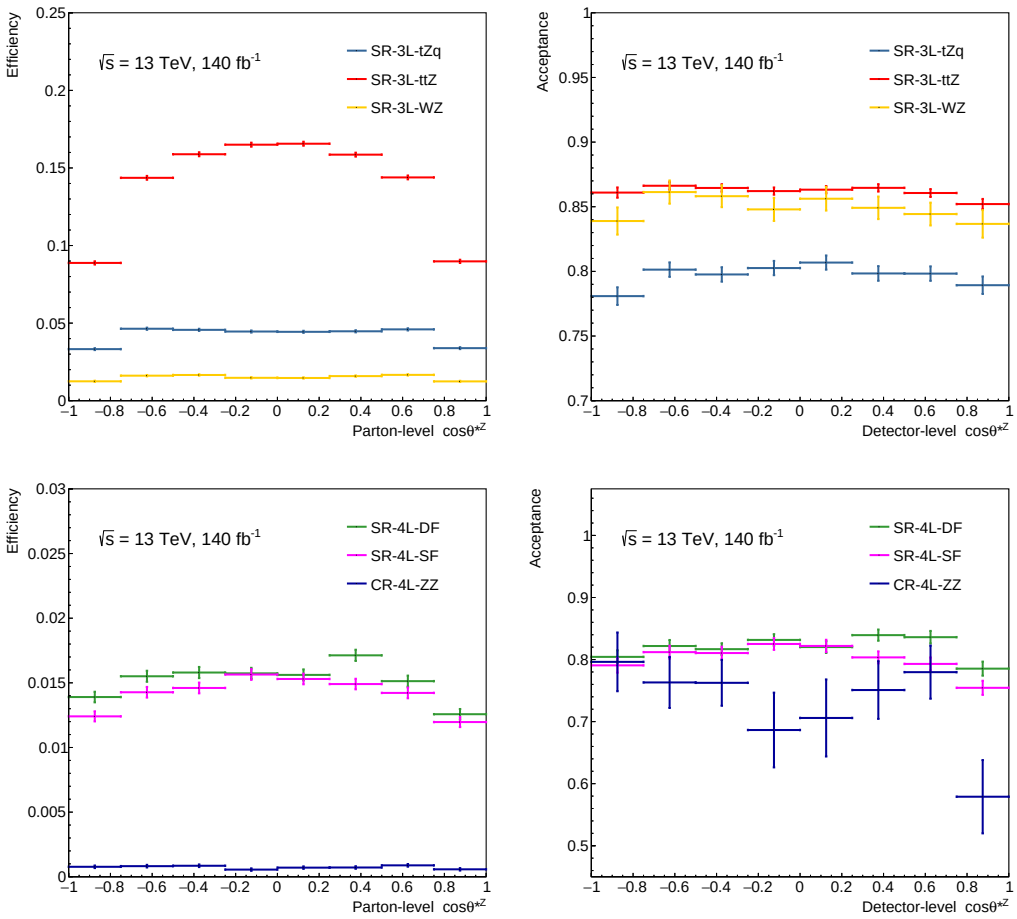

Figure 7.27: Efficiency (left) and acceptance (right) corrections to parton-level for $\cos(\theta_Z^\star)$ in the trilepton (top) and tetralepton (bottom) regions.

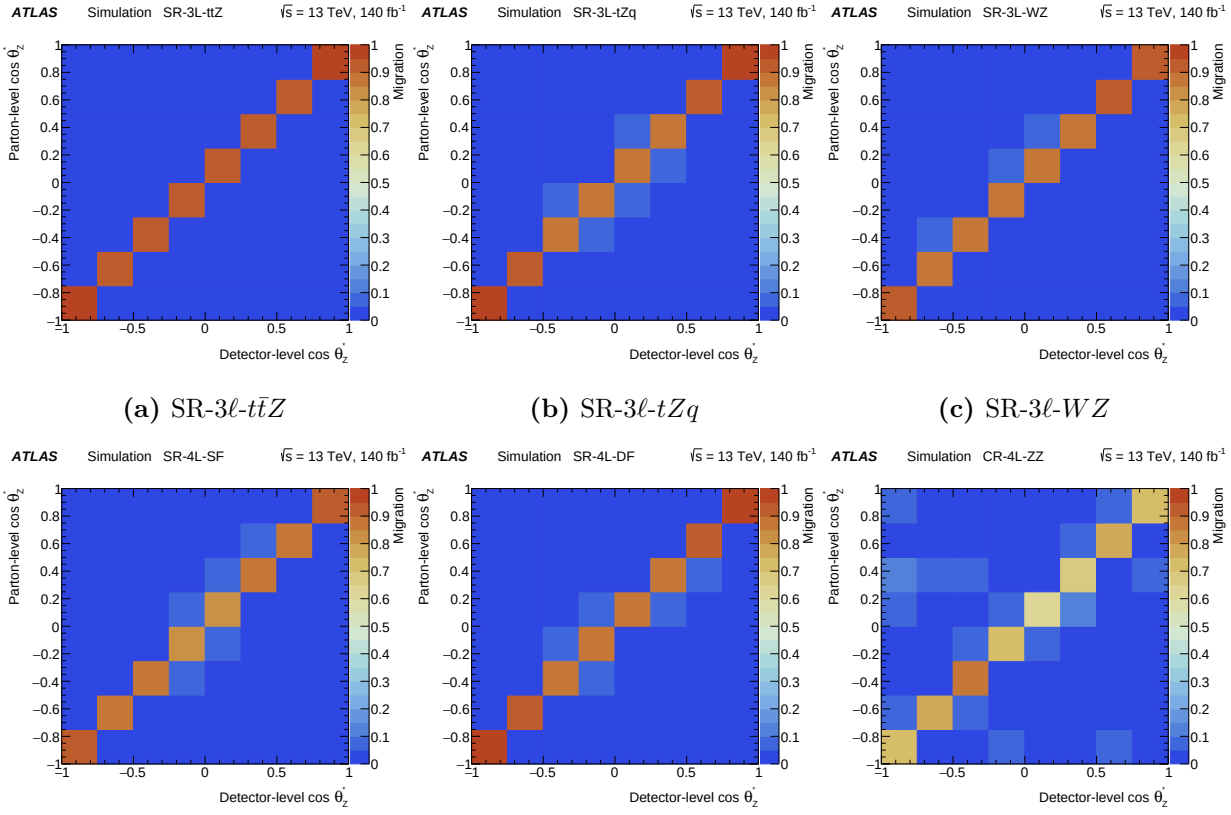

(a) SR-3ℓ-$t\bar{t}Z$ **(b)** SR-3ℓ-tZq **(c)** SR-3ℓ-WZ

(d) SR-4ℓ-SF **(e)** SR-4ℓ-DF **(f)** CR-4ℓ-ZZ

Figure 7.28: Migration matrices with respect to parton-level $\cos(\theta^{\star}_{Z})$ in the trilepton and tetralepton regions.

Chapter 8

Validation of the unfolding method

The unfolding method used to measure the $t\bar{t}Z$ differential cross-sections could introduce bias to the results. Bias can arise because the analysis is designed using a finite number of simulated events. If observed data is not well-described by the simulated events, then we need to check that the method can be applied to a different dataset and still reliably produce the true distribution. Additionally, analysis design choices such as the binning of observables can affect the stability of the unfolding method. For example, distribution binning that results in large migration of events between bins can amplify biases already present in the unfolding method. Tests of the unfolding method are performed to check that there are no significant biases within the analysis setup. This chapter describes three types of test that are performed: closure, pull and stress tests. Validation tests are performed before applying the method to observed data. These tests use simulated pseudo-data to test various scenarios.

8.1 Stability with respect to independent datasets

The *closure test* verifies that the unfolding method is unbiased when applied to a statistically-independent sample. The nominal MC signal sample is divided randomly into two statistically independent samples. One sample is used as pseudo-data, while the other is used to derive unfolding corrections. The full event selection procedure described in Chapter 6 is applied to

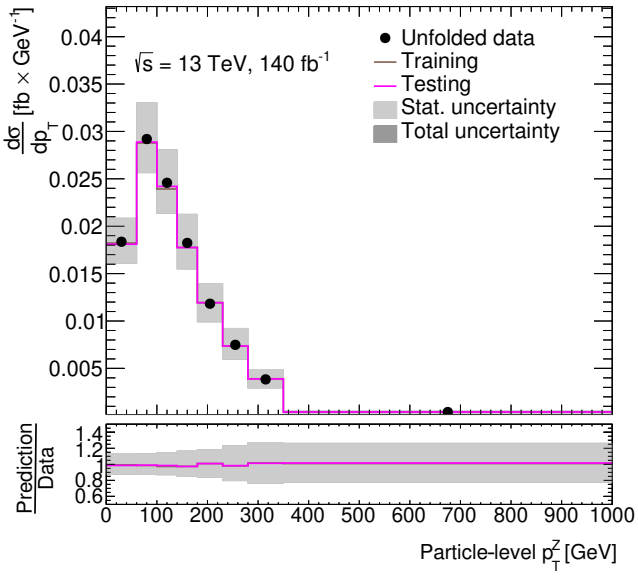

Figure 8.1: Closure test for the p_{T}^{Z} observable in the combination of the trilepton and tetralepton channels at particle-level.

both samples. The closure test is passed if pseudo-data unfolded with corrections derived from a statistically-independent dataset are in agreement, within statistical uncertainties, with the true distribution. Closure tests are performed for each differential cross-section measurement observable. Only statistical uncertainties are considered in the fit for the closure test and the backgrounds are not included. To give an example of the closure test, the unfolded pseudo-data is compared to the independent signal sample at particle-level in Figure 8.1 for the p_{T}^{Z} observable in the combination of the trilepton and tetralepton channel.

If the unfolded pseudo-data and true distribution are in good agreement, more specifically if the difference between the two samples is smaller than the associated statistical uncertainty in the bin, then the test is considered to have passed. This can be quantified with a χ^2 test:

$$\chi^2 = \sum_{ij} (n_i - \nu_i) C_{ij}^{-1} (n_j - \nu_j), \tag{8.1}$$

where n_i is the measured cross-section value, ν_i is the expected cross-section value and C_{ij} is the covariance matrix estimated by the unfolding fit. This includes bin-to-bin correlations, that are intrinsic to the unfolding method, arising from statistical uncertainty. Values of χ^2 that are

Table 8.1: Summary of the χ^2/NDF values for the closure tests observables measured in the tetralepton channel and the combination of the trilepton and tetralepton channels which are unfolded to particle- and parton-level where possible.

Observable	Channel	Particle-level	Parton-level
H_{T}^{ℓ}	4ℓ	0.052/5	0.048/5
$\lvert\Delta\phi(\ell,\ell)\rvert$	4ℓ	0.019/7	0.027/7
N_{jets}	4ℓ	0.023/3	–
p_{T}^{Z}	$3\ell + 4\ell$	0.081/8	0.114/8
$\lvert y^{Z}\rvert$	$3\ell + 4\ell$	0.055/9	0.089/9
$\cos(\theta_{Z}^{\star})$	$3\ell + 4\ell$	0.065/8	0.100/8

close to one indicate that the pseudo-data are well-represented by the model. The χ^2 per degree of freedom (χ^2/NDF) is shown for each observable in Table 8.1. The χ^2/NDF values are small and show good agreement between the unfolded pseudo-data and the true distribution. They are much less than one because we use many more simulated events than there are expected in the data. The closure test results show that the profile likelihood unfolding method is able to recover the true distribution and contains no significant bias.

8.2 Stability with respect to statistical fluctuations

The *pull test* checks that the unfolding technique is unbiased in the presence of statistical fluctuations in the dataset and that the statistical uncertainty returned by the fit is reliable. A set of 5,000 pseudo-experiments are obtained by repeatedly smearing the simulated detector-level distribution for each observable with a Poisson distribution. The smeared pseudo-data is then used as input to the nominal fit. We expect the measured POI values to be a Gaussian distribution with mean one and width σ, where σ is the expected uncertainty on μ from the nominal fit. This test is performed using the nominal fit excluding systematic uncertainties.

Figure 8.2 shows the POIs for the second and last bins of the distribution resulting from the fit to the pseudo-experiments for each bin of p_{T}^{Z} at particle-level in the combination of the trilepton and tetralepton channels. In general, well-populated bins, such as the second bin, are

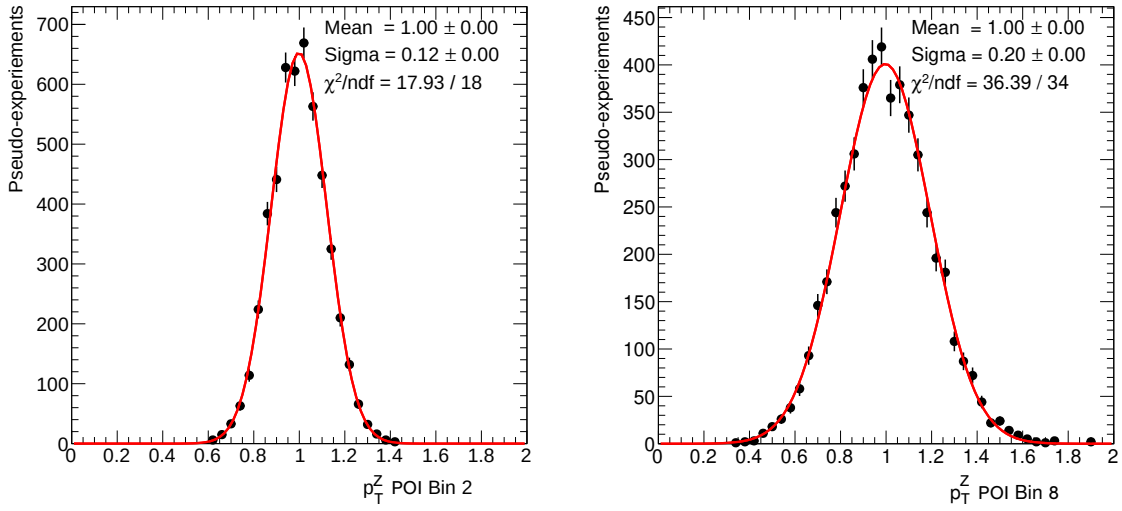

Figure 8.2: Distribution of the estimated POI resulting from 5000 pseudo-experiment fits for the second (left) and eighth (right) bins of the p_{T}^{Z} distribution.

approximately Gaussian-distributed while the bins towards the tail of the distribution, such as the eighth bin, contain fewer events and skew towards a Poisson distribution. This can be understood by knowing that the asymptotic limit of the Poisson distribution is the Gaussian distribution.

In the absence of bias, the difference between the mean of the pseudo-experiments for each POI, μ_{fitted}, and the nominal POI value should be consistent with zero. If the unfolding method appropriately estimates the POI statistical uncertainties, the root-mean-squared error (RMS) of the pseudo-experiments for each POI, σ_{fitted}, should be consistent with the uncertainties estimated in the nominal unfolding. Figure 8.3 shows a summary of the pull test results for the tetralepton measurement observables and Figure 8.4 shows a summary of the pull test results for the observables unfolded in the combination of the trilepton and tetralepton channels. The blue markers show the mean of the difference between pseudo-experiments and nominal measurements of POIs in Asimov data. The red markers show the pseudo-experiment RMS errors with respect to the statistical uncertainties of the nominal unfolding. In general, the values of σ_{fitted} show consistency with unity. There is a small non-closure of μ_{fitted} in some bins e.g. bin six of $|y^{Z}|$ and bin two of $\cos(\theta_{Z}^{\star})$, but these are small (less than 5%). Therefore, the profile likelihood unfolding method is considered to be robust against statistical fluctuations.

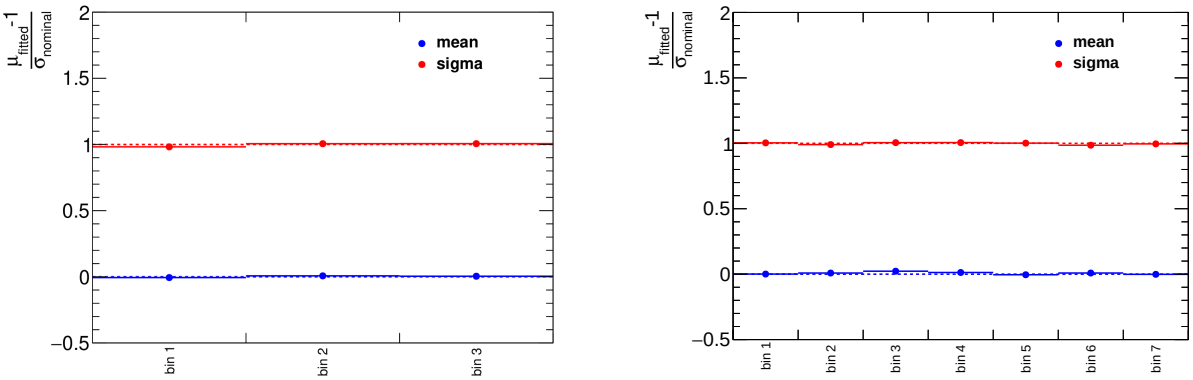

(a) N_{jets}

(b) $|\Delta\phi(\ell,\ell)|$

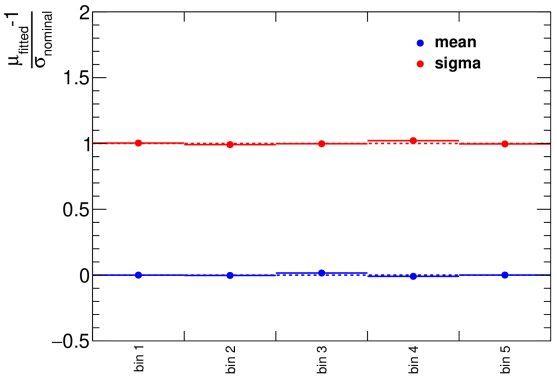

(c) H_{T}^{ℓ}

Figure 8.3: Summary of the pull tests for the unfolding of the tetralepton observables to particle-level.

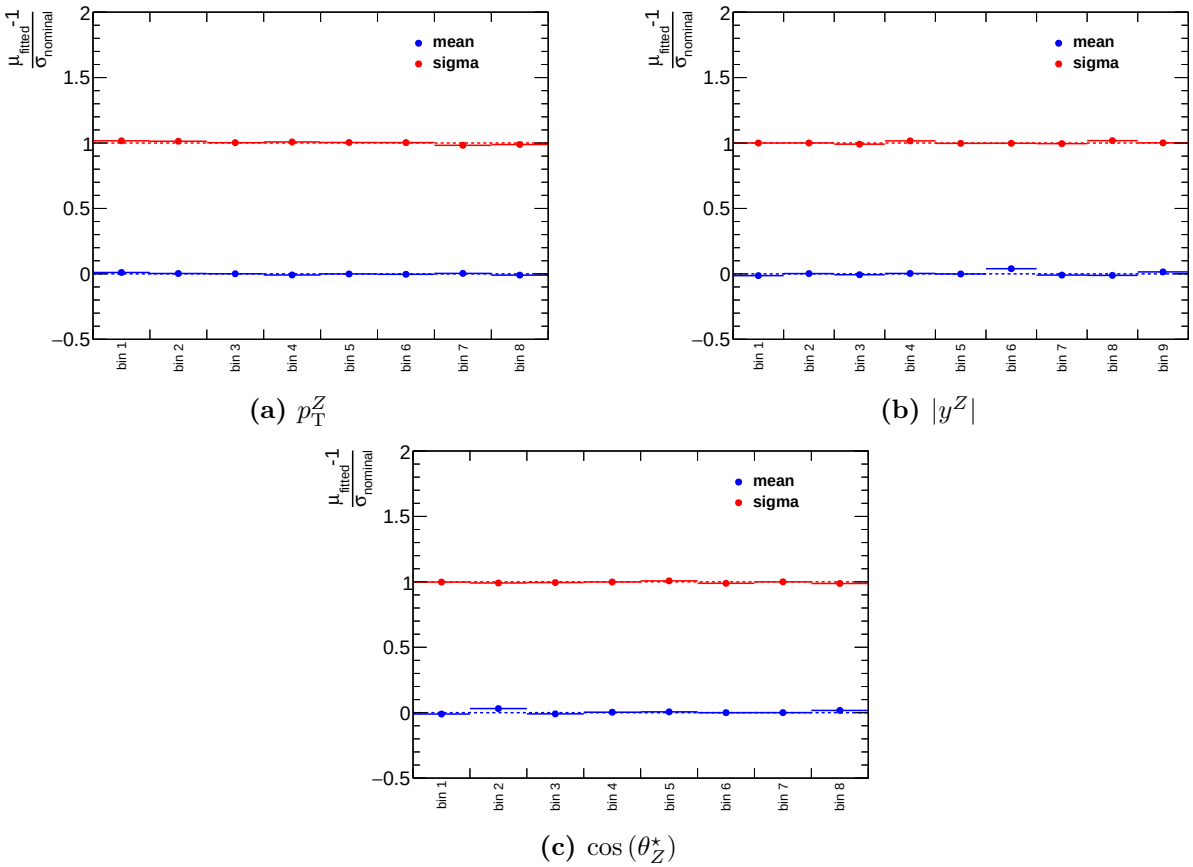

(a) p_{T}^{Z} **(b)** $|y^{Z}|$

(c) $\cos(\theta_{Z}^{\star})$

Figure 8.4: Summary of the pull tests for the unfolding of the combined trilepton and tetralepton observables to particle-level.

8.3 Capacity to recover the underlying shape

The unfolding method can introduce shape bias towards the distribution predicted by the nominal signal sample. This potential bias is especially problematic in the case where the observed data distribution has a different shape to the prediction. Contributions to the $t\bar{t}Z$ differential cross-sections could be missed in data if the method is biased towards the SM distribution. A *stress test* aims to verify that the unfolding method is able to recover any difference in shape between data and the simulated event sample used to derive the unfolding corrections. Contributions from new physics could change the shape of a differential observable distribution in data with respect to the SM: the profile likelihood unfolding method must be able to recover the data distribution shape without bias.

Two stress tests are performed for each unfolded observable distribution. For each test, a pseudo-dataset is created by reweighting the nominal signal prediction, changing the distribution shape, and adding this to the nominal background prediction. The pseudo-data is then used as input to the nominal fit. The unfolded pseudo-data should agree with the pseudo-data truth-level distribution and not be biased towards the nominal truth-level distribution. Stress tests can be performed in a number of ways according to how the pseudo-data is constructed; physically-motivated reweighting is often used. The first stress test uses linear reweighting across the p_{T}^{Z} observable. The second stress test uses data reweighting. The combination of these tests should cover all new physics scenarios.

8.3.1 Linear reweighting in p_{T}^{Z}

Stress tests are performed by reweighting the nominal signal prediction using a linear function

$$f(x) = 1 + xk, \tag{8.2}$$

where x is the value of p_{T}^{Z} at truth-level and k is a constant that tunes the strength of the weight at high p_{T}^{Z}. The pseudo-data then emulates a new physics model that would

increase or decrease the number of $t\bar{t}Z$ events in the high p_{T}^{Z} region. Specifically, values of $k = [-0.5, -0.25, 0.25, 0.5, 0.75]$ are tested such that events with $p_{\mathrm{T}}^{Z} = 1000\,\mathrm{GeV}$ have an additional weight equal to k.[1] Effective field theory interpretations have shown that potential new physics effects could increase the $t\bar{t}Z$ differential cross-sections at high values of p_{T}^{Z} [26].

This verifies the performance of the unfolding method in different potential data scenarios, specifically when there are modified cross-section contributions at high p_{T}^{Z}. The range of values deliberately tests extreme scenarios, to ensure the unfolding method is unbiased even in these cases. All observable distributions are unfolded with the p_{T}^{Z}-reweighted pseudo-data for each k value at particle- and parton-level. If the unfolding method is unbiased, the unfolded pseudo-data will match the reweighted particle-level distribution (pink line) rather than the nominal truth distribution (brown line). Figure 8.5 shows an example of the stress test results for the p_{T}^{Z} observable. For each value k, the true distribution is recovered by the unfolding method and indicates that the unfolding method is not biased towards the shape of the nominal signal distribution.

For other observables, the shape of the distribution will change in a different way, or not at all, when events are reweighted with respect to p_{T}^{Z}, depending on the correlation between the tested observable and p_{T}^{Z}. Figure 8.6 shows the stress test results for the $|\Delta\phi(\ell,\ell)|$ observable in the tetralepton channel. In this distribution, the decrease/increase in the high-p_{T}^{Z} events results in an overall normalisation effect. The ratio plots in the bottom panels of Figures 8.6a to 8.6d show that the difference between the reweighted sample and the nominal sample is uniform across the $|\Delta\phi(\ell,\ell)|$ distribution. The same stress test is performed in the other tetralepton differential observable distributions, N_{jets} and H_{T}^{ℓ}. The result of the N_{jets} test is shown in Figure 8.7. A small positive slope is seen in the difference between the reweighted and nominal samples, indicating a very small positive correlation between p_{T}^{Z} and jet multiplicity. For the H_{T}^{ℓ} test shown in Figure 8.8, there is a clear positive slope in the ratio between the reweighted and nominal signal samples, indicating a strong correlation between the p_{T}^{Z} and H_{T}^{ℓ} observables, which is as expected. In the combination of the trilepton and tetralepton channels, the shape of the $|y^{Z}|$ and $\cos(\theta_{Z}^{\star})$ observables show no correlation with p_{T}^{Z} and an overall normalisation effect is seen in the reweighted sample. No significant bias towards the nominal setup is observed.

[1] Provided x is given in TeV.

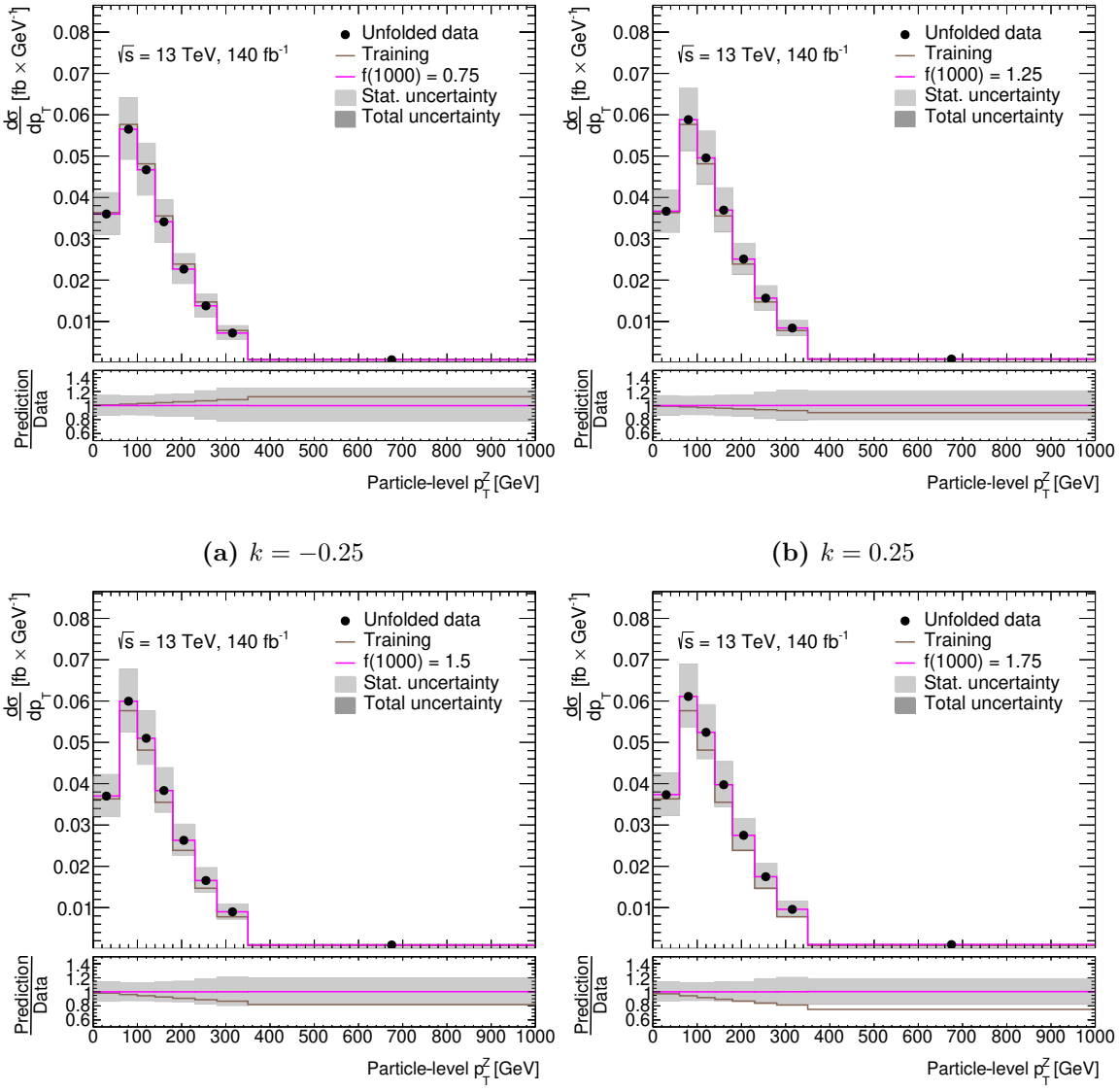

(a) $k = -0.25$ **(b)** $k = 0.25$

(c) $k = 0.50$ **(d)** $k = 0.75$

Figure 8.5: Linear stress test unfolded pseudo-data distributions of p_{T}^{Z} with signal samples modified by a factor k at $p_{\mathrm{T}}^{Z} = 1000\,\mathrm{GeV}$ at particle-level.

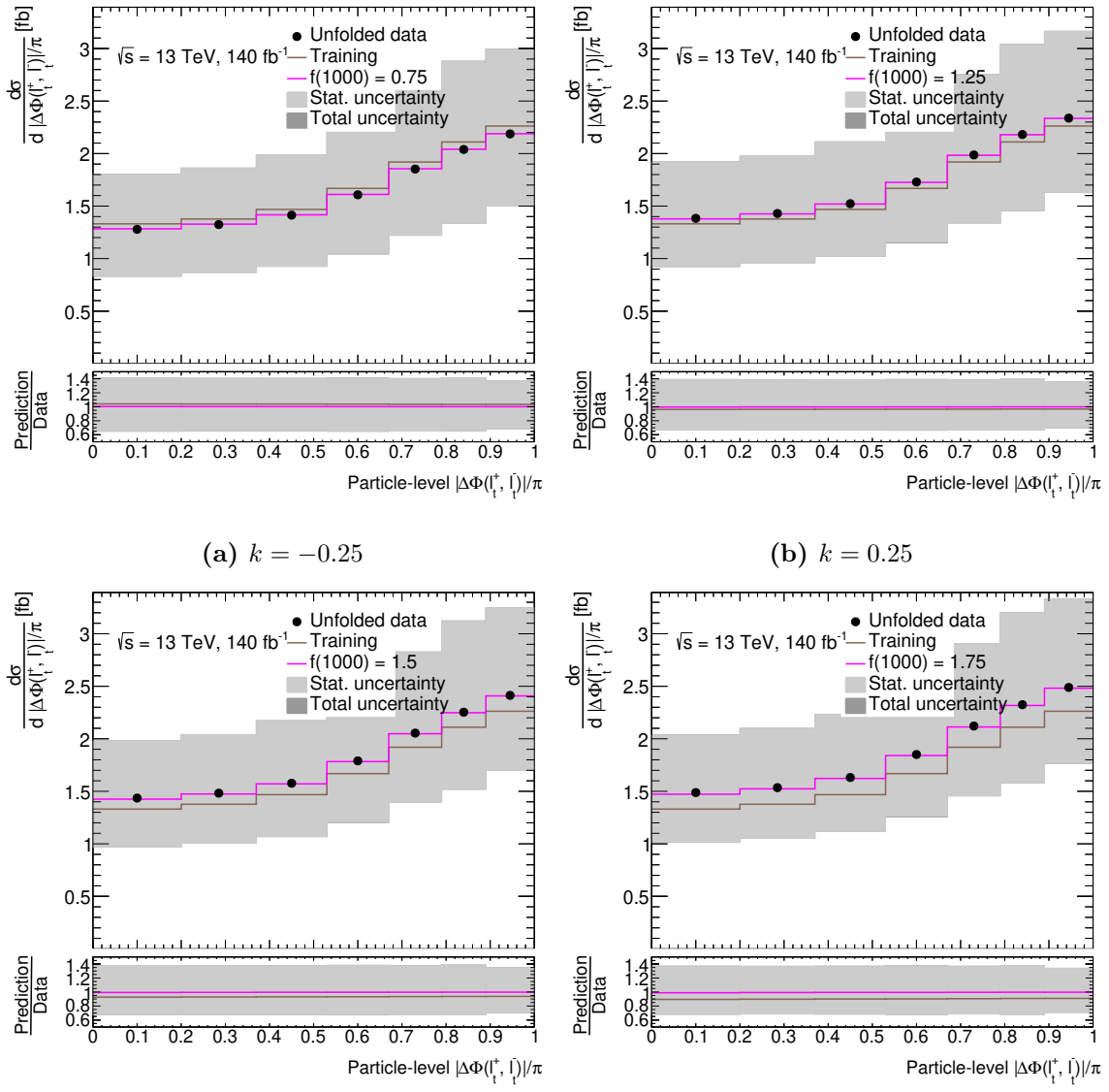

(a) $k = -0.25$ **(b)** $k = 0.25$

(c) $k = 0.50$ **(d)** $k = 0.75$

Figure 8.6: Linear stress test unfolded pseudo-data distributions of $|\Delta\phi(\ell,\ell)|$ with signal samples modified by a factor k at $p_{\mathrm{T}}^{Z} = 1000\,\mathrm{GeV}$ at particle-level.

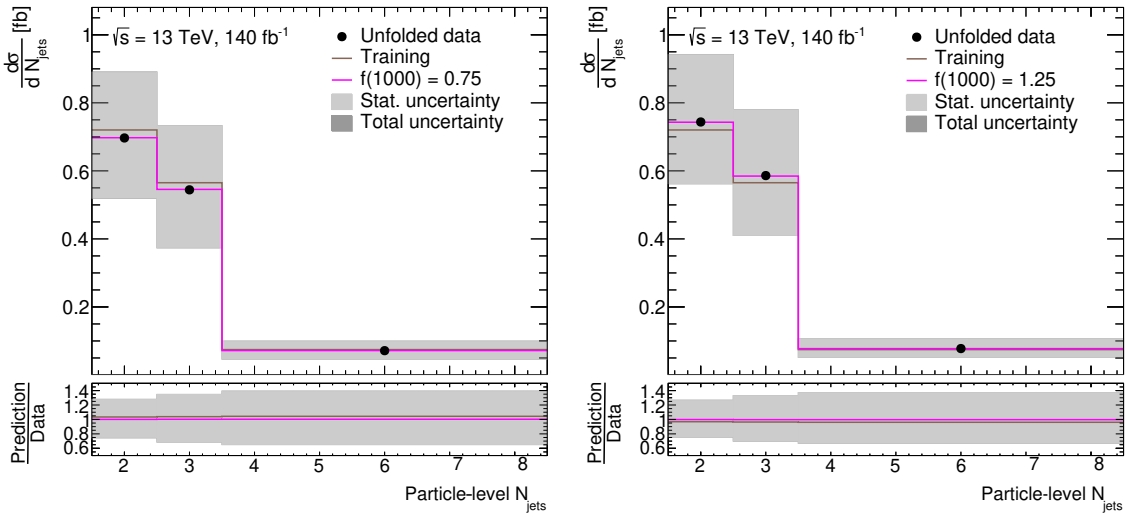

(a) $k = -0.25$

(b) $k = 0.25$

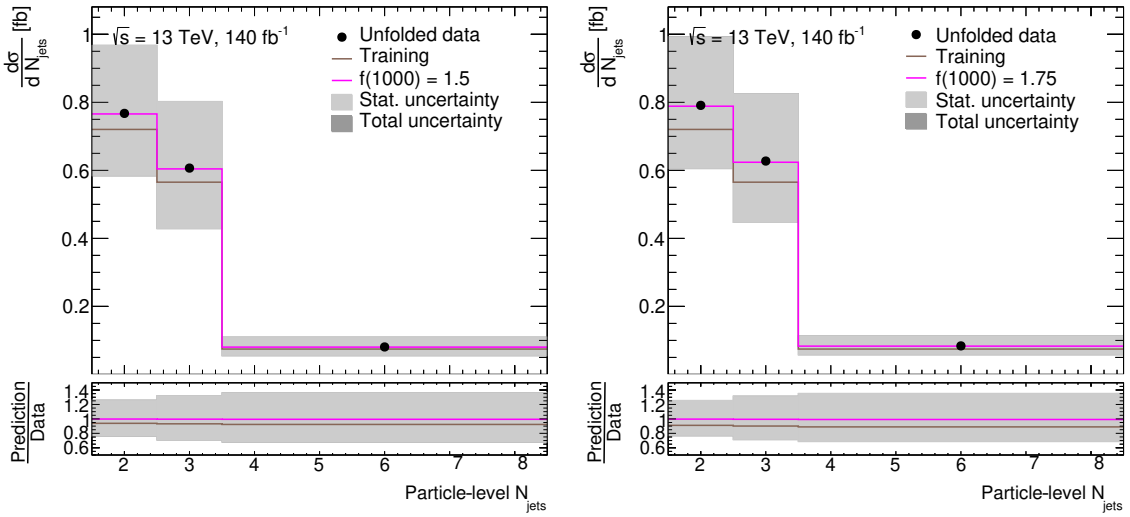

(c) $k = 0.50$

(d) $k = 0.75$

Figure 8.7: Linear stress test unfolded pseudo-data distributions of N_{jets} with signal samples modified by a factor k sample at $p_{\text{T}}^{Z} = 1000\,\text{GeV}$ at particle-level.

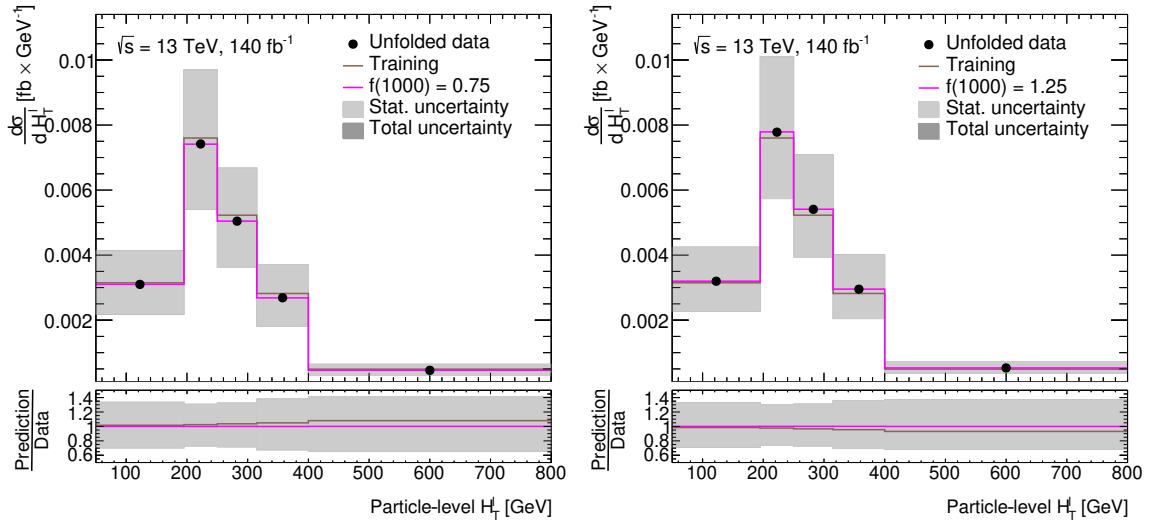

(a) $k = -0.25$

(b) $k = 0.25$

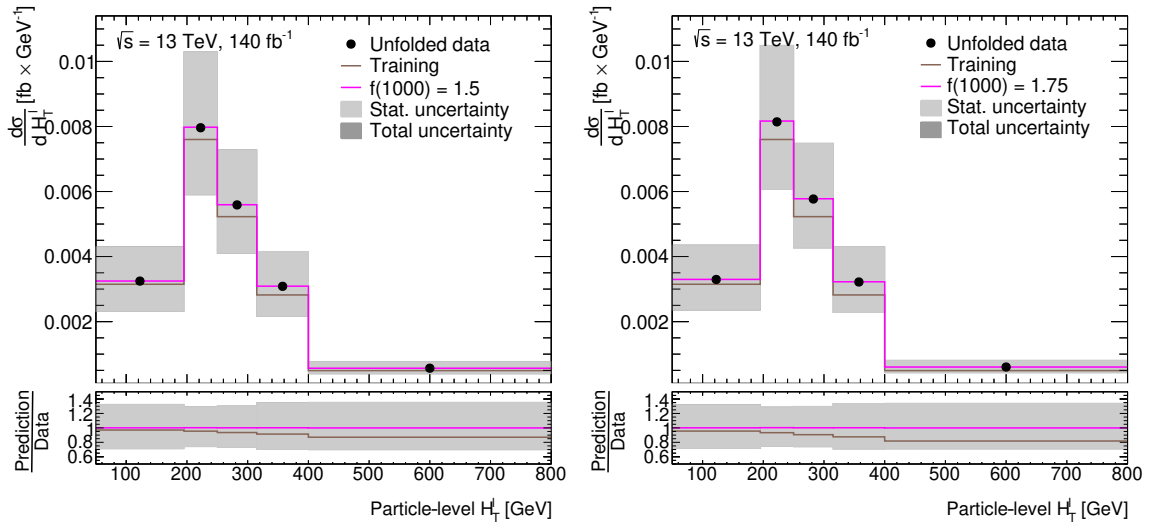

(c) $k = 0.50$

(d) $k = 0.75$

Figure 8.8: Linear stress test unfolded pseudo-data distributions of H_{T}^{ℓ} with signal samples modified by a factor k at $p_{\mathrm{T}}^{Z} = 1000\,\mathrm{GeV}$ at particle-level.

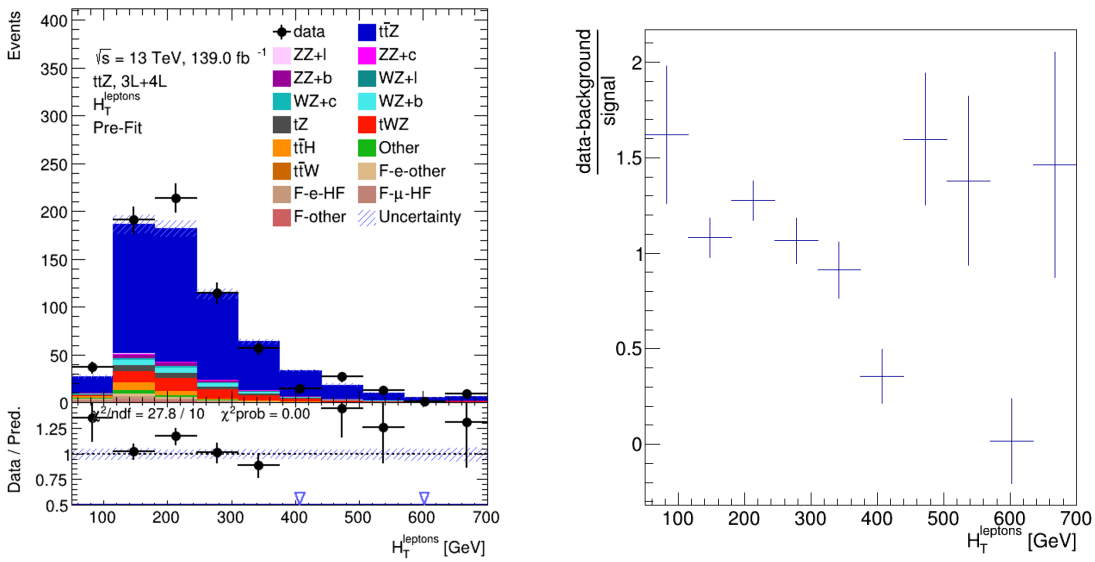

Figure 8.9: Detector-level distribution of the H_{T}^{ℓ} observable in the combination of the trilepton and tetralepton regions (left) and the ratio of observed and expected signal as a function of H_{T}^{ℓ} observable (right).

8.3.2 Data reweighting in H_{T}^{ℓ}

The slope in the linear stress test is an arbitrary parameter, and while it might be sensitive to additional contributions at high p_{T}^{Z}, it is not motivated by a particular physics model. Therefore, it is useful to perform a different kind of stress test, based on observed data. For this test, the pseudo-data is constructed by adding the nominal background predictions to the nominal signal sample that has been reweighted according to the ratio between simulation and data. This ratio will depend on which observable distribution is chosen for the reweighting and it is safest to choose the observable with the largest differences between data and MC-simulation. The observable with the worst modelling - the highest value of χ^2/NDF between MC and data at detector-level - is found to be H_{T}^{ℓ}. Figure 8.9 shows the detector-level distribution of H_{T}^{ℓ} in the combination of the trilepton and tetralepton regions and the histogram of (data - predicted background)/expected ratio.

Pseudo-data is created by adding the nominal background samples to a signal sample reweighted by the data-MC ratio. For each event, the H_{T}^{ℓ} value at truth-level in the nominal signal sample is used to apply the corresponding value of the data-MC ratio as a weight. The

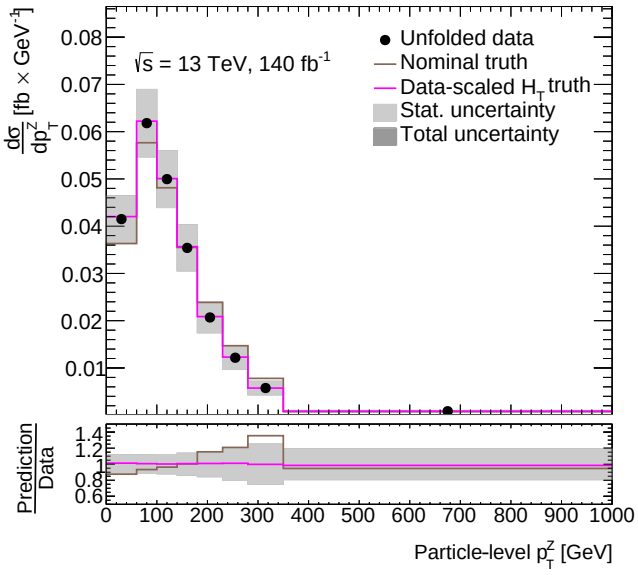

Figure 8.10: Data-driven stress test unfolded pseudo-data distribution of p_{T}^{Z} where the signal sample is reweighted by the ratio of data-MC in the H_{T}^{ℓ} observable.

pseudo-data sample is used as an input to the nominal fit and compared to the reweighted signal sample truth-level distribution for each observable, an example of which is shown in Figure 8.10 for the p_{T}^{Z} observable. Good agreement between the unfolded distribution and reweighted truth distribution, evaluated using the χ^2/NDF metric, is observed for all differential observables. This confirms that the profile likelihood unfolding method is able to reliably recover the shape of the unfolded data.

Chapter 9

Uncertainties

Measurements are only meaningful when they have an associated uncertainty. The measurements described in this thesis require careful consideration of the statistical and systematic sources of uncertainty. Furthermore, the precision of the measurements is a crucial metric for the success of the analysis. Systematic uncertainties, derived from theoretical (modelling) and experimental (detector-related) sources, are combined with the statistical uncertainty to evaluate the total measurement uncertainty. This chapter describes the various sources of systematic uncertainty. As described in Section 7.1, systematic uncertainties are implemented in the fit using nuisance parameters, and each source of uncertainty can contain multiple factors that lead to multiple nuisance parameters.

9.1 Theoretical uncertainties

Theoretical uncertainties arise from approximations in MC event generation. The analysis design heavily relies on simulated events. It is important to understand potential mismodelling effects and evaluate their impact on the differential cross-section results. There are different considerations that must be taken for the simulated signal and background event samples.

$t\bar{t}Z$ signal modelling

Renormalisation and factorisation scale

Variations of the renormalisation and factorisation scales in MC event generation are used to estimate missing higher-order effects. To evaluate the uncertainty associated with the choice of these parameters, they are varied with respect to the nominal MC sample, both simultaneously and individually, up and down by factors of two and a half and compared to the nominal predictions.

PDF

Experimental uncertainties and perturbative QCD calculations contribute to the uncertainties related to the derivation of the nominal PDF set. The uncertainties associated with the derivation of the nominal NNPDF3.0NNLO PDF set are evaluated following the PDF4LHC prescription [130]. The uncertainty related to the choice of the nominal PDF set is evaluated using the PDF4LHC PDF set.

Parton showering

The uncertainty associated with the parton showering algorithm and the underlying event model is evaluated by comparing the nominal samples, generated with MadGraph5_aMC@NLO interfaced to Pythia 8, to alternative samples interfaced to Herwig 7.

Initial-state radiation

The uncertainty associated with initial-state radiation is evaluated by varying the `Var3c` tune setup, which is related to the variation of α_s, of the Pythia `A14` tune in dedicated alternative samples.

Diboson + jets background

The uncertainties listed below are applied as separate nuisance parameters for each of the light-, c- and b-flavour components of the WZ+jets and ZZ+jets background processes in the trilepton and tetralepton analysis regions respectively.

Renormalisation and factorisation scale

The renormalisation and factorisation scale uncertainties are evaluated following the same prescription as for the $t\bar{t}Z$ signal sample.

PDF

Similarly, uncertainties related to the derivation of the nominal PDF set are evaluated following the PDF4LHC prescription. The uncertainty associated with the choice of the nominal PDF set are derived using the CT14 and MMHT14 PDF sets [131, 132] as variations from the nominal. Variations of α_s in the nominal PDF set are also included.

Merging and resummation scales and recoil

Uncertainties on the diboson backgrounds arise from the matching scale, the resummation scale and the recoil scheme. For the diboson background simulated event samples, a matching and merging scheme was used to prevent double-counting of additional QCD radiation. The Catani-Krauss-Kuhn-Webber (CKKW) merging scheme is used to match partons between the matrix element calculation and parton shower algorithm [118]. In order to evaluate the uncertainty associated with the choice of the merging and matching scale, alternative truth-level samples with variations of the scale are compared to the nominal. CKKW matching scale variations compare the nominal 20 GeV, with variations at 15 GeV and 30 GeV. Variations of the resummation scale, which is used in the parton shower step of the event generation process to calculate soft emissions, are performed by varying the QSF resummation parameter to both double and half the nominal value. The uncertainty associated with the choice of recoil scheme is evaluated using an alternative CSSKIN scheme [118] as a variation of the nominal MEPS@NLO prescription.

Cross-section normalisation

A cross-section normalisation uncertainty of 30% is applied to each of the $WZ + l$ and $WZ + c$ backgrounds. Normalisation uncertainties of 10% and 30% are applied to the $ZZ + l$ and $ZZ + c$ backgrounds respectively. The values of these uncertainties are based on discrepancies found in comparisons between data and MC simulated events. As discussed in Section 6.2, the normalisations of the $WZ + b$ and $ZZ + b$ backgrounds are free-floating in the differential cross-section fits and thus have uncertainty associated with their measurement in data.

tZq background

A cross-section normalisation uncertainty of 14% is assigned to the tZq process, based on the dedicated ATLAS measurement in Run 2 [133]. A parton shower uncertainty is obtained by comparing an alternative sample of tZq events generated with MadGraph5_aMC@NLO 2.9.5 interfaced to Herwig 7.2.1 to the nominal setup (MadGraph5_aMC@NLO 2.9.5 interfaced to Pythia 8.245). As for $t\bar{t}Z$, variations of the `Var3c` tune setup of the Pythia `A14` tune, as well as of the factorisation and renormalisation scales, are also included.

tWZ background

For the tWZ background process, the modelling uncertainty is taken as the difference between samples generated with the DR1 and DR2 diagram removal schemes [121]. This leads to a 10 to 15% normalisation uncertainty across the observable distributions. As with the other backgrounds, PDF and renormalisation and factorisation scale uncertainties are taken into account.

$t\bar{t}H$ background

The uncertainty associated with the cross-section normalisation of the $t\bar{t}H$ background is based on theoretical uncertainties. Following the NLO QCD + electroweak calculation presented in Ref. [134], the scale uncertainty is taken to be +5.8% and −9.2%, and the PDF+α_s uncertainty is ±3.6%.

Other background processes

For other minor background processes, such as $t\bar{t}W$, $t\bar{t}t\bar{t}$, $tt\bar{t}$, VVV and VH, a conservative cross-section normalisation uncertainty of 50% is applied. For $t\bar{t}t\bar{t}$, an additional parton shower uncertainty is applied. This is evaluated by comparing samples interfaced to Pythia 8 and

HERWIG 7. These minor background processes typically contribute $< 1\%$ of the total event yields in the signal regions.

9.2 Experimental uncertainties

Detector-related uncertainties cover those derived from detector inefficiencies and the reconstruction and calibration of physics objects.

Luminosity and pileup

The luminosity of the Run 2 dataset recorded by ATLAS is measured by the LUCID-2 subdetector [135] and calibrated following the procedure described in Ref. [35]. The integrated luminosity was found to be $(140.1 \pm 1.2)\,\text{fb}^{-1}$, contributing an uncertainty of 0.83%. Scale factors are applied to MC samples to account for differences in pileup distributions between the simulated events and data. The uncertainty associated with the pileup reweighting scale factors is included as a single nuisance parameter.

Jets

Uncertainties associated with the jet selection arise from the choice of jet energy scale, resolution and vertex tagging.

Jet energy scale and resolution

As mentioned in Section 5.3, the jet energy scale and resolution require some calibration. The jet energy scale calibration and its associated uncertainty are derived by combining LHC test-beam data, collision data and simulated events, described in detail in Ref. [102]. The jet energy scale uncertainties contribute 23 nuisance parameters to the fit. The jet energy resolution is measured separately for data and MC using two in-situ techniques, estimating the jet resolution as a function of p_T. The difference in the jet resolution between simulation and data is corrected for in simulation where it exceeds the resolution in data. Residual uncertainty is propagated to the

analysis by smearing the energy of jets in simulated events by a Gaussian function [102]. This adds 14 nuisance parameters to the fit.

Jet vertex tagging

The efficiency of the jet vertex tagger is measured in $Z(\rightarrow \mu\mu)$+jets event samples, and can vary across different event generators, introducing some uncertainty. The uncertainty associated with the jet vertex tagging is estimated as the difference in the jet vertex tagger efficiency between POWHEG+PYTHIA and SHERPA MC [136].

Jet flavour tagging

The efficiency of the `DL1r` b-tagging algorithm is measured for each jet flavour (b/c/light) using control samples in data and simulated events. From this, scale factors are derived to correct the tagging rates in simulation to match the performance observed in data. The b-tagging efficiency measurement is extrapolated from the p_T region used to determine the scale factors to regions with higher p_T and an additional uncertainty is assigned that is associated with the extrapolation. The uncertainties from the calibration and extrapolation contribute 82 nuisance parameters to the cross-section fit, with different sets of nuisance parameters for each of the flavours.

Leptons

The performance of reconstruction, identification, isolation and trigger algorithms for electrons and muons can differ between simulated events and observed data. Scale factors, as mentioned in Section 5.2, are applied to correct for the difference in efficiency. The efficiency scale factors are derived using reconstructed distributions of the $Z \rightarrow \ell^+\ell^-$ and $J/\psi \rightarrow \ell^+\ell^-$ masses and the tag-and-probe method [91, 92, 96, 137]. Uncertainties relating to the muon momentum scale calibration and resolution are also applied [97]. The variation of these corrections is evaluated separately in the muon spectrometer and tracking subsystems. Similarly, uncertainties relating to the electron energy scale and resolution are applied [93]. In total, uncertainties relating to electrons and muons add 52 and 37 nuisance parameters to the fit, respectively.

$E_{\mathrm{T}}^{\mathrm{miss}}$

Uncertainties on the energy scale and resolution of jets and calibrated photons and leptons are propagated to the calculation of the $E_{\mathrm{T}}^{\mathrm{miss}}$ in each event. As described in Section 5.4, the accurate measurement of $E_{\mathrm{T}}^{\mathrm{miss}}$ is dependent on the measurement of the p_T of the hard and soft terms. The systematic uncertainty for the soft term is derived from the comparison of data and simulated events as described in Ref. [107]. Uncertainties relating to $E_{\mathrm{T}}^{\mathrm{miss}}$ soft term contribute three nuisance parameters to the fit.

Chapter 10

Results

This chapter presents the measured differential cross-sections of $t\bar{t}Z$ in the tetralepton channel and the combination of the trilepton and tetralepton channels. The profile likelihood unfolding method described in Section 7.1 is applied to $t\bar{t}Z$ events that are selected according to requirements outlined in Chapter 6 in order to measure the differential cross-section with respect to the observables described in Section 7.2. The differential cross-sections are compared to state-of-the-art MC predictions.

10.1 Differential cross-section measurements in the tetralepton channel

The measurements of the $t\bar{t}Z$ differential cross-sections in the tetralepton channel are performed with a combined fit to the tetralepton regions, including a region enriched in the dominant $ZZ + b$ background, and fake lepton control regions for each differential observable. This results in the simultaneous extraction of differential cross-sections and background normalisation factors. In each tetralepton differential cross-section measurement, the measured background normalisation factors are found to be consistent with the SM predictions. As an example, the normalisation factors in the fit to the N_{jets} observable are measured as $\mathcal{N}_{ZZ+b} = 1.18^{+0.66}_{-0.58}$, $\mathcal{N}_{e,\text{HF}} = 0.87^{+0.10}_{-0.09}$, $\mathcal{N}_{\mu,\text{HF}} = 0.99^{+0.09}_{-0.08}$ and $\mathcal{N}_{e,\text{other}} = 1.15^{+0.40}_{-0.36}$. These are consistent with the

results from the corresponding inclusive cross-section measurement [1]. The large uncertainty associated with $\mathcal{N}_{ZZ+b}$ reflects the small number of events in the tetralepton channel. The measured fake lepton normalisation factors are similar to those fitted in the fake lepton regions only (Table 6.4). This is because there are few fake lepton events in the tetralepton regions, so the statistical contribution to the measured uncertainty is not significantly impacted in the combined (tetralepton + fake lepton) fit.

The measured differential cross-sections are compared to the SM prediction at particle- and parton-level as calculated using three different MC event samples: MadGraph5_aMC@NLO +Pythia 8 (labelled as MG5_aMC@NLO+Pythia 8), Sherpa 2.2.1 and Sherpa 2.2.11. Figures 10.1 to 10.3 show the absolute and normalised $t\bar{t}Z$ differential cross-section measurements for the observables in the tetralepton channel at particle- and parton-level, except the N_{jets} observable, which is defined at particle-level only. The black markers show the measured cross-section in each bin, while the coloured lines correspond to each SM prediction. The nominal MC event sample, used to design the analysis, is shown as a green line. The associated measurement uncertainties are shown as light- and dark-grey bands for the statistical and total (statistical + systematic) uncertainty, respectively. The differential cross-section measurements with respect to the N_{jets} observable are shown in Figure 10.1. The peak of the distribution is at

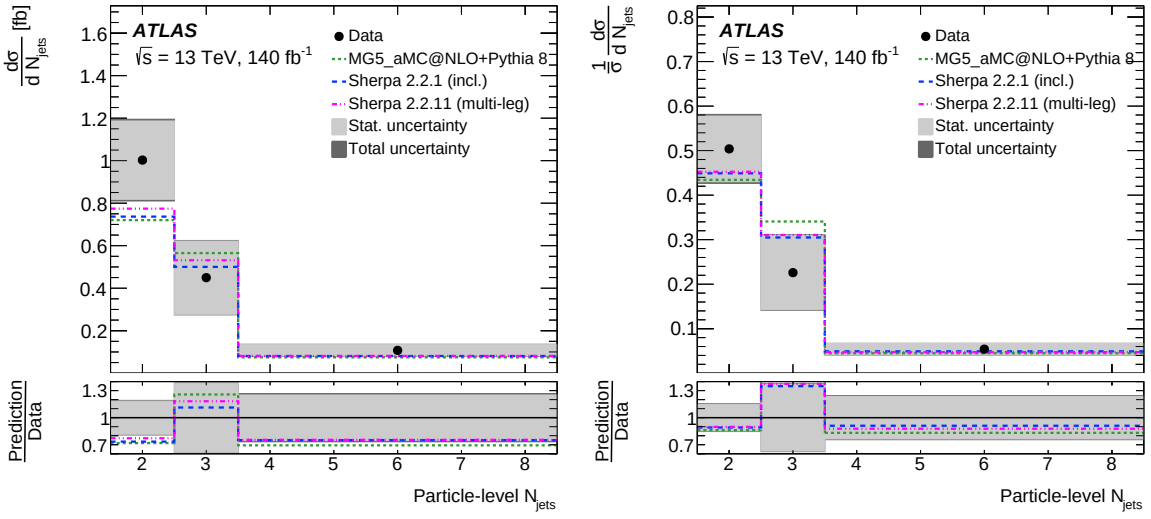

Figure 10.1: Absolute (left) and normalised (right) differential cross-section measurements of $t\bar{t}Z$ with respect to N_{jets} at particle-level in the tetralepton channel.

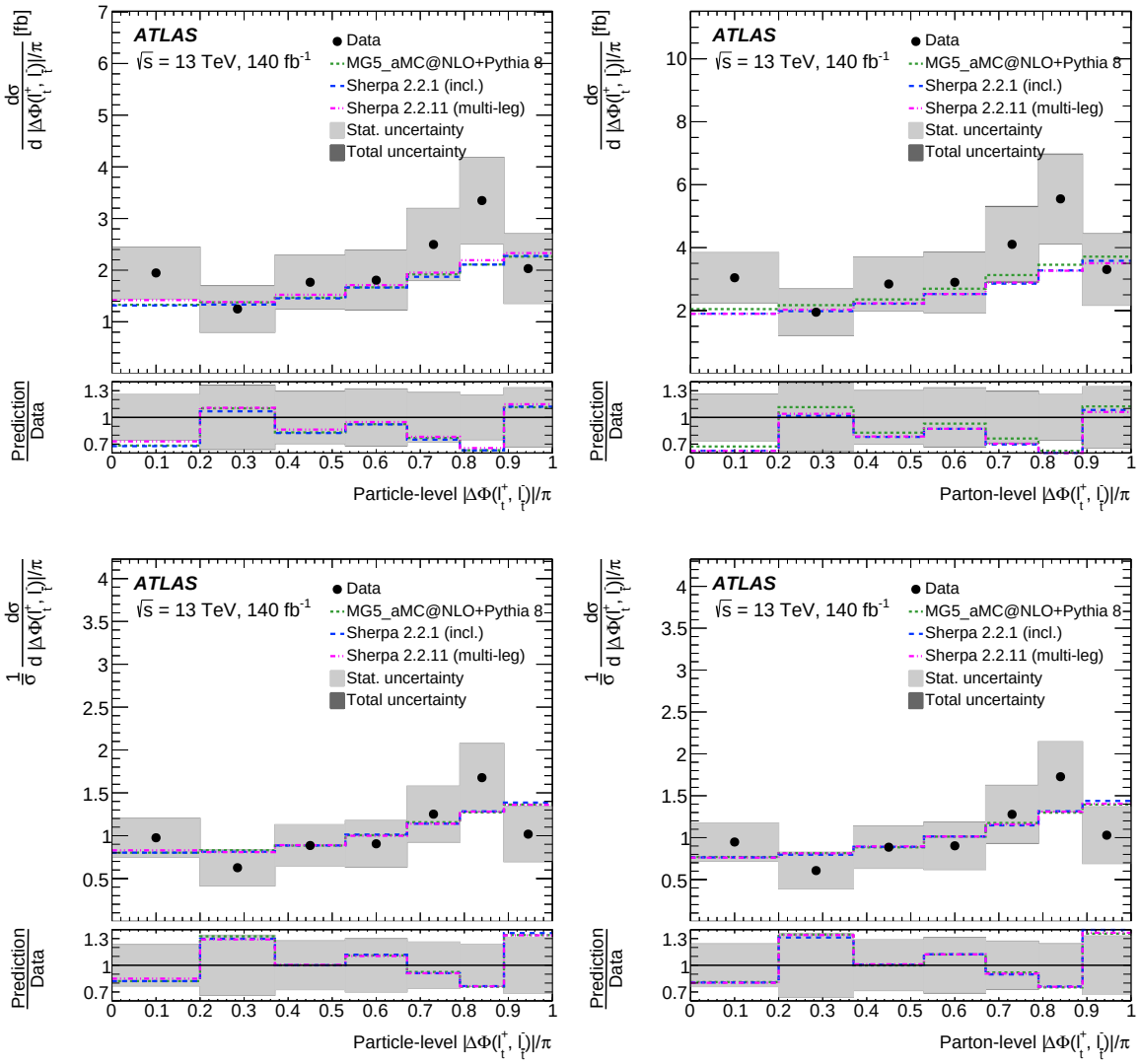

Figure 10.2: Absolute (top) and normalised (bottom) differential cross-section measurements of $t\bar{t}Z$ with respect to $|\Delta\phi(\ell,\ell)|$ at particle- (left) and parton-level (right) in the tetralepton channel.

two, which is the expected number of jets in a $t\bar{t}Z$-4ℓ event at LO. Additional jets are from parton emissions and correspond to higher-order contributions to the cross-section. Naïvely, you might expect these contributions to be approximately 10% of the measured cross-section, corresponding to the value of $\alpha_s(m_Z)$ that arises from the additional QCD vertex. From the normalised measurement we can see that this higher-order contribution ($N_{\text{jets}} \geq 3$) is closer to 50%. This high rate of extra jet production motivates the need for NLO+PS predictions for LHC search analyses. The differential cross-section measurements with respect to $|\Delta\phi(\ell,\ell)|$

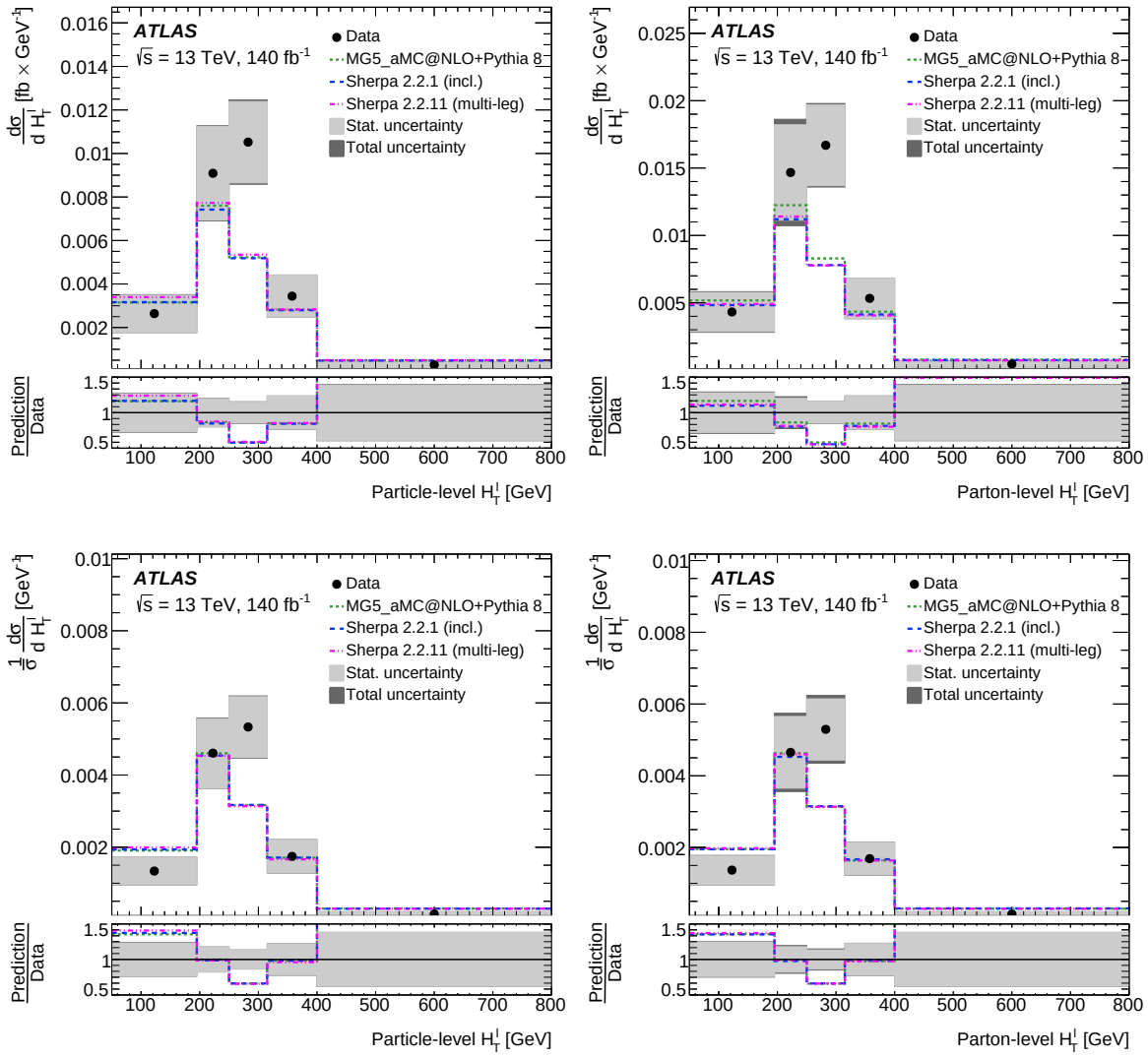

Figure 10.3: Absolute (top) and normalised (bottom) differential cross-section measurements of $t\bar{t}Z$ with respect to H_{T}^{ℓ} at particle- (left) and parton-level (right) in the tetralepton channel.

are shown in Figure 10.2. In the absolute cross-section measurements at both particle- and parton-level, the cross-section measured in data is slightly higher than the prediction in the first and sixth bins of the distribution, though in general the cross-section measurements with respect to $|\Delta\phi(\ell,\ell)|$ show good agreement with the SM predictions. The $|\Delta\phi(\ell,\ell)|$ observable is sensitive to potential BSM effects that can modify the spin correlations between the top and antitop quarks in the $t\bar{t}$ pair. This could be present in the differential cross-section distributions for this observable as a deviation from the shape of the SM prediction. No significant deviation is seen with the precision reached in this analysis. The differential cross-section measurements

with respect to the H_{T}^{ℓ} observable is shown in Figure 10.3. The general shape of the distribution is as expected, with a peak at low- to mid-values of H_{T}^{ℓ} that tails off towards higher values. However, the measured cross-sections are significantly larger than the predictions in the third bin of the distributions. This is also seen at detector-level (Figure 7.3) in the SR-4ℓ-SF and SR-4ℓ-DF regions. As mentioned in Chapter 8, the H_{T}^{ℓ} observable has the largest data-MC disagreement, and can be considered as the worst-modelled observable. It is possible that the high measured cross-section in this bin is a statistical fluctuation in data. Other than this bin, we see good agreement with the SM predicitons.

For the differential cross-section measurements in the tetralepton channel, the unfolded data are generally consistent with the SM predictions within statistical uncertainties. The uncertainties on the differential cross-sections range from 15% to 40% and are dominated by the statistical uncertainty. As $t\bar{t}Z$ is a rare SM process, the statistical uncertainty is the largest limiting factor on the precision of $t\bar{t}Z$ differential cross-section measurements with current ATLAS data. Systematic uncertainties are generally smaller for the normalised cross-section measurements where effects of the uncertainty contributions on the distribution can cancel each other out.

The compatibility of the measured cross-section distributions and the three $t\bar{t}Z$ MC samples described in Section 6.1 is tested using the χ^2 metric described for the validation of the unfolding

Table 10.1: Compatibility of the normalised measured cross-section and MC predictions in the tetralepton channel at particle-level and parton-level.

		MadGraph+Pythia 8		Sherpa 2.2.1		Sherpa 2.2.11	
	Observable	parton	particle	parton	particle	parton	particle
Absolute	N_{jets}	-	0.36	-	0.43	-	0.55
	$\lvert\Delta\phi(\ell,\ell)\rvert$	0.68	0.67	0.52	0.65	0.52	0.77
	H_{T}^{ℓ}	0.04	0.04	0.02	0.04	0.03	0.04
Normalised	N_{jets}	-	0.40	-	0.65	-	0.61
	$\lvert\Delta\phi(\ell,\ell)\rvert$	0.75	0.76	0.73	0.75	0.74	0.80
	H_{T}^{ℓ}	0.03	0.02	0.03	0.02	0.03	0.02

method in Section 8. Table 10.1 shows the p-values from the χ^2 test between the measured differential cross-sections and three MC predictions. The p-values indicate good agreement between the measured cross-section and the prediction for $|\Delta\phi(\ell,\ell)|$ and N_{jets}. The lowest p-values are observed for H_{T}^{ℓ}; this is consistent with the data-MC difference observed at detector-level. There is no clear preference for one particular $t\bar{t}Z$ MC sample at particle- or parton-level across the tetralepton observable distributions. Given that the physics inputs are largely the same to each of these generators, this is perhaps reassuring.

The nuisance parameter ranking process described in Section 7.1 was performed for each differential cross-section measurement in order to quantify the impact of the sources of systematic uncertainty described in Chapter 9 on the measurement precision. While the measurements reported here are statistically-limited, this is an important consideration for future differential measurements of $t\bar{t}Z$, including the measurements currently underway using data collected during the ongoing Run 3 of the LHC. The nuisance parameter ranking is performed in each bin, though only selected bins and observables are shown here for brevity.

The ranking of the nuisance parameters for the N_{jets} measurements are shown in Figure 10.4. Each plot shows the twenty most-important nuisance parameters in a particular bin and the nuisance parameters are ranked by decreasing impact. The empty blue and cyan rectangles show the pre-fit impact and the filled rectangles show the post-fit impact. On the upper axis, the impact on the fitted POI is shown. The lower axis shows the nuisance parameter pull. The pull is comparing the best-fit value to the nominal pre-fit value, with the difference divided by the pre-fit uncertainty. Free-floating normalisation factors used to constrain the fake lepton and diboson background are shown as red markers, while other nuisance parameters associated with sources of systematic uncertainty are shown in black. For the N_{jets} measurements, jet-related systematics are highly-ranked, as well as background normalisation and $t\bar{t}Z$ modelling uncertainties. In general, the individual impacts on the normalised measurements are smaller where some effects of the systematic uncertainties have cancelled out. The systematic uncertainty is largest in the first bin of the N_{jets} distribution, where the nuisance parameter associated with the $ZZ + b$ background normalisation factor is the highest-ranked. From the detector-level distributions (Figure 7.1), we see that this is the bin with the largest contribution from $ZZ + b$ background. Figures 10.5 shows the ranking of the nuisance parameters in the second, fourth

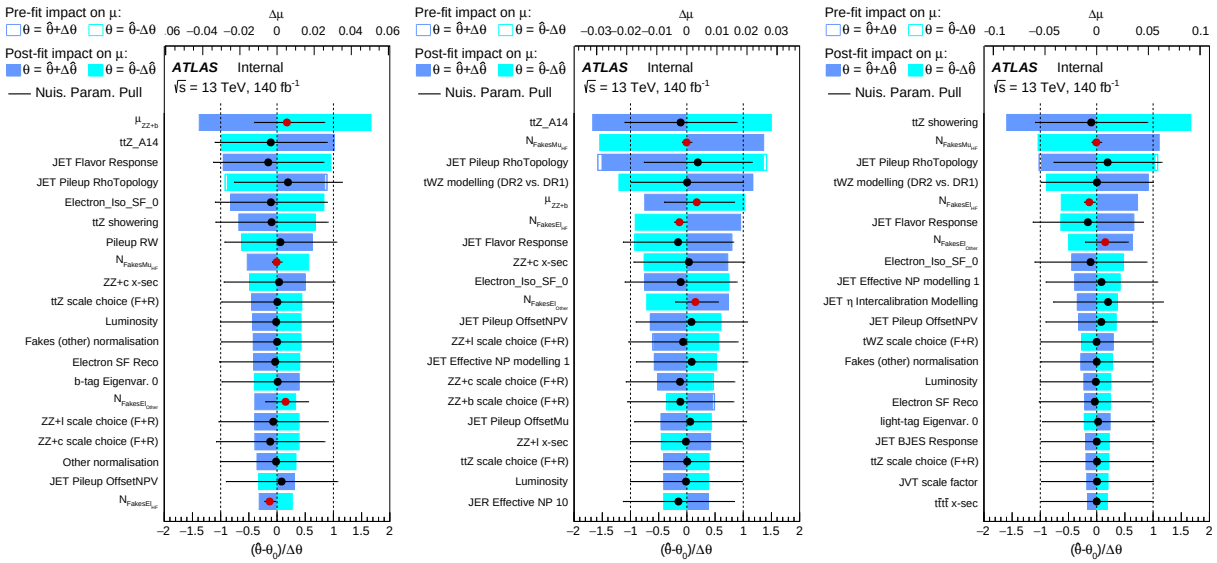

(a) Bin 1 **(b)** Bin 2 **(c)** Bin 3

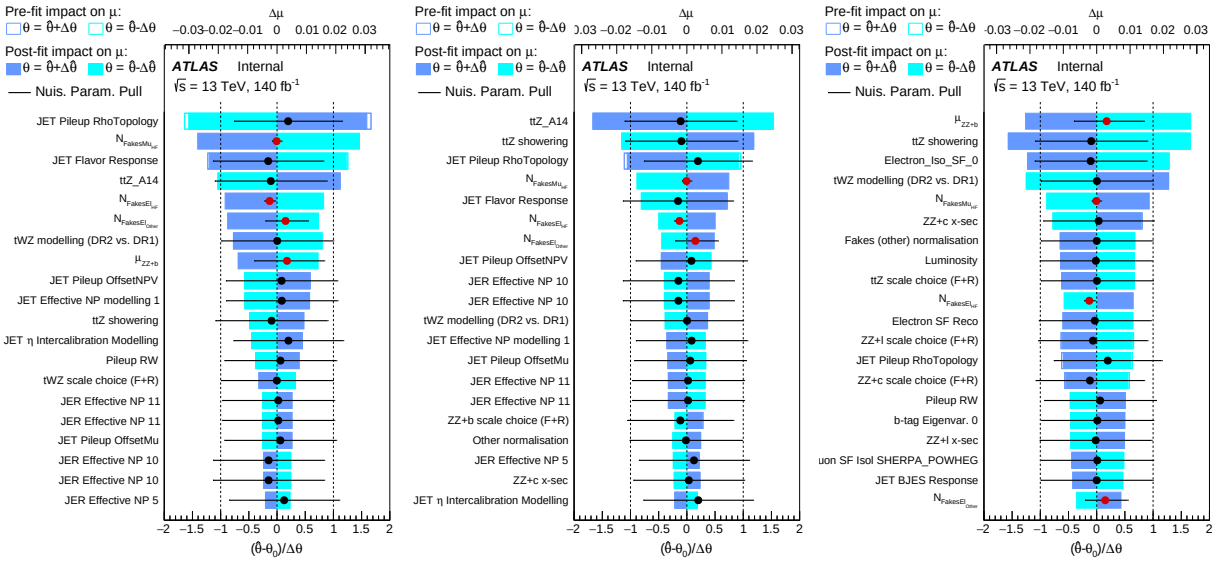

(d) Bin 1 **(e)** Bin 2 **(f)** Total

Figure 10.4: Ranking of nuisance parameters for the first, second and last bin of the N_{jets} absolute (a - c) and normalised (d - f) differential cross-section measurements at particle-level in the tetralepton channel.

and sixth bins of the particle-level $|\Delta\phi(\ell,\ell)|$ differential cross-section measurements. The systematic uncertainty contribution for the $|\Delta\phi(\ell,\ell)|$ measurements is fairly uniform across the distributions. The highest-ranked nuisance parameters for these measurements are associated with the two largest backgrounds, the $ZZ + b$ normalisation factor and the tWZ diagram removal uncertainty, and the $t\bar{t}Z$ parton shower. In general, there are no significant constraints on the nuisance parameters and where there are pulls from the central value, these are small.

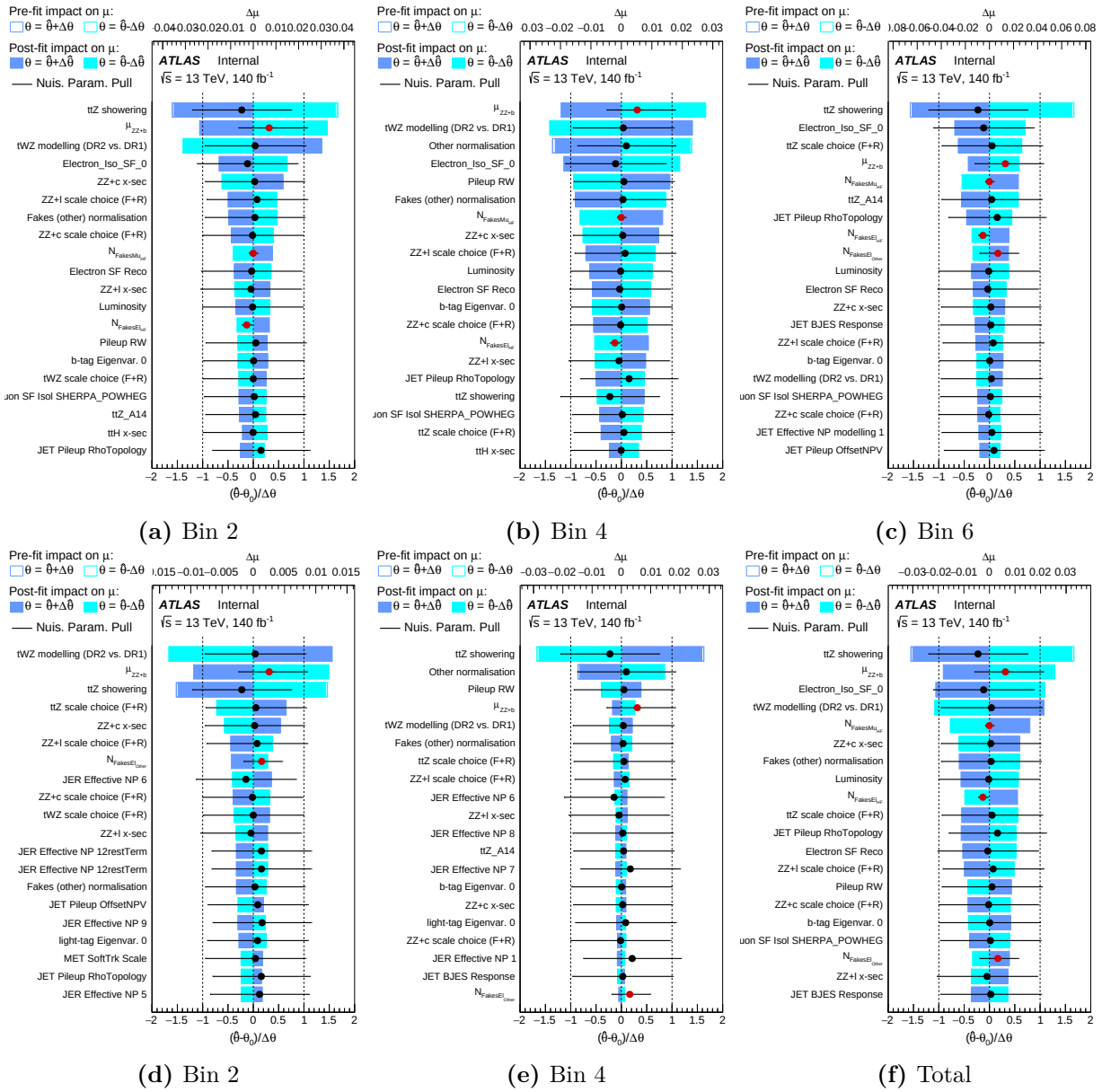

(a) Bin 2 **(b)** Bin 4 **(c)** Bin 6

(d) Bin 2 **(e)** Bin 4 **(f)** Total

Figure 10.5: Ranking of nuisance parameters for the second, fourth and last bin of the $|\Delta\phi(\ell,\ell)|$ absolute (a - c) and normalised (d - f) differential cross-section measurements at particle-level in the tetralepton channel.

Figure 10.6 shows the ranking of the nuisance parameters in the second, third and last (total) bins of the parton-level H_{T}^{ℓ} absolute (normalised) differential cross-section measurements. In the second bin of the H_{T}^{ℓ} distribution, there is a large (10%) impact on the absolute cross-section at parton-level from the choice of $t\bar{t}Z$ parton shower uncertainty, reducing to around 5.5% for the corresponding bin of the normalised measurement. When the analysis is applied to the expectation from the SM, the impact is around 4%. The difference was investigated by

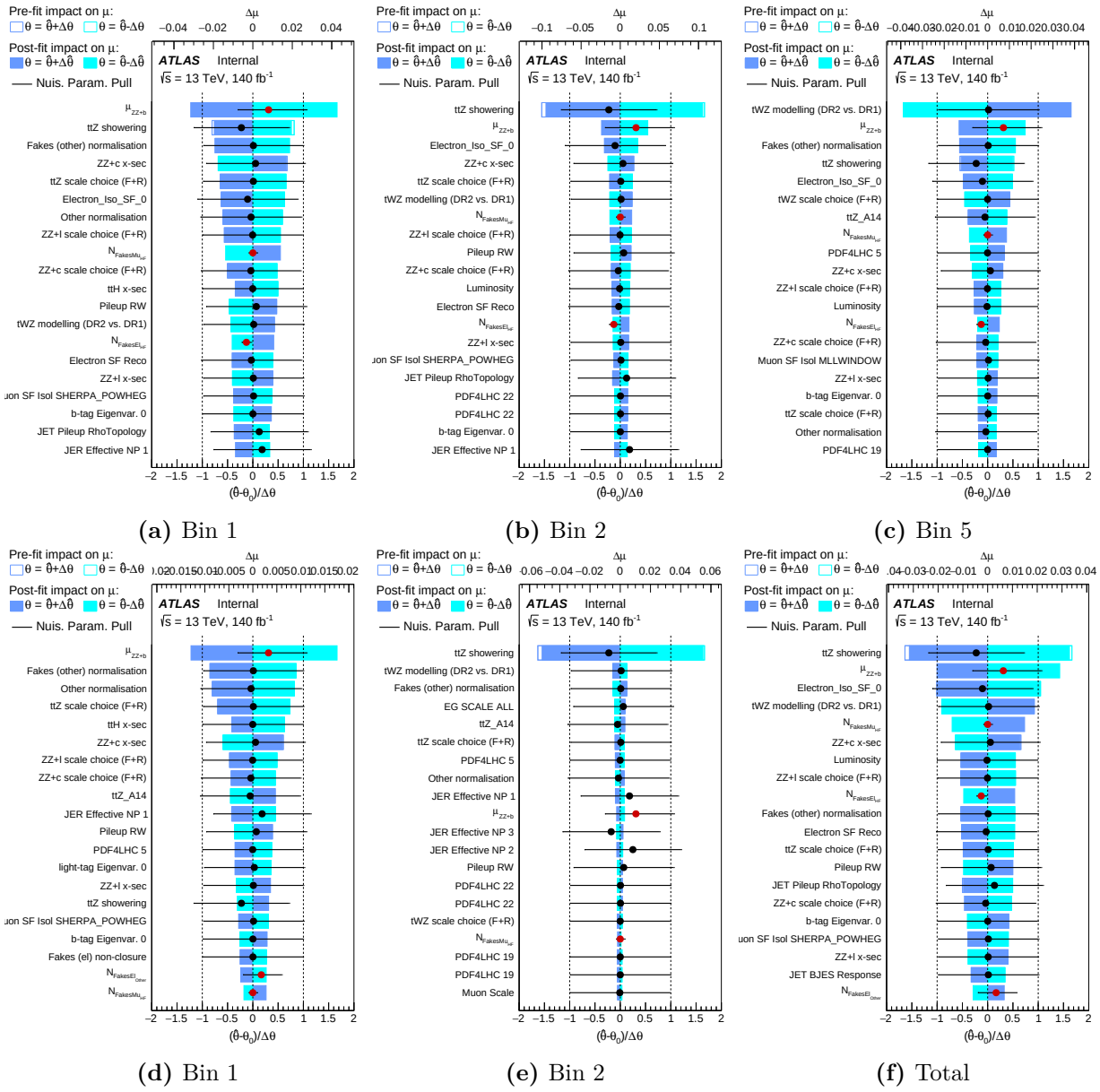

(a) Bin 1 **(b)** Bin 2 **(c)** Bin 5

(d) Bin 1 **(e)** Bin 2 **(f)** Total

Figure 10.6: Ranking of nuisance parameters for the first, second and last bin of the H_{T}^{ℓ} absolute (a - c) and normalised (d - f) differential cross-section measurements at parton-level in the tetralepton channel.

comparing the efficiency and acceptance histograms for the nominal signal sample and the alternative HERWIG sample used to derive the systematic uncertainty on the parton shower. While the efficiencies are similar between the two samples, the acceptance is larger in the nominal sample by around 2% (of 80% acceptance) in each of the three tetralepton regions. This may account for the increase in the impact of the parton shower systematic nuisance parameter

when the cross-section measurement is applied to data. The other highly-ranked nuisance parameters are the $ZZ + b$ normalisation factor and the tWZ diagram removal uncertainty.

Looking forward to the Run 3 measurement of the $t\bar{t}Z$ differential cross-sections, the background normalisation impact will decrease with more data. Then, the signal and background modelling nuisance parameters will have the largest impact on the differential cross-section measurements of $t\bar{t}Z$. Improvements to the MC modelling of the relevant simulated processes is likely to be useful to these measurements in the future.

10.2 Differential cross-section measurements in the combination of the trilepton and tetralepton channels

The measurements of the $t\bar{t}Z$ differential cross-sections in the combination of the trilepton and tetralepton channels is performed in a combined fit to the trilepton, tetralepton and fake lepton regions. The measured values of the fake lepton and diboson normalisation factors $\mathcal{N}_{WZ+b}$, $\mathcal{N}_{ZZ+b}$, $\mathcal{N}_{e,\text{HF}}$, $\mathcal{N}_{\mu,\text{HF}}$ and $\mathcal{N}_{e,\text{other}}$ agree with the SM predictions. As an example, the normalisation factors in the fit to the p_{T}^{Z} observable are measured as $\mathcal{N}_{WZ+b} = 0.95^{+0.39}_{-0.39}$, $\mathcal{N}_{ZZ+b} = 1.60^{+0.76}_{-0.59}$, $\mathcal{N}_{e,\text{HF}} = 0.89^{+0.10}_{-0.10}$, $\mathcal{N}_{\mu,\text{HF}} = 1.02^{+0.09}_{-0.08}$ and $\mathcal{N}_{e,\text{other}} = 1.19^{+0.37}_{-0.37}$. These are also consistent with the results from corresponding inclusive cross-section measurement [1].

Figures 10.7 to 10.9 show the absolute and normalised $t\bar{t}Z$ differential cross-section measurements in the combination of the trilepton and tetralepton channels at particle- and parton-level. In general, the differential cross-section measurements in the combined channel measurements have smaller uncertainties than the tetralepton channel due to the increased number of events, leading to reduced statistical uncertainty. The differential cross-section measurements with respect to the p_{T}^{Z} observable are shown in Figure 10.7. The general shape of the distribution is as expected, with a peak in the low values of p_{T}^{Z} that tails off at high p_{T}^{Z}. The data are higher than the predictions in the low p_{T}^{Z} bins and lower than the predictions in the high p_{T}^{Z} bins, indicating that the data favour a 'softer' (lower-p_T) shape of the distribution. In particular, the measured cross-section is significantly lower than the prediction in the sixth bin of the distribution. This is similar to the detector-level distribution (Figure 7.4) in the SR-3ℓ-$t\bar{t}Z$,

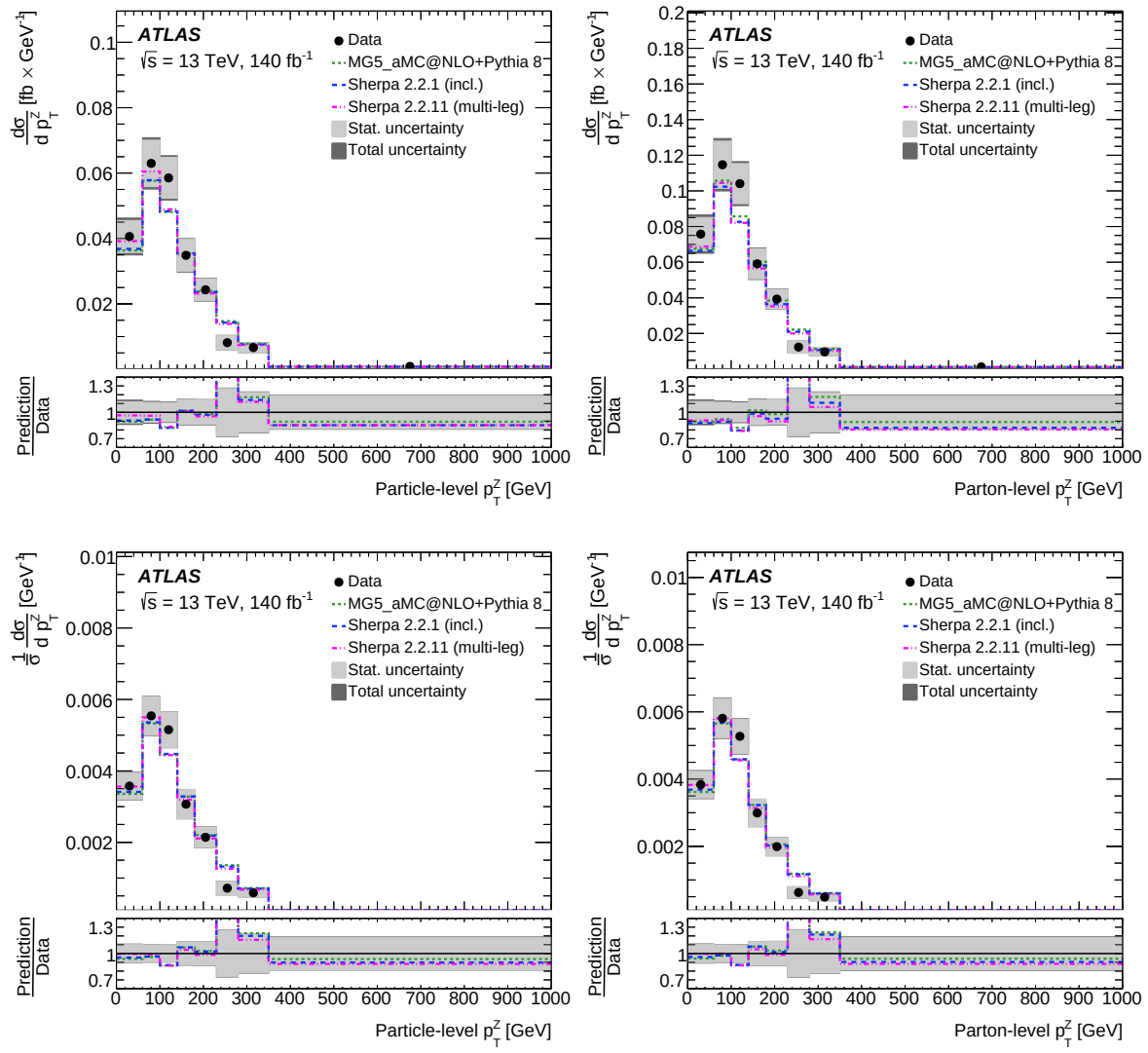

Figure 10.7: Absolute (top) and normalised (bottom) differential cross-section measurements of $t\bar{t}Z$ with respect to p_{T}^{Z} at particle- (left) and parton-level (right) in the combination of the trilepton and tetralepton channels.

SR-3ℓ-tZq and SR-4ℓ-SF regions. The differential cross-section measurements with respect to the $|y^{Z}|$ observable are shown in Figure 10.8. Generally, good agreement is seen between the measured and predicted cross-sections. High values of $|y^{Z}|$ correspond to $t\bar{t}Z$ events with Z-bosons that have high momentum in the z-direction and are angled close to the beam pipe. The shape of the $|y^{Z}|$ distribution is reasonable; as the Z-bosons are on-shell and radiated from either an ingoing or outgoing parton, they are expected to have non-zero transverse momentum

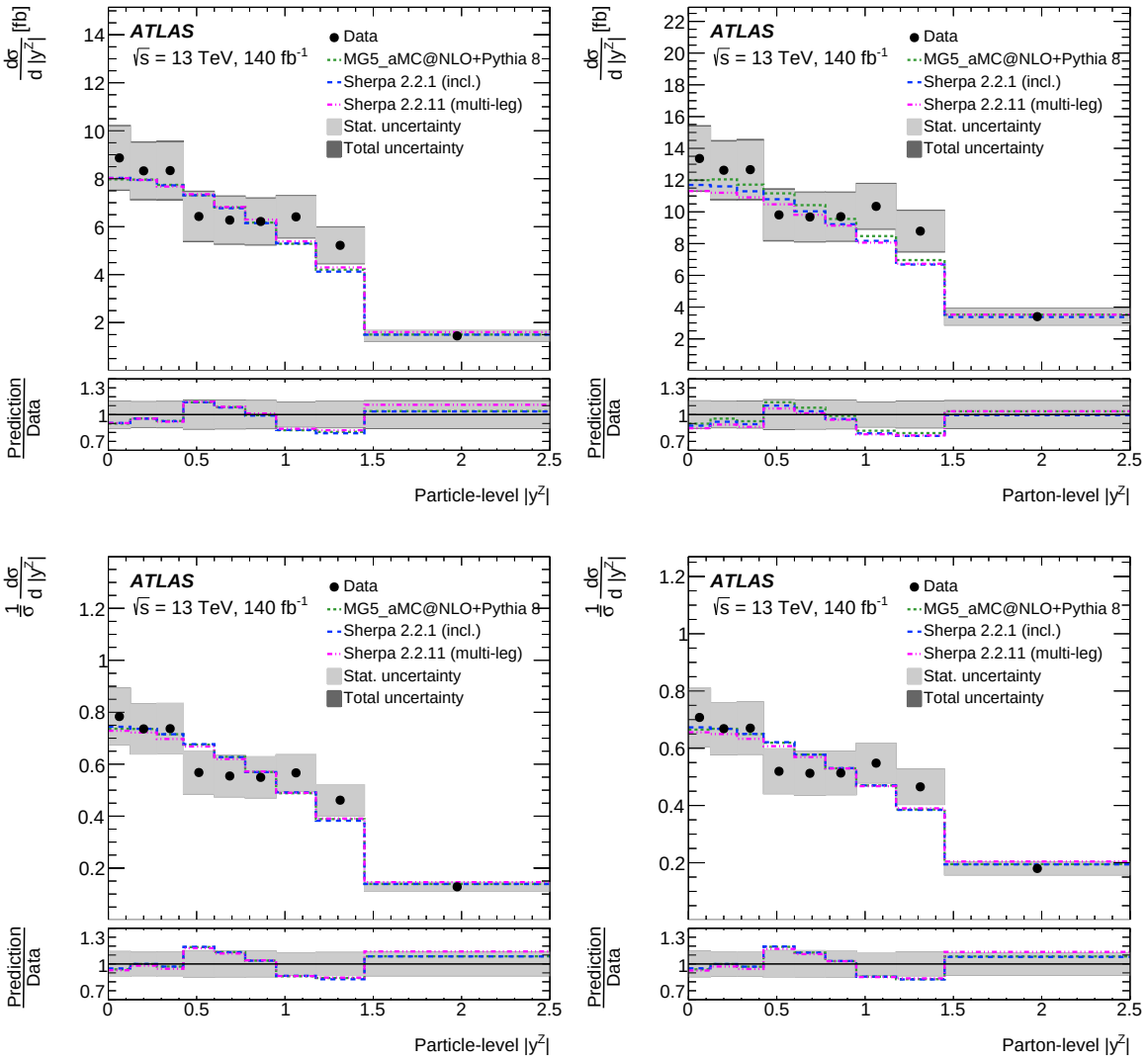

Figure 10.8: Absolute (top) and normalised (bottom) differential cross-section measurements of $t\bar{t}Z$ with respect to $|y^Z|$ at particle- (left) and parton-level (right) in the combination of the trilepton and tetralepton channels.

and tend towards lower values of rapidity. This distribution can be sensitive to the PDF set used in the simulated event sample, as rapidity is directly related to parton momentum.

The $\cos(\theta_Z^\star)$ observable shown in Figure 10.9 is expected to have a slightly peaked distribution favouring middle values of $\cos(\theta_Z^\star)$. This observable is interesting to measure because it is sensitive to the top-quark and Z-boson polarisations [138]. Potential BSM contributions could affect the polarisations and, in turn, the $\cos(\theta_Z^\star)$ distribution shape. For each of the $\cos(\theta_Z^\star)$ measurements, the cross-section is significantly higher than the prediction in the first bin of

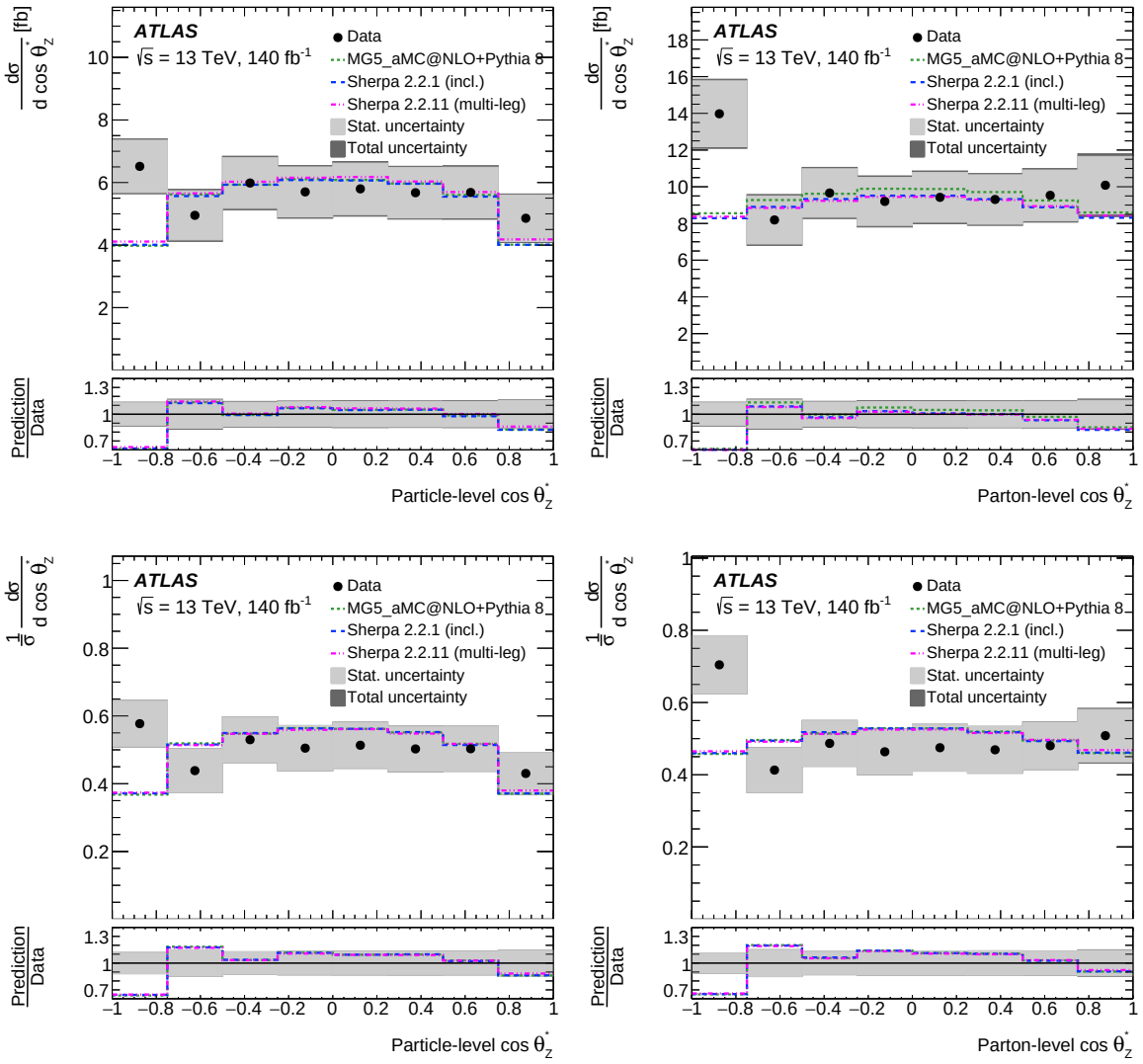

Figure 10.9: Absolute (top) and normalised (bottom) differential cross-section measurements of $t\bar{t}Z$ with respect to $\cos(\theta^{\star}_{Z})$ at particle- (left) and parton-level (right) in the combination of the trilepton and tetralepton channels.

the distribution. This is consistent with the detector-level (Figure 7.6) distributions in the SR-3ℓ-$t\bar{t}Z$ and SR-4ℓ-SF regions, and to a lesser extent in the SR-3ℓ-tZq and SR-3ℓ-WZ regions. To quantify the probability of having this excess in data from statistical fluctuations, the χ^2 was calculated using just the first bin at detector-level. Values of χ^2 can be interpreted through the corresponding p-value. The p-value for fit only including the first bin of $\cos(\theta^{\star}_{Z})$ is 2.2%. Across all the differential cross-section measurements, including differential measurements using regularisation that are not reported here, there are over 100 bins, so it is statistically expected

Table 10.2: Compatibility of the measured cross-section and MC predictions, in the combination of the trilepton and tetralepton channels at particle-level and parton-level.

		MadGraph+Pythia 8		Sherpa 2.2.1		Sherpa 2.2.11	
	Observable	parton	particle	parton	particle	parton	particle
Absolute	p_{T}^{Z}	0.09	0.08	0.13	0.13	0.22	0.23
	$\lvert y^{Z}\rvert$	0.77	0.78	0.70	0.77	0.64	0.77
	$\cos(\theta_{Z}^{\star})$	0.20	0.17	0.21	0.19	0.24	0.22
Normalised	p_{T}^{Z}	0.04	0.03	0.06	0.06	0.13	0.14
	$\lvert y^{Z}\rvert$	0.71	0.72	0.71	0.71	0.70	0.69
	$\cos(\theta_{Z}^{\star})$	0.11	0.11	0.12	0.12	0.15	0.15

that a few of these bins would give p-values on the percent-level, even if the data and prediction are in good agreement.

The compatibility of the measured cross-section distributions and the three $t\bar{t}Z$ MC samples is shown in Table 10.2. The p-values indicate good agreement between the measured cross-section and the prediction for the $|y^{Z}|$ observable, while they are smaller for the p_{T}^{Z} and $\cos(\theta_{Z}^{\star})$ observables due to the data-MC differences described above. Again, there is no clear preference for one particular MC event sample.

Figures 10.10 (a - c) show the nuisance parameter ranking for the first, fourth and last bin of the absolute cross-section with respect to p_{T}^{Z} and Figures 10.10 (d - f) show the nuisance parameter ranking for the first, fourth and total cross-section parameters of the normalised cross-section with respect to p_{T}^{Z}. Modelling uncertainties, such as those associated with the choice of the $t\bar{t}Z$ renormalisation and factorisation scale and the choice of the $t\bar{t}Z$ parton shower are highly ranked, as well as fake lepton and $WZ + b$ background normalisation. The uncertainty associated with the diagram removal scheme in the tWZ background ('tWZ modelling (DR2 vs. DR1)') is ranked highest in the last bin of the absolute cross-section measurements, corresponding to values of high p_{T}^{Z}. From the detector-level distributions of p_{T}^{Z} (Figure 7.4), we can see tWZ background at high-p_{T}^{Z} in the SR-3ℓ-$t\bar{t}Z$, SR-3ℓ-WZ, SR-4ℓ-SF and SR-4ℓ-SF regions. The fake lepton and $WZ + b$ background normalisation factors are

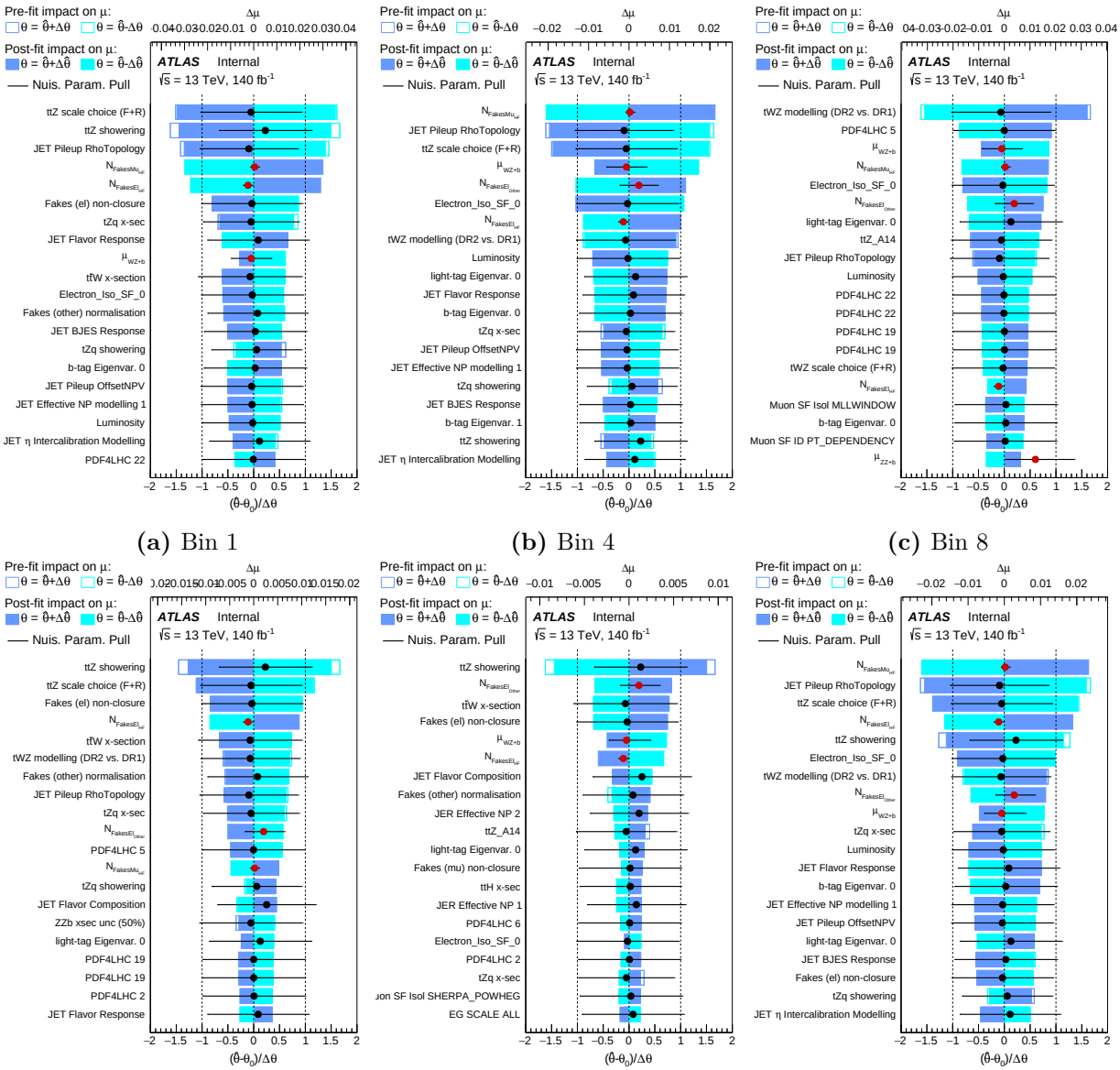

(a) Bin 1 **(b)** Bin 4 **(c)** Bin 8

(d) Bin 1 **(e)** Bin 4 **(f)** Total

Figure 10.10: Ranking of nuisance parameters for the first, fourth and last bins of the p_{T}^{Z} absolute (a - c) and normalised (d - f) differential cross-section measurements at particle-level in the combination of the trilepton and tetralepton channels.

consistently ranked highly across the absolute and normalised cross-section measurements. In general, there are no significant constraints on the nuisance parameters and where there are pulls from the central value, these are small. Figures 10.11 (a - c) show the nuisance parameter ranking for the first, fourth and last bin of the absolute cross-section with respect to $|y^{Z}|$ and Figures 10.11 (d - f) show the nuisance parameter ranking for the first, fourth and total cross-section parameters of the normalised cross-section with respect to $|y^{Z}|$ at parton-level.

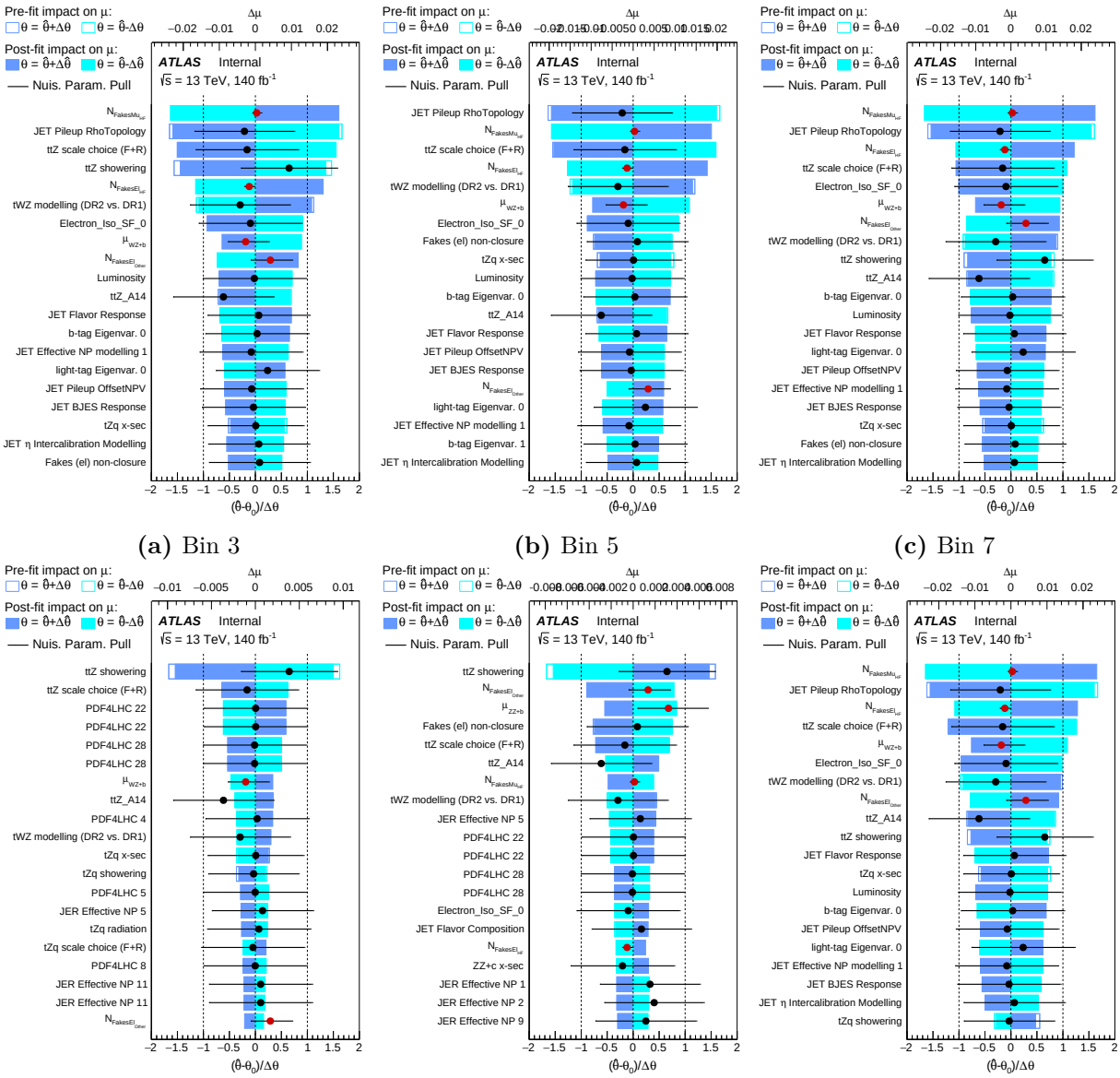

(a) Bin 3 **(b)** Bin 5 **(c)** Bin 7

(d) Bin 3 **(e)** Bin 5 **(f)** Total

Figure 10.11: Ranking of nuisance parameters for the third, fifth and seventh bins of the $|y^Z|$ absolute (a - c) and normalised (d - f) differential cross-section measurements at parton-level in the combination of the trilepton and tetralepton channels.

The systematic uncertainty for the $|y^Z|$ measurements is fairly uniform across each bin of the distribution, with the highest-ranked nuisance parameters being the $t\bar{t}Z$ scale choice, jet pileup and the diboson and fake lepton normalisation factors. Figures 10.12 (a - c) show the nuisance parameter ranking for the first, fourth and last bin of the absolute cross-section with respect to $\cos(\theta^\star_Z)$ and Figures 10.12 (d - f) show the nuisance parameter ranking for the first, fourth and total cross-section parameters of the normalised cross-section with respect

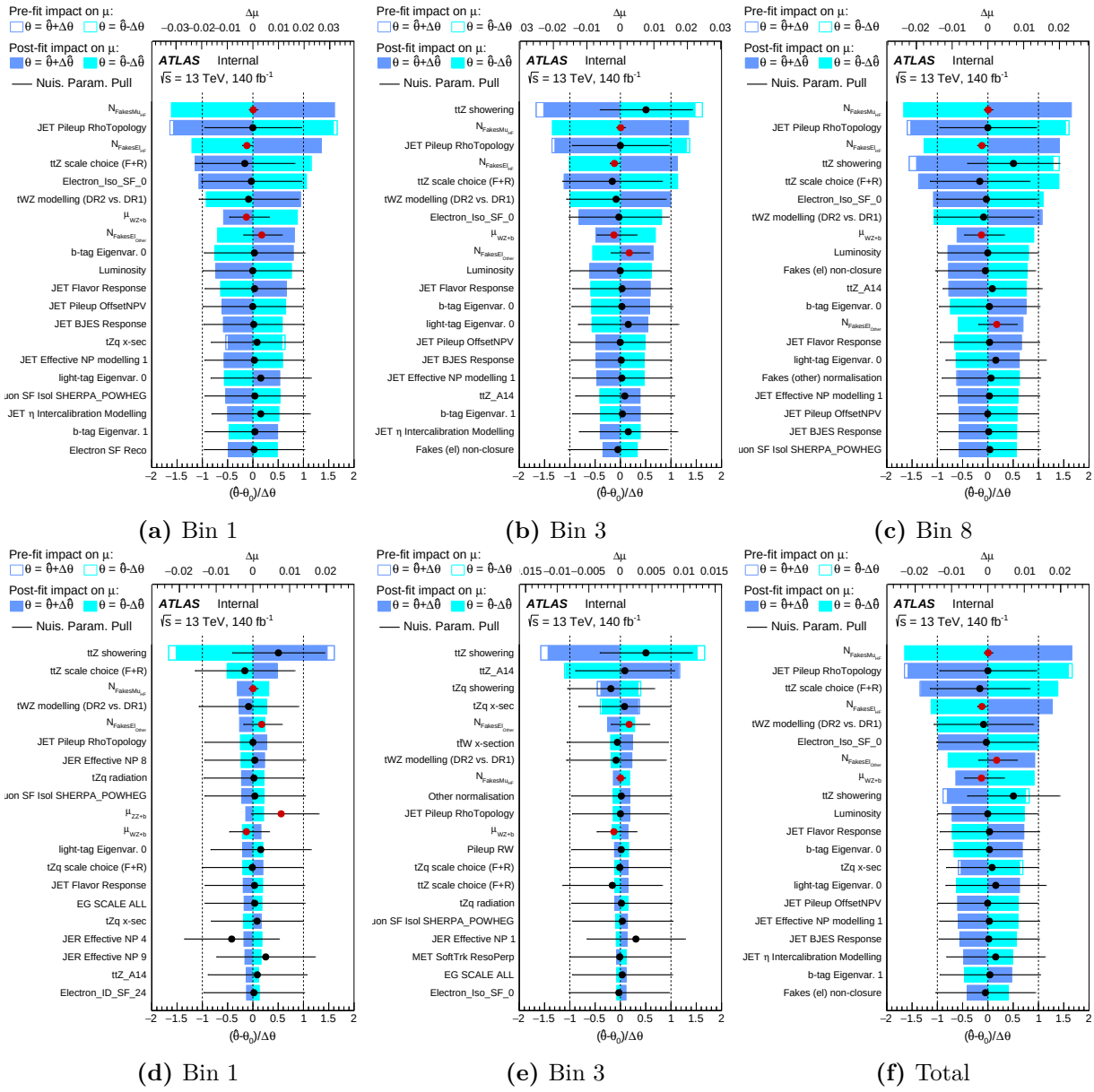

(a) Bin 1 **(b)** Bin 3 **(c)** Bin 8

(d) Bin 1 **(e)** Bin 3 **(f)** Total

Figure 10.12: Ranking of nuisance parameters for the first, third and last bins of the $\cos(\theta^{\star}_{Z})$ absolute (a - c) and normalised (d - f) differential cross-section measurements at particle-level in the combination of the trilepton and tetralepton channels.

to $\cos(\theta^{\star}_{Z})$ at particle-level. The systematic uncertainty for $\cos(\theta^{\star}_{Z})$ measurements has the largest contributions from the $t\bar{t}Z$ parton showering uncertainty, fake lepton normalisation and other $t\bar{t}Z$ modelling systematics. As with the differential cross-section measurements in the tetralepton channels, Run 3 data will improve the measurements in the combination of the trilepton and tetralepton channels by reducing the statistical uncertainty and the uncertainty associated with background normalisation. Then, $t\bar{t}Z$ modelling uncertainties will have the

largest impact on the measured cross-sections. This motivates the careful consideration of these uncertainty contributions for future measurements.

10.3 Comparison to the previous ATLAS measurements with the Run 2 dataset

It is difficult to directly compare the precision of the measurements presented here with previous ATLAS measurements on the Run 2 dataset [25] because the observable distributions have different binning and additional observables are measured in this analysis. However, for the p_{T}^{Z} measurements in the combination of the trilepton and tetralepton channels, there is an additional bin in the differential cross-section measurements here when compared with the previous analysis (Figures 9 and 10 in Ref. [25]) and the precision in each bin is the same or better. This clearly demonstrates the improvement made in this analysis. The same statement applies to the measurements with respect to $|y^{Z}|$ (Figure 11 in Ref. [25]). The measurements with respect to the N_{jets} distribution in the tetralepton channel is the most directly-comparable between the two analyses as it is a discrete observable. In the first bin, corresponding to N_{jets} equal to two, the uncertainty is 18% in the analysis presented here, which is a $\sim 30\%$ improvement on the previous analysis. Inclusive cross-section measurements have also been performed using the same analysis regions and method for the analysis presented in this thesis and the previous ATLAS analysis. In this updated analysis, the inclusive cross-section was measured to be $0.86 \pm 0.05 = 0.86 \pm 0.04$ (stat.) ± 0.04 (syst.) pb [1]. Using the precision of the inclusive cross-sections as a benchmark to compare this analysis and Ref. [25], there is a 35% improvement in the precision of the $t\bar{t}Z$ cross-section measurements presented here using the same dataset [1]. The gain in precision is due to the better separation of the signal and background processes using neural networks, the use of the improved DL1r b-tagging algorithm and the use of the profile likelihood method. Each of these features of the analysis allowed us to include more signal events and a similar number of background events to deliver the most precise differential cross-section measurements of the production of $t\bar{t}Z$ to date.

Chapter 11

Conclusion

This thesis describes differential cross-section measurements of the production of $t\bar{t}Z$ with data collected by the ATLAS detector during Run 2 (2015 - 2018) of the LHC corresponding to an integrated luminosity of $140\,\text{fb}^{-1}$ and centre-of-mass energy of $\sqrt{s} = 13\,\text{TeV}$. The analysis targets the production of a top-antitop quark pair in association with a Z-boson in the trilepton and tetralepton final states. Events are reconstructed into collections of physics objects and required to have three or four isolated leptons in the final state. Neural networks are used in both the trilepton and tetralepton channels to separate $t\bar{t}Z$ events from diboson and fake lepton background processes. Analysis regions are defined using the neural network classifier output. Semi-data-driven techniques are used to estimate the fake lepton background and for the diboson backgrounds, normalisation factors are fitted to data in the unfolding fit. Other backgrounds are estimated with simulated event samples. The profile likelihood unfolding method is used to simultaneously fit multiple orthogonal signal and control regions in the trilepton and tetralepton channels and unfold the differential cross-sections to particle- and parton-level. In order to verify that the unfolding procedure is unbiased, the method is validated using three different tests before the analysis is applied to data. Six differential observables are used to measure the differential cross-sections of $t\bar{t}Z$ production in the tetralepton channel as well as the combination of the trilepton and tetralepton channels. These measurements improve on the previous ATLAS measurements on the Run 2 dataset [25]. The measured differential cross-sections are consistent with the SM predictions and the precision of the differential cross-sections is dominated by the

statistical uncertainty. The measurements are part of a paper submitted for publication, which also includes measurements of the $t\bar{t}Z$ inclusive cross-section and spin correlations, additional differential measurements and an effective field theory interpretation [1].

Looking forward, the Run 3 dataset will double the current available dataset and reduce the statistical uncertainties of future $t\bar{t}Z$ differential cross-section measurements. While statistical uncertainties may still be important, modelling uncertainties will also have a high impact on such measurements. Additionally, it may be possible to include the dilepton channel in the differential cross-section measurements of $t\bar{t}Z$. This channel was previously excluded from the differential cross-section measurements due to very high background. Other final states, such as those with zero charged leptons ($Z \to \nu\bar{\nu}$) are currently the subject of ATLAS analysis. In the search for new physics, the differential cross-section measurements of $t\bar{t}Z$ have been used to set limits on effective field theory parameters. Recent work [139] shows there is interest in a combined effective field theory fit using $t\bar{t}Z$ and other $t\bar{t}X$ processes and makes this an interesting area for future research. The measurements presented in this thesis are fully unfolded and are therefore suitable for inclusion in future global effective field theory fits.

Acknowledgements

This thesis has been the product of three and half years of research, during which I have been helped by many people - too many to name in full, but I hope that, regardless, you know who you are. Starting a PhD in the midst of a global pandemic produced a few obstacles to my initiation into a worldwide research project. Despite this, my supervisor Mark Owen has supported me brilliantly and helped me become a half-decent physicist, so if you're reading this then you know where to send your letters of complaint. I would like to thank my collaborators in the ATLAS top-quark working group, in particular my fellow $t\bar{t}Z$ analysis team members. Thank you to Carmen Diez Pardos and Baptiste Ravina, for their invaluable support with my next steps into academia. I have been fortunate enough to find many friends in my colleagues at the University of Glasgow, whose company has made it a thoroughly enjoyable place to work and to learn. I am particularly grateful to the community I have found in the Glasgow Women in Physics and the Justice, Equality, Diversity & Inclusion groups. During my year at CERN I encountered many budding physicists, conversations with whom have been both enlightening and entertaining; thank you to you all. Thank you to my partner, Nick, who has seen the ups and downs of a particle physics PhD firsthand and supported me throughout. Last but certainly not least, I am thankful for the love and support my family.

Bibliography

[1] ATLAS Collaboration, "Inclusive and differential cross-section measurements of $t\bar{t}Z$ production in pp collisions at $\sqrt{s} = 13$ TeV with the ATLAS detector, including EFT and spin-correlation interpretations," *JHEP*, vol. 08, p. 163, July 2024.

[2] ATLAS Collaboration, "Muon trigger performance in 2022 at $\sqrt{s} = 13.6$ TeV," November 2022.

[3] D. J. Gross and F. Wilczek, "Asymptotically Free Gauge Theories I," *Phys. Rev. D*, vol. 8, pp. 3633–3652, November 1973.

[4] A. Salam and J. Ward, "Electromagnetic and weak interactions," *Physics Letters*, vol. 13, no. 2, pp. 168–171, 1964.

[5] F. Wilczek, "Quantum chromodynamics: The modern theory of the strong interaction," *Annual Review of Nuclear and Particle Science*, vol. 32, no. 1, pp. 177–209, 1982.

[6] F. Englert and R. Brout, "Broken symmetry and the mass of gauge vector mesons," *Phys. Rev. Lett.*, vol. 13, pp. 321–323, August 1964.

[7] P. W. Higgs, "Broken symmetries and the masses of gauge bosons," *Phys. Rev. Lett.*, vol. 13, pp. 508–509, October 1964.

[8] ATLAS Collaboration, "Observation of a new particle in the search for the Standard Model Higgs boson with the ATLAS detector at the LHC," *Physics Letters B*, vol. 716, no. 1, pp. 1–29, 2012.

[9] CMS Collaboration, "Observation of a new boson at a mass of 125 GeV with the CMS

experiment at the LHC," *Phys. Lett. B*, vol. 716, pp. 30–61, 2012.

[10] M. Kobayashi and T. Maskawa, "CP-Violation in the renormalizable theory of weak interaction," *Progress of Theoretical Physics*, vol. 49, no. 2, pp. 652–657, 1973.

[11] CDF Collaboration, "Observation of top quark production in $\bar{p}p$ collisions," *Phys. Rev. Lett.*, vol. 74, pp. 2626–2631, 1995.

[12] D0 Collaboration, "Observation of the top quark," *Phys. Rev. Lett.*, vol. 74, pp. 2632–2637, 1995.

[13] ATLAS and CMS Collaborations, "Combination of Measurements of the Top Quark Mass from Data Collected by the ATLAS and CMS Experiments at $\sqrt{s} = 7$ and 8 TeV," *Phys. Rev. Lett.*, vol. 132, no. 26, p. 261902, 2024.

[14] Particle Data Group, "Review of Particle Physics," *Progress of Theoretical and Experimental Physics*, vol. 2020, p. 083C01, August 2020.

[15] ATLAS Collaboration, "Measurement of the Higgs boson mass with H→$\gamma\gamma$ decays in 140 fb^{-1} of $\sqrt{s} = 13$ TeV pp collisions with the ATLAS detector," *Phys. Lett. B*, vol. 847, p. 138315, 2023.

[16] N. Cabibbo, "Unitary symmetry and leptonic decays," *Phys. Rev. Lett.*, vol. 10, pp. 531–533, June 1963.

[17] UA1 Collaboration, "Experimental observation of isolated large transverse energy electrons with associated missing energy at $\sqrt{s} = 540$ gev," *Physics Letters B*, vol. 122, no. 1, pp. 103–116, 1983.

[18] UA2 Collaboration, "Evidence for $Z^0 \to e^+e^-$ at the CERN pp collider," *Physics Letters B*, vol. 129, no. 1, pp. 130–140, 1983.

[19] Y. L. Dokshitzer, "Calculation of the structure functions for deep inelastic scattering and e^+e^- Annihilation by perturbation theory in quantum chromodynamics," *Sov. Phys. JETP*, vol. 46, pp. 641–653, 1977.

[20] V. N. Gribov and L. N. Lipatov, "Deep inelastic ep scattering in perturbation theory,"

Sov. J. Nucl. Phys., vol. 15, pp. 438–450, 1972.

[21] G. Altarelli and G. Parisi, "Asymptotic freedom in parton language," *Nuclear Physics B*, vol. 126, no. 2, pp. 298–318, 1977.

[22] A. Kulesza, L. Motyka, D. Schwartländer, T. Stebel, and V. Theeuwes, "Associated production of a top quark pair with a heavy electroweak gauge boson at NLO+NNLL accuracy," *Eur. Phys. J. C*, vol. 79, no. 3, p. 249, 2019.

[23] ATLAS Collaboration, "Top Quarks + X Summary Plots November 2023," tech. rep., CERN, Geneva, 2023. All figures including auxiliary figures are available at https://atlas.web.cern.ch/Atlas/GROUPS/PHYSICS/PUBNOTES/ATL-PHYS-PUB-2023-035.

[24] CMS Collaboration, "Measurement of top quark pair production in association with a Z boson in proton-proton collisions at $\sqrt{s} = 13$ TeV," *JHEP*, vol. 03, p. 056, 2020.

[25] ATLAS Collaboration, "Measurements of the inclusive and differential production cross sections of a top-quark-antiquark pair in association with a Z boson at $\sqrt{s} = 13$ TeV with the ATLAS detector," *Eur. Phys. J. C*, vol. 81, no. 8, p. 737, 2021.

[26] O. Bessidskaia Bylund, F. Maltoni, I. Tsinikos, E. Vryonidou, and C. Zhang, "Probing top quark neutral couplings in the Standard Model Effective Field Theory at NLO in QCD," *JHEP*, vol. 05, p. 052, 2016.

[27] J. M. Alves, G. Branco, A. Cherchiglia, C. Nishi, J. Penedo, P. M. Pereira, M. Rebelo, and J. Silva-Marcos, "Vector-like singlet quarks: a roadmap," *Physics Reports*, vol. 1057, pp. 1–69, 2024.

[28] M. Perelstein, "Little Higgs models and their phenomenology," *Prog. Part. Nucl. Phys.*, vol. 58, pp. 247–291, 2007.

[29] ATLAS Collaboration, "Search for direct top squark pair production in events with a Higgs or Z boson, and missing transverse momentum in $\sqrt{s} = 13$ TeV pp collisions with the ATLAS detector," *JHEP*, vol. 08, p. 006, 2017.

[30] ATLAS Collaboration, "Search for new phenomena with top-quark pairs and large missing transverse momentum using 140 fb^{-1} of pp collision data at $\sqrt{s} = 13$ TeV with the ATLAS

detector," *JHEP*, vol. 03, p. 139, 2024.

[31] C. D. Anderson, "The apparent existence of easily deflectable positives," *Science*, vol. 76, no. 1967, pp. 238–239, 1932.

[32] S. H. Neddermeyer and C. D. Anderson, "Note on the nature of cosmic-ray particles," *Phys. Rev.*, vol. 51, pp. 884–886, May 1937.

[33] G. D. Rochester and C. C. Butler, "Evidence for the existence of new unstable elementary particles," *Nature*, vol. 160, pp. 855–857, 1947.

[34] S. Myers and E. Picasso, "The design, construction and commissioning of the cern large electron–positron collider," *Contemporary Physics*, vol. 31, no. 6, pp. 387–403, 1990.

[35] ATLAS Collaboration, "Luminosity determination in pp collisions at $\sqrt{s} = 13$ TeV using the ATLAS detector at the LHC," *Eur. Phys. J. C*, vol. 83, no. 10, p. 982, 2023.

[36] E. Mobs, "The CERN accelerator complex in 2019. Complexe des accélérateurs du CERN en 2019," *CERN-GRAPHICS-2019-002*, 2019. General Photo.

[37] ATLAS Collaboration, "The ATLAS experiment at the CERN Large Hadron Collider," *JINST*, vol. 3, p. S08003, 2008.

[38] CMS Collaboration, "The CMS experiment at the CERN LHC," *Journal of Instrumentation*, vol. 3, p. S08004, August 2008.

[39] ALICE Collaboration, "The ALICE experiment at the CERN LHC," *JINST*, vol. 3, p. S08002, 2008.

[40] LHCb Collaboration, "The LHCb Detector at the LHC," *JINST*, vol. 3, p. S08005, 2008.

[41] W. Herr and B. Muratori, "Concept of luminosity." 10.5170/CERN-2006-002.361, 2006.

[42] ATLAS Collaboration, "ATLAS data quality operations and performance for 2015–2018 data-taking," *Journal of Instrumentation*, vol. 15, p. P04003, April 2020.

[43] J. Pequenao, "Computer-generated image of the whole ATLAS detector." 2008.

[44] ATLAS Collaboration, *ATLAS inner detector: Technical Design Report, 1.* Technical

design report. ATLAS, Geneva: CERN, 1997.

[45] S. Haywood, L. Rossi, R. Nickerson, and A. Romaniouk, *ATLAS inner detector: Technical Design Report, 2*. Technical design report. ATLAS, Geneva: CERN, 1997.

[46] ATLAS Collaboration, "The ATLAS central solenoid," *Nuclear Instruments and Methods in Physics Research Section A: Accelerators, Spectrometers, Detectors and Associated Equipment*, vol. 584, no. 1, pp. 53–74, 2008.

[47] ATLAS Collaboration, "The expected performance of the ATLAS inner detector," tech. rep., CERN, Geneva, 2008. ATL-PHYS-PUB-2009-002.

[48] J. Pequenao, "Computer-generated image of the ATLAS inner detector." 2008.

[49] A. La Rosa, "The ATLAS Insertable B-Layer: from construction to operation," *JINST*, vol. 11, no. 12, p. C12036, 2016.

[50] B. Abbott *et al.*, "Production and Integration of the ATLAS Insertable B-Layer," *JINST*, vol. 13, no. 05, p. T05008, 2018.

[51] ATLAS Collaboration, "Operation and performance of the ATLAS semiconductor tracker," *JINST*, vol. 9, p. P08009, 2014.

[52] ATLAS Collaboration, "The ATLAS Transition Radiation Tracker (TRT) proportional drift tube: design and performance," *Journal of Instrumentation*, vol. 3, p. P02013, February 2008.

[53] ATLAS Collaboration, "The ATLAS Transition Radiation Tracker," tech. rep., CERN, Geneva, 2003.

[54] ATLAS Collaboration, *ATLAS liquid-argon calorimeter: Technical Design Report*. Technical design report. ATLAS, Geneva: CERN, 1996.

[55] ATLAS Collaboration, *ATLAS tile calorimeter: Technical Design Report*. Technical design report. ATLAS, Geneva: CERN, 1996.

[56] J. Pequenao, "Computer-generated image of the ATLAS calorimeter." 2008.

[57] ATLAS Collaboration, *ATLAS muon spectrometer: Technical Design Report*. Technical design report. ATLAS, Geneva: CERN, 1997.

[58] H. H. J. ten Kate, "Superconducting magnet system for the ATLAS detector at CERN," *IEEE Trans. Appl. Supercond.*, vol. 9, no. 2, pt.1, pp. 841–846, 1999.

[59] ATLAS Collaboration, "The ATLAS 'New Small Wheel' muon detector stations recently commissioned for LHC Run 3," *Nuclear Instruments and Methods in Physics Research Section A: Accelerators, Spectrometers, Detectors and Associated Equipment*, vol. 1045, p. 167574, 2023.

[60] J. Pequenao, "Computer-generated image of the ATLAS muon subsystem." 2008.

[61] M. Livan, "Monitored drift tubes in ATLAS," *Nuclear Instruments and Methods in Physics Research Section A: Accelerators, Spectrometers, Detectors and Associated Equipment*, vol. 384, no. 1, pp. 214–218, 1996.

[62] T. Argyropoulos *et al.*, "Cathode strip chambers in ATLAS : Installation, commissioning and in situ performance," in *2008 IEEE Nuclear Science Symposium Conference Record*, pp. 2819–2824, 2008.

[63] D. Boscherini, "Performance and operation of the ATLAS Resistive Plate Chamber system in LHC Run-1," Tech. Rep. 12, CERN, Geneva, 2014.

[64] K. Nagai, "Thin gap chambers in ATLAS," *Nuclear Instruments and Methods in Physics Research Section A: Accelerators, Spectrometers, Detectors and Associated Equipment*, vol. 384, no. 1, pp. 219–221, 1996. BEAUTY '96.

[65] ATLAS Collaboration, "The ATLAS Data Acquisition and High Level Trigger system," *Journal of Instrumentation*, vol. 11, p. P06008, June 2016.

[66] ATLAS Collaboration, "Operation of the ATLAS trigger system in Run 2," *JINST*, vol. 15, no. 10, p. P10004, 2020.

[67] ATLAS Collaboration, "2015 start-up trigger menu and initial performance assessment of the ATLAS trigger using Run-2 data," tech. rep., CERN, Geneva, 2016. All figures including auxiliary figures are available at https://atlas.web.cern.ch/At-

las/GROUPS/PHYSICS/PUBNOTES/ATL-DAQ-PUB-2016-001.

[68] ATLAS Collaboration, "Trigger Menu in 2016," tech. rep., CERN, Geneva, 2017. All figures including auxiliary figures are available at https://atlas.web.cern.ch/Atlas/GROUPS/PHYSICS/PUBNOTES/ATL-DAQ-PUB-2017-001.

[69] ATLAS Collaboration, "Trigger Menu in 2017," tech. rep., CERN, Geneva, 2018. All figures including auxiliary figures are available at https://atlas.web.cern.ch/Atlas/GROUPS/PHYSICS/PUBNOTES/ATL-DAQ-PUB-2018-002.

[70] ATLAS Collaboration, "Trigger menu in 2018," tech. rep., CERN, Geneva, 2019. All figures including auxiliary figures are available at https://atlas.web.cern.ch/Atlas/GROUPS/PHYSICS/PUBNOTES/ATL-DAQ-PUB-2019-001.

[71] ATLAS Collaboration, "Performance of electron and photon triggers in ATLAS during LHC Run 2," *Eur. Phys. J. C*, vol. 80, no. 1, p. 47, 2020.

[72] ATLAS Collaboration, "Performance of the ATLAS muon triggers in Run 2," *JINST*, vol. 15, no. 09, p. P09015, 2020.

[73] T. Sjöstrand, S. Ask, J. R. Christiansen, R. Corke, N. Desai, P. Ilten, S. Mrenna, S. Prestel, C. O. Rasmussen, and P. Z. Skands, "An introduction to PYTHIA 8.2," *Comput. Phys. Commun.*, vol. 191, pp. 159–177, 2015.

[74] E. Bothmann *et al.*, "Event Generation with Sherpa 2.2," *SciPost Phys.*, vol. 7, no. 3, p. 034, 2019.

[75] J. Bellm *et al.*, "Herwig 7.0/Herwig++ 3.0 release note," *Eur. Phys. J. C*, vol. 76, no. 4, p. 196, 2016.

[76] S. Frixione, P. Nason, and C. Oleari, "Matching NLO QCD computations with parton shower simulations: the POWHEG method," *JHEP*, vol. 11, p. 070, 2007.

[77] S. Frixione and B. R. Webber, "Matching NLO QCD computations and parton shower simulations," *JHEP*, vol. 06, p. 029, 2002.

[78] T. Sjöstrand, "Jet fragmentation of multiparton configurations in a string framework,"

Nuclear Physics B, vol. 248, no. 2, pp. 469–502, 1984.

[79] M. Bahr *et al.*, "Herwig++ Physics and Manual," *Eur. Phys. J. C*, vol. 58, pp. 639–707, 2008.

[80] ATLAS Collaboration, "The ATLAS simulation infrastructure," *Eur. Phys. J. C*, vol. 70, 2010.

[81] S. Agostinelli *et al.*, "Geant4 — a simulation toolkit," *Nucl. Instrum. Methods Phys. Res. A*, vol. 506, 2003.

[82] J. Allison *et al.*, "Geant4 developments and applications," *IEEE Transactions on Nuclear Science*, vol. 53, pp. 270–278, February 2006.

[83] T. Cornelissen, M. Elsing, S. Fleischmann, W. Liebig, and E. Moyse, "Concepts, Design and Implementation of the ATLAS New Tracking (NEWT)," *CDS*, March 2007.

[84] R. Frühwirth, "Application of Kalman filtering to track and vertex fitting," *Nuclear Instruments and Methods in Physics Research Section A: Accelerators, Spectrometers, Detectors and Associated Equipment*, vol. 262, no. 2, pp. 444–450, 1987.

[85] ATLAS Collaboration, "Performance of the ATLAS track reconstruction algorithms in dense environments in LHC Run 2," *Eur. Phys. J. C*, vol. 77, no. 10, p. 673, 2017.

[86] ATLAS Collaboration, "Electron and photon reconstruction and performance in ATLAS using a dynamical, topological cell clustering-based approach," *CDS*, December 2017.

[87] ATLAS Collaboration, "Topological cell clustering in the ATLAS calorimeters and its performance in LHC Run 1," *Eur. Phys. J. C*, vol. 77, p. 490, 2017.

[88] ATLAS Collaboration, "Electron reconstruction and identification in the ATLAS experiment using the 2015 and 2016 LHC proton-proton collision data at $\sqrt{s} = 13$ TeV," *Eur. Phys. J. C*, vol. 79, no. 8, p. 639, 2019.

[89] ATLAS Collaboration, "Electron and photon performance measurements with the ATLAS detector using the 2015–2017 LHC proton-proton collision data," *JINST*, vol. 14, no. 12, p. P12006, 2019.

[90] F. He, J. Liu, R. Ospanov, and R. T. Roberts, "Tagging non-prompt electrons and muons using lifetime and isolation information," tech. rep., CERN, Geneva, 2018.

[91] ATLAS Collaboration, "Electron and photon efficiencies in LHC Run 2 with the ATLAS experiment," *pre-print*, August 2023.

[92] ATLAS Collaboration, "Performance of electron and photon triggers in ATLAS during LHC Run 2," *Eur. Phys. J. C*, vol. 80, no. 1, p. 47, 2020.

[93] ATLAS Collaboration, "Electron and photon energy calibration with the ATLAS detector using 2015–2016 LHC proton-proton collision data," *Journal of Instrumentation*, vol. 14, p. P03017, March 2019.

[94] J. Illingworth and J. Kittler, "A survey of the hough transform," *Computer Vision, Graphics, and Image Processing*, vol. 44, no. 1, pp. 87–116, 1988.

[95] ATLAS Collaboration, "Muon reconstruction performance of the ATLAS detector in proton–proton collision data at $\sqrt{s}$ =13 TeV," *Eur. Phys. J. C*, vol. 76, no. 5, p. 292, 2016.

[96] ATLAS Collaboration, "Muon reconstruction and identification efficiency in ATLAS using the full Run 2 *pp* collision data set at $\sqrt{s}$ = 13 TeV," *Eur. Phys. J. C*, vol. 81, no. 7, p. 578, 2021.

[97] ATLAS Collaboration, "Studies of the muon momentum calibration and performance of the ATLAS detector with *pp* collisions at $\sqrt{s}$ = 13 TeV," *Eur. Phys. J. C*, vol. 83, no. 8, p. 686, 2023.

[98] ATLAS Collaboration, "Jet reconstruction and performance using particle flow with the ATLAS Detector," *Eur. Phys. J. C*, vol. 77, no. 7, p. 466, 2017.

[99] M. Cacciari, G. P. Salam, and G. Soyez, "The anti-k_t jet clustering algorithm," *JHEP*, vol. 04, p. 063, 2008.

[100] G. P. Salam, "Towards jetography," *Eur. Phys. J. C*, vol. 67, pp. 637–686, 2010.

[101] ATLAS Collaboration, "Jet energy scale measurements and their systematic uncertainties

in proton-proton collisions at $\sqrt{s} = 13$ TeV with the ATLAS detector," *Phys. Rev. D*, vol. 96, p. 072002, October 2017.

[102] ATLAS Collaboration, "Jet energy scale and resolution measured in proton–proton collisions at $\sqrt{s} = 13$ TeV with the ATLAS detector," *Eur. Phys. J. C*, vol. 81, no. 8, p. 689, 2021.

[103] ATLAS Collaboration, "Performance of pile-up mitigation techniques for jets in *pp* collisions at $\sqrt{s} = 8$ TeV using the ATLAS detector," *Eur. Phys. J. C*, vol. 76, no. 11, p. 581, 2016.

[104] ATLAS Collaboration, "Constituent-level pile-up mitigation techniques in ATLAS," tech. rep., CERN, Geneva, 2017. All figures including auxiliary figures are available at https://atlas.web.cern.ch/Atlas/GROUPS/PHYSICS/CONFNOTES/ATLAS-CONF-2017-065.

[105] ATLAS Collaboration, "ATLAS flavour-tagging algorithms for the LHC Run 2 *pp* collision dataset," *Eur. Phys. J. C*, vol. 83, no. 7, p. 681, 2023.

[106] ATLAS Collaboration, "Optimisation and performance studies of the ATLAS *b*-tagging algorithms for the 2017-18 LHC run," tech. rep., CERN, Geneva, 2017. All figures including auxiliary figures are available at https://atlas.web.cern.ch/Atlas/GROUPS/PHYSICS/PUBNOTES/ATL-PHYS-PUB-2017-013.

[107] ATLAS Collaboration, "Performance of missing transverse momentum reconstruction with the ATLAS detector using proton-proton collisions at $\sqrt{s} = 13$ TeV," *Eur. Phys. J. C*, vol. 78, no. 11, p. 903, 2018.

[108] T. Sjostrand, S. Mrenna, and P. Z. Skands, "A brief introduction to PYTHIA 8.1," *Comput. Phys. Commun.*, vol. 178, pp. 852–867, 2008.

[109] R. D. Ball *et al.*, "Parton distributions for the LHC Run II," *JHEP*, vol. 04, p. 040, 2015.

[110] ATLAS Collaboration, "The Pythia 8 A3 tune description of ATLAS minimum bias and inelastic measurements incorporating the Donnachie-Landshoff diffractive model," August 2016.

[111] ATLAS Collaboration, "The ATLAS Simulation Infrastructure," *Eur. Phys. J. C*, vol. 70, pp. 823–874, 2010.

[112] M. Beckingham *et al.*, "The simulation principle and performance of the ATLAS fast calorimeter simulation FastCaloSim," October 2010.

[113] J. Alwall *et al.*, "The automated computation of tree-level and next-to-leading order differential cross sections, and their matching to parton shower simulations," *JHEP*, vol. 07, p. 079, 2014.

[114] D. J. Lange, "The EvtGen particle decay simulation package," *Nuclear Instruments and Methods in Physics Research Section A: Accelerators, Spectrometers, Detectors and Associated Equipment*, vol. 462, no. 1, pp. 152–155, 2001. BEAUTY2000, Proceedings of the 7th Int. Conf. on B-Physics at Hadron Machines.

[115] S. Catani, F. Krauss, R. Kuhn, and B. R. Webber, "QCD matrix elements + parton showers," *JHEP*, vol. 11, p. 063, 2001.

[116] S. Hoeche, F. Krauss, S. Schumann, and F. Siegert, "QCD matrix elements and truncated showers," *JHEP*, vol. 05, p. 053, 2009.

[117] S. Hoeche, F. Krauss, M. Schonherr, and F. Siegert, "QCD matrix elements + parton showers: The NLO case," *JHEP*, vol. 04, p. 027, 2013.

[118] S. Schumann and F. Krauss, "A parton shower algorithm based on Catani-Seymour dipole factorisation," *JHEP*, vol. 03, p. 038, 2008.

[119] S. Hoeche, F. Krauss, M. Schonherr, and F. Siegert, "A critical appraisal of NLO+PS matching methods," *JHEP*, vol. 09, p. 049, 2012.

[120] F. Cascioli, P. Maierhofer, and S. Pozzorini, "Scattering Amplitudes with Open Loops," *Phys. Rev. Lett.*, vol. 108, p. 111601, 2012.

[121] F. Demartin *et al.*, "tWH associated production at the LHC," *Eur. Phys. J. C*, vol. 77, no. 1, p. 34, 2017.

[122] J. Heaton, "Applications of deep neural networks," 2020.

[123] F. Chollet *et al.*, "Keras." `https://keras.io`, 2015.

[124] M. Cacciari, G. P. Salam, and G. Soyez, "The Catchment Area of Jets," *JHEP*, vol. 04, p. 005, 2008.

[125] G. Cowan, K. Cranmer, E. Gross, and O. Vitells, "Asymptotic formulae for likelihood-based tests of new physics," *Eur. Phys. J. C*, vol. 71, p. 1554, 2011. [Erratum: Eur.Phys.J.C 73, 2501 (2013)].

[126] T. D. et al., "Documentation for TRExFitter." `https://trexfitter-docs.web.cern.ch/trexfitter-docs/`. Accessed: 2024-03-06.

[127] F. James and M. Roos, "Minuit - a system for function minimization and analysis of the parameter errors and correlations," *Computer Physics Communications*, vol. 10, no. 6, pp. 343–367, 1975.

[128] G. D'Agostini, "A multidimensional unfolding method based on Bayes' theorem," *Nuclear Instruments and Methods in Physics Research Section A: Accelerators, Spectrometers, Detectors and Associated Equipment*, vol. 362, no. 2, pp. 487–498, 1995.

[129] R. D. Cousins, "Generalization of chisquare goodness-of-fit test for binned data using saturated models, with application to histograms." 2013.

[130] J. Butterworth *et al.*, "PDF4LHC recommendations for LHC Run II," *J. Phys. G*, vol. 43, p. 023001, 2016.

[131] S. Dulat *et al.*, "New parton distribution functions from a global analysis of quantum chromodynamics," *Phys. Rev. D*, vol. 93, no. 3, p. 033006, 2016.

[132] L. A. Harland-Lang, A. D. Martin, P. Motylinski, and R. S. Thorne, "Parton distributions in the LHC era: MMHT 2014 PDFs," *Eur. Phys. J. C*, vol. 75, no. 5, p. 204, 2015.

[133] ATLAS Collaboration, "Observation of the associated production of a top quark and a Z boson in pp collisions at $\sqrt{s} = 13$ TeV with the ATLAS detector," *JHEP*, vol. 07, p. 124, 2020.

[134] D. de Florian *et al.*, "Handbook of LHC Higgs Cross Sections: 4. Deciphering the Nature

of the Higgs Sector," vol. 2/2017, October 2016.

[135] G. Avoni *et al.*, "The new LUCID-2 detector for luminosity measurement and monitoring in ATLAS," *JINST*, vol. 13, no. 07, p. P07017, 2018.

[136] ATLAS Collaboration, "Performance of pile-up mitigation techniques for jets in pp collisions at $\sqrt{s} = 8$ TeV using the ATLAS detector," *Eur. Phys. J. C*, vol. 76, no. 11, p. 581, 2016.

[137] ATLAS Collaboration, "Performance of the ATLAS muon triggers in Run 2," *JINST*, vol. 15, no. 09, p. P09015, 2020.

[138] ATLAS Collaboration, "Measurement of the angular coefficients in Z-boson events using electron and muon pairs from data taken at $\sqrt{s} = 8$ TeV with the ATLAS detector," *JHEP*, vol. 08, p. 159, 2016.

[139] ATLAS Collaboration, "Measurements of inclusive and differential cross-sections of $t\bar{t}\gamma$ production in pp collisions at $\sqrt{s} = 13$ TeV with the ATLAS detector," March 2024.

Glossary of acronyms

ALICE A Large Ion Collider Experiment. 18, 155

ATLAS A Toroidal LHC Apparatus. i, 5, 11–13, 18, 20–22, 24–28, 30, 33, 36, 39, 44, 45, 50, 62, 67, 77, 117, 125, 138–140, 155, 163

BDT Boosted Decision Tree. 42, 155

BSM Beyond the Standard Model. 13, 14, 124, 132, 155

CERN Conseil Européen pour la Recherche Nucléaire. 8, 17–19, 155, 163

CKKW Catani-Krauss-Kuhn-Webber merging scheme. 115, 155

CKM Cabbibo-Kobayashi-Maskawa. 6, 155

CMS Compact Muon Solenoid. 5, 12, 18, 37, 67, 155

CR Control Region. 51, 55, 155

CSC Cathode Strip Chambers. 28, 29, 42, 155

CSSKIN Catani-Seymour Recoil Kinematics Scheme. 115, 155

DF Different-Flavour, referring to a lepton pair. 58, 155

DNN Deep Neural Network. 58–62, 77, 155

DR Diagram Removal. 52, 116, 155

EFT Effective Field Theory. 155

EM Electromagnetic. 155

EMEC Electromagnetic Endcap. 27, 47, 155

EWK Electroweak. 3, 4, 11, 14, 155

EWSB Electroweak Symmetry Breaking. 5, 155

FCal Forward Calorimeter. 27, 155

HEC Hadronic Endcap. 27, 47, 155

HLT High-Level Trigger. 30, 155

IBL Insertable B-Layer. 23, 155

ID Inner Detector. 23, 25, 29, 155

IP Interaction Point. 21, 23, 155

IR Infrared. 10, 155

ISR Initial-State Radiation. 155

JER Jet Energy Resolution. 155

JES Jet Energy Scale. 155

JVT Jet Vertex Tagger. 44, 155

L1 Level-1 trigger. 30, 155

LAr Liquid Argon. 27, 47, 155

LCW Local Cell Weighting. 155

LEP Large Electron-Positron collider. 17, 155

LHC Large Hadron Collider. i, 5, 9, 10, 12, 17–21, 23, 29, 30, 33, 36, 46, 67, 117, 123, 126, 139, 155

LHCb Large Hadron Collider beauty. 18, 155

LO Leading Order. 10, 34, 51–53, 123, 155

MC Monte Carlo. 33, 34, 36, 37, 49, 50, 52–54, 68, 74, 75, 99, 111–115, 117, 118, 121, 122, 125, 126, 130, 134, 155

MDT Monitored Drift Tubes. 28, 29, 42, 155

ME Matrix Element. 33, 155

MPI Multiple Parton Interaction. 36, 155

NDF Number of Degrees of Freedom. 101, 111, 112, 155

NLO Next-to-Leading Order. 10, 11, 13, 14, 34, 50, 52, 53, 116, 123, 155

NNLL Next-to-Next-to Leading Logarithm. 11, 14, 155

NNLO Next-to-Next-to Leading Order. 155

NP Nuisance Parameter. 68, 69, 155

NSW New Small Wheel. 28, 155

OSSF Opposite-Sign Same-Flavour, referring to a lepton pair. 8, 11, 55, 58, 65, 155

PDF Parton Distribution Function. 9, 10, 14, 33, 50–54, 114–116, 132, 155

PLU Profile Likelihood Unfolding. 67, 155

PLV Prompt Lepton Veto. 42, 155

POI Parameter of Interest. 68–72, 101, 102, 126, 155

PS Parton Shower. 33, 123, 155

PV Primary Vertex. 155

QCD Quantum Chromodynamics. 4, 10, 14, 34, 35, 43, 52, 114–116, 123, 155

QFT Quantum Field Theory. 3, 10, 155

RMS Root Mean Squared. 102, 155

ROI Regions of Interest. 30, 155

RPC Resistive Plate Chambers. 28–30, 42, 155

SCT Semiconductor Tracker. 23, 25, 39, 40, 155

SF Same-Flavour, referring to a lepton pair. 58, 59, 155

SM Standard Model. 3, 4, 9, 10, 12–15, 18, 27, 49, 51, 56, 59, 61, 68, 105, 121, 122, 124, 125, 128, 130, 139, 155

SPS Super Proton Synchrotron. 155

SR Signal Region. 55, 155

TDAQ Trigger and Data Acquisition. 30, 155

TGC Thin Gap Chambers. 28–30, 42, 155

TRT Transition Radiation Tracker. 23, 25, 29, 40, 155

UA1 Underground Area 1. 8, 155

UA2 Underground Area 2. 8, 155

UV Ultraviolet. 10, 155

List of tables

List of figures